UiT
THE ARCTIC
UNIVERSITY
OF NORWAY

Faculty of Science and Technology
Department of Geosciences

Changes in paleoceanography and methane release in relation to past climatic variability at Vestnesa Ridge, Svalbard

Jarl-Eirik Åsheim
EOM-3901 Master's thesis in Energy, Climate and Environment
June 2017

Abstract

Sediment core HH16-549GC from Vestnesa Ridge in the Fram Strait, western Svalbard, has been investigated in order to reconstruct paleoceanographic and paleoclimatic conditions from 31,000 to 7500 cal years BP. Vestnesa Ridge is located in an area with extensive seepage of methane from the ocean floor. The core is retrieved from within a pockmark to reconstruct possible changes in seepage of methane in the past. Methane is a potent greenhouse gas regarded to be 25 times more potent than CO_2. Fluctuations of methane release through time are particularly interesting to study in this area as the Fram Strait constitutes the predominant route for water and heat exchange between the world's ocean and the Arctic Basin. Potential seepage of gas is important to study in order to investigate the possible effects it might cause on a continuously changing climate.

The core has been divided into six different units based on lithological and stratigraphical parameters by investigating the distribution of grain sizes, magnetic susceptibility, assemblage of planktic and benthic foraminifera, stable isotopes and content of total carbon, total organic carbon, sulfur and calcium carbonate. An age model was established by correlating the results from HH16-549GC with results from a study from Jessen et al (2010), which compared and correlated 11 sediment cores from the western Svalbard region. The age model is based on AMS-^{14}C dates and correlation to the Marine Isotope Stages (MIS) based on $\delta^{18}O$ values from stable isotope analysis. The record covers MIS3 to MIS 1 (31,000-7500 cal years BP). Only late MIS3 from 31,000 to 29,000 cal years BP is present in this core and terminate at the end of Heinrich event 3 (30,500 cal years BP). MIS 2 is characterized by high $\delta^{18}O$ values and comprises the period from 29,000 to 14,000 cal years BP which includes the Last Glacial Maximum (26,800-20,671 cal years BP), early deglaciation (20,671-19,327) and Heinrich event 1 (19,327-15,600 cal years BP). MIS 1 starts as the value of $\delta^{18}O$ declines and includes periods such as Bølling-Allerød interstadials and Younger Dryas (15,600-11,700 cal years BP) and the Holocene (11,700 cal years BP until recent).

Possible events of paleo-methane seepages is indicated by low $\delta^{13}C$ values and high content of total organic carbon. In this thesis two major events of methane seepages with peaking intensity is interpreted to occur in the start of the Bølling-Allerød interstadials (14,900 cal years BP) and at the onset of the Last Glacial Maximum (26,300 cal years BP). These seepage events are likely to be triggered by increased seismic activity, variation in sea-level and high sediment supply

Acknowledgments

Table of Contents

1 Introduction

1.1 Objectives

The objective in this study is to reconstruct paleoceanography and paleoclimate at Vestnesa Ridge in Fram Strait, western Svalbard. Additionally, these results will be correlated to identify possible methane seepage from the core site. This study has been carried out by investigating the sediment core HH16-549GC retrieved from within a pockmark at Vestnesa Ridge.

1.2 Background

Sediment core HH16-549GC was retrieved from Vestnesa Ridge in Fram Strait, on the slope of western-Svalbard. Fram Strait is particularly interesting to investigate because of extensive methane seepage from the ocean floor in this area (Hustoft, et al., 2009a). Vestnesa is regarded as one of the northernmost deep-water gas provinces in the Arctic (Hustoft, et al., 2009a; Bunz, et al., 2012). Methane has a considerable impact on the climate and is therefore important to study as it is considered to be 25 times stronger as a greenhouse gas than carbon dioxide on a 100-year timescale (Intergovernmental Panel on Climate Change, 2007; Schaefer, et al., 2012). Potential seepage of gas in Fram Strait can be identified by examining it in relation to paleoceanography and paleoclimate. Figure 1 and 2 show the location of Vestnesa Ridge.
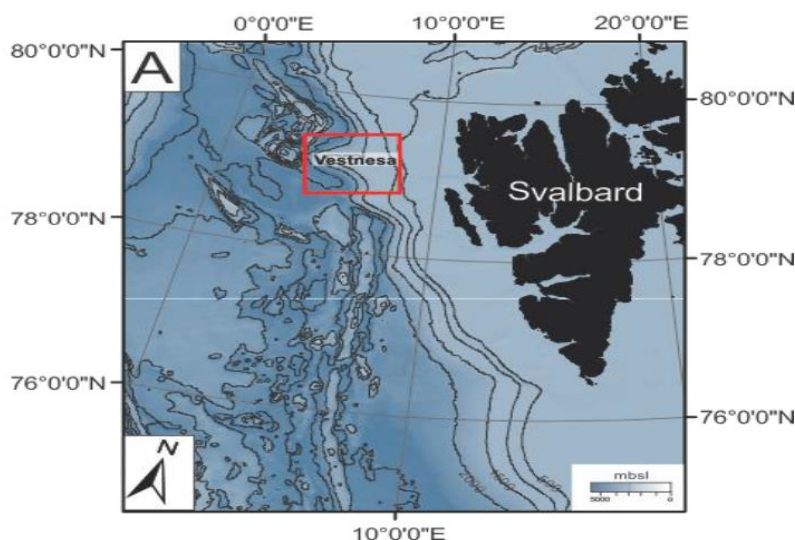
Figure 1: Bathymetry of Vestnesa Ridge in Fram Strait, located on the slope of western of Svalbard (red box). Adapted from Myrvang (2015).
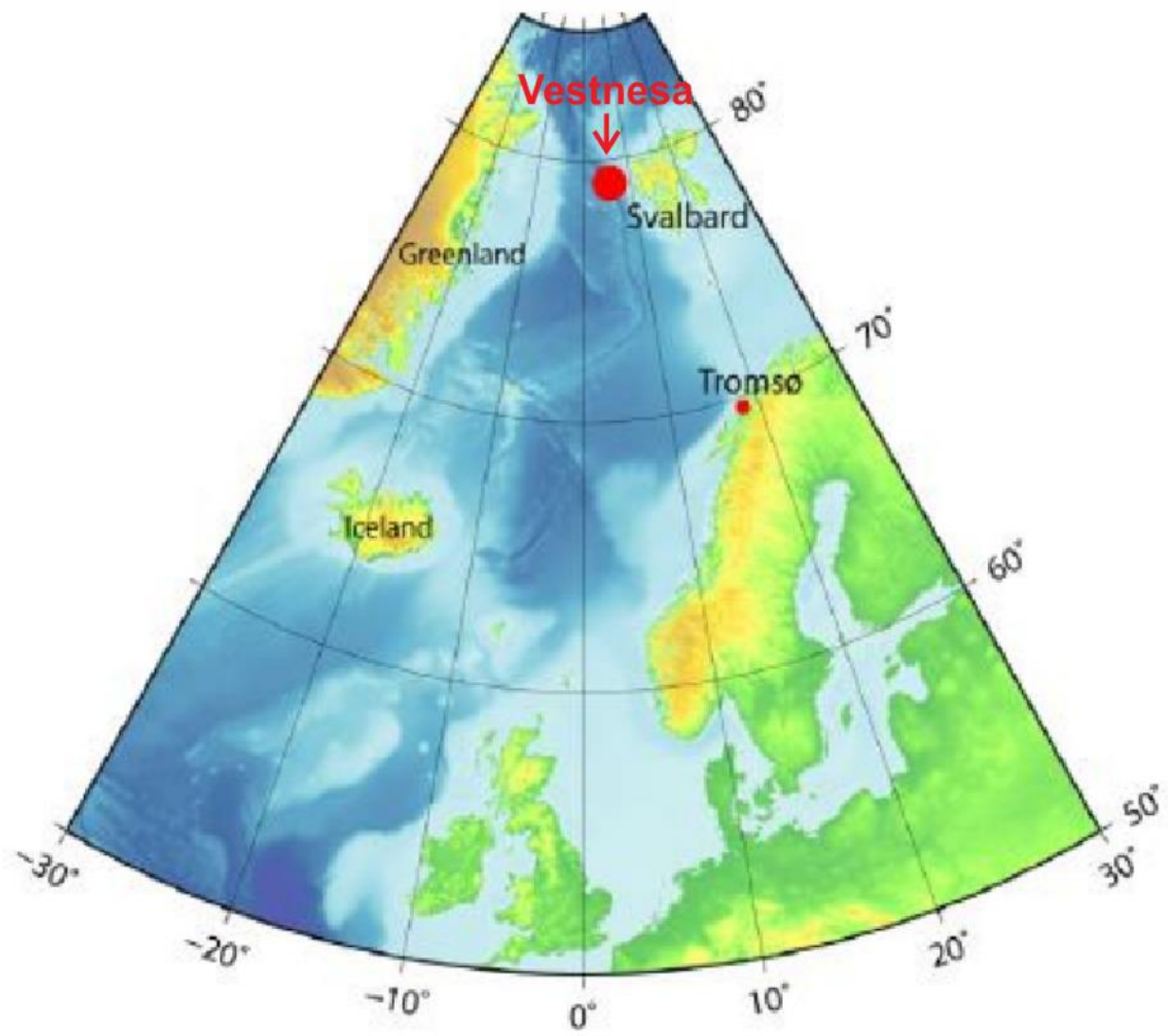
Figure 2: Illustration of study area Vestnesa Ridge, Svalbard. Modified from (Petersen, et al., 2008).

1.3 Study area

Vestnesa Ridge is located northwest of Svalbard in the eastern Fram Strait at approximately 79-80°N. Fram Strait has for a long time been acknowledged as the most important link connecting the Nordic Seas and the Arctic Ocean (Rudels, et al., 2000; Walczowski, et al., 2005). Fram Strait is located in the predominant route for water and heat exchange between the world's ocean and the Arctic Basin and acts as a connection point between the Arctic and the Atlantic Ocean (Bylinskaya, et al., 2016). The cold Arctic and warm Atlantic water mixes and generates Arctic water masses which influences the thermohaline circulation and in turn influences paleoenvironmental changes and the climate (Bylinskaya, et al., 2016). The Atlantic and Arctic waters are separated by the Arctic Front, while the Polar Front marks the boundary between Polar and Arctic surface waters (Figure 3) (Walczowski, et al., 2005). Increased volume of Atlantic water flowing into the Arctic Ocean is linked with considerable sea ice retreat and alteration of the thermohaline structure (Zhang, et al., 1998; Dickson, et al., 2000; Karcher, et al., 2003). The transportation of the saline and warm water brought northwards by the Meridional Overturning Cell exerts a major control on the climate in the Nordic Seas (Walczowski, et al., 2005).
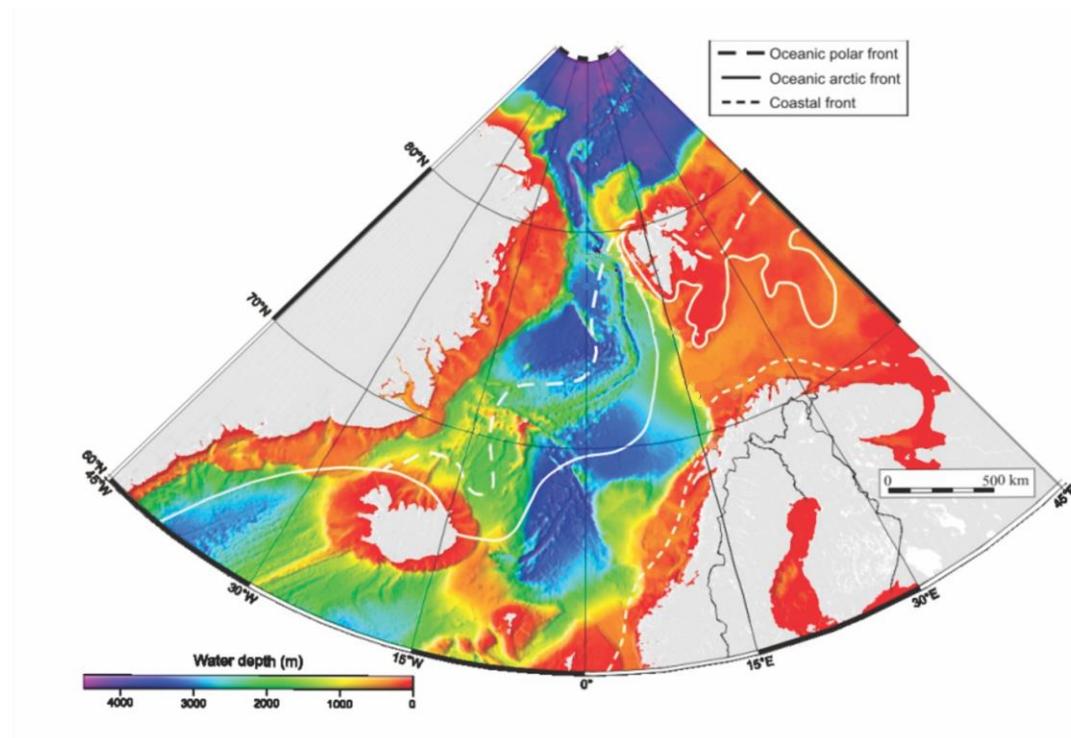
Figure 3: Illustration of the oceanic polar front, oceanic arctic front and coastal front. Modified from (Husum & Hald, 2012).

The cold East Greenland Current and the warm West Spitsbergen current are the two dominating surface current in this area (Figure 4) (Aagaard, et al., 1987). The East Greenland current transports fresh and cold water from the Arctic regions close to the East Greenland margin into the North Atlantic Ocean (Aagaard, et al., 1987). The majority of the Atlantic Water circulates in the Nordic Seas and moves southwards with the East Greenland Current as Atlantic Intermediate Water (Perkin & Lewis, 1984; Quadfasel, et al., 1987; Bourke, et al., 1988). The current contributes to sustain ice-free conditions in the eastern part of Fram Strait for most parts of the year and transports salt and heat to the Arctic Ocean (Aagaard, et al., 1987; Walczowski, et al., 2005). This current is important for the transport of heat and salt to northern latitudes and is crucial for the formation of deep water in the Nordic Seas (Aagaard, et al., 1985). It generally moves along the continental slope of the Barents Sea because of the topography in the area (Hopkins, 1991). The Nordic seas overflow generated from deep convection in the Nordic Seas contributes to the formation of North Atlantic Deep Water (Aagaard, et al., 1985). Further input of fresh water to the system is assumed to cool the North Atlantic region and reduces the formation of deep water (Bluiner & Brook, 2001). Comparing and correlating the flow of Atlantic Water to the Polar Water is closely connected to the advance and retreat of ice sheets (Jessen, et al., 2010).
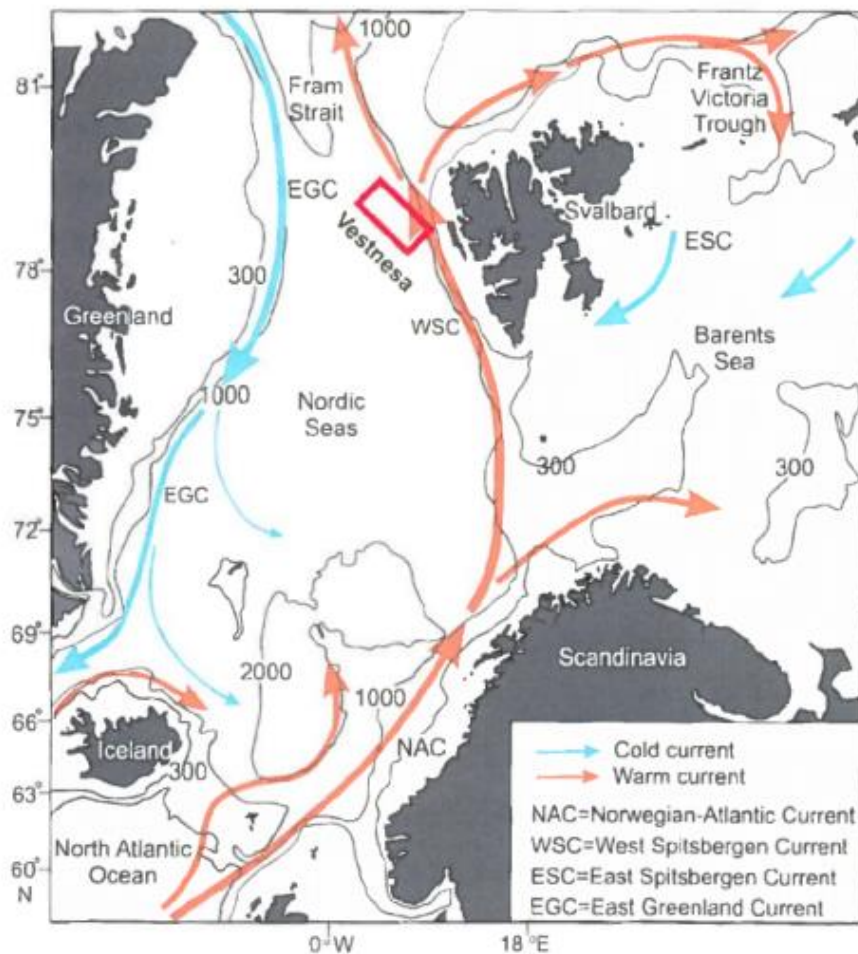
Figure 4: Illustration of the dominant currents in the Barents Sea and the Nordic Sea. The location of the study area is in within the red box. Modified from (Rasmussen, et al., 2007).

Vestnesa Ridge is located on young oceanic crust which is considered to be <20 Ma. It is situated on the segment spreading eastwards of the Molloy Fracture Zone, which is connected to the northern part of the Mid-Atlantic Ridge system (Hustoft, et al., 2009a). Several pockmarks are found on the Vestnesa Ridge, which is suggested to be linked with methane venting and release in this area (Hustoft, et al., 2009a; Bunz, et al., 2012; Plaza-Faverola, et al., 2015). Methane venting at this site might be caused by tectonic stress and glacial activity (Plaza-Faverola, et al., 2015). The presence of gas hydrates is indicated by a bottom-simulating reflector 160-180 meters underneath the seabed (Hustoft, et al., 2009a; Bunz, et al., 2012). Sediments located in the western Svalbard region generally dates from the Late Pliocene to Quaternary period consisting of several glaciogenic Trough-Mouth Fans and areas with inter-fan sediments over the bedrock (Faleide, et al., 1996; Solheim, et al., 1998). Studies of seismic data from the pockmark have shown vertical pathways enabling gas to go through the hydrate stability zone and reach the seafloor (Bunz, et al., 2012).

5

HH16-549GC is retrieved from within a pockmark in Vestnesa Ridge at a water depth of 1207 meters. Pockmarks are craters formed in fine-grained and soft sediments located at the seafloor and is an area where pore fluids and gas seepage is assumed to occur (Judd & Hovland, 2007).

Marine Isotope Stages (MIS) can be characterized by investigating $\delta^{18}O$ values from stable isotope analysis (Lisiecki & Raymo, 2005). MIS 2 is suggested to occur from 29 ka to 14ka (Lisiecki & Raymo, 2005) and is characterized to with very fluctuating sea surface conditions due to alterations in advection of Atlantic water masses towards higher latitudes (Hebbeln, et al., 1994). Seasonally ice-free environments were present as a result of further inflow of saline and warm Atlantic water masses leading to destabilization the ice sheets in the Svalbard-Barents Sea leading to occasional discharge of meltwater (Hebbeln, et al., 1994; Nørgaard-Pedersen, et al., 2003; Rasmussen, et al., 2007). The transition from MIS 1 to MIS 2 is expected to occur as the $\delta^{18}O$ drops significantly 14 ka (Lisiecki & Raymo, 2005). The shift from MIS 2 to MIS 3 occurs at 29 ka and is regarded to appear at the end of Heinrich event 3 when the concentration of planktic and benthic foraminifera is very low (Chauhan, et al., 2014). Heinrich events are characterized as recurring events where the icebergs break off the glaciers (Heinrich, 1988). These cycles occur every 6000-10,000 years (Heinrich, 1988). Jessen et al (2010) suggest that Heinrich events transpire around 16,500 and 24,000 cal years BP in western Svalbard.

Elverhøi et al (1995) suggest that the Barents Sea Ice Sheets progressed towards the shelf edge in two phases (Figure 41). Increased concentration of IRD and decreasing $\delta^{13}C$ values indicate that the ice sheets advanced towards the shelf at 27,000 cal years BP (Jessen, et al., 2010). Enhanced precipitation and open-water conditions between the North Atlantic Ocean and Fram Strait characterizes the growth of the Barents Sea Ice Sheets in the period from 27,000 to 22,500 cal years BP (Hebbeln, et al., 1994). The western shelf of Svalbard is anticipated to be completely glaciated at 23,800 cal years BP, which occurs in a period defined as the Last Glacial Maximum (Jessen, et al., 2010). The deglaciation of the Svalbard margin is predicted to start at 20,000 cal years BP (Jessen, et al., 2010), and is proposed to occur in two acts which occurred from 17,500 at 14,800 cal years BP (Elverhøi, et al., 1995). The ice sheets is suggested to retreat rapidly at the warm Bølling-Allerød interstadials starting in 14,700 cal years BP (Jessen, et al., 2010), which may be explained by an enhanced solar radiation and increasing sea level in this period (Figure 43) (Laskar, et al., 2004; Peltier & Fairbanks, 2006) and enhanced inflow of the Atlantic Water (Hald & Aspeli, 1997).

Lower salinity and bottom water temperatures occurring from 12,600 to 11,700 cal years BP characterizes the relatively cold Younger Dryas (Slubowska-Woldengen, et al., 2007). The early Holocene starting in 11,700 cal years BP experienced warmer temperatures due to increased inflow of Atlantic water and thermohaline circulation along with enhanced insolation from the sun (Slubowska-Woldengen, et al., 2007) which reduced the extent of the glaciers substantially (Svendsen & Mangerud, 1992). Figure 5 illustrates the development of the ice sheets from 20,000 to 14,000 cal years BP.
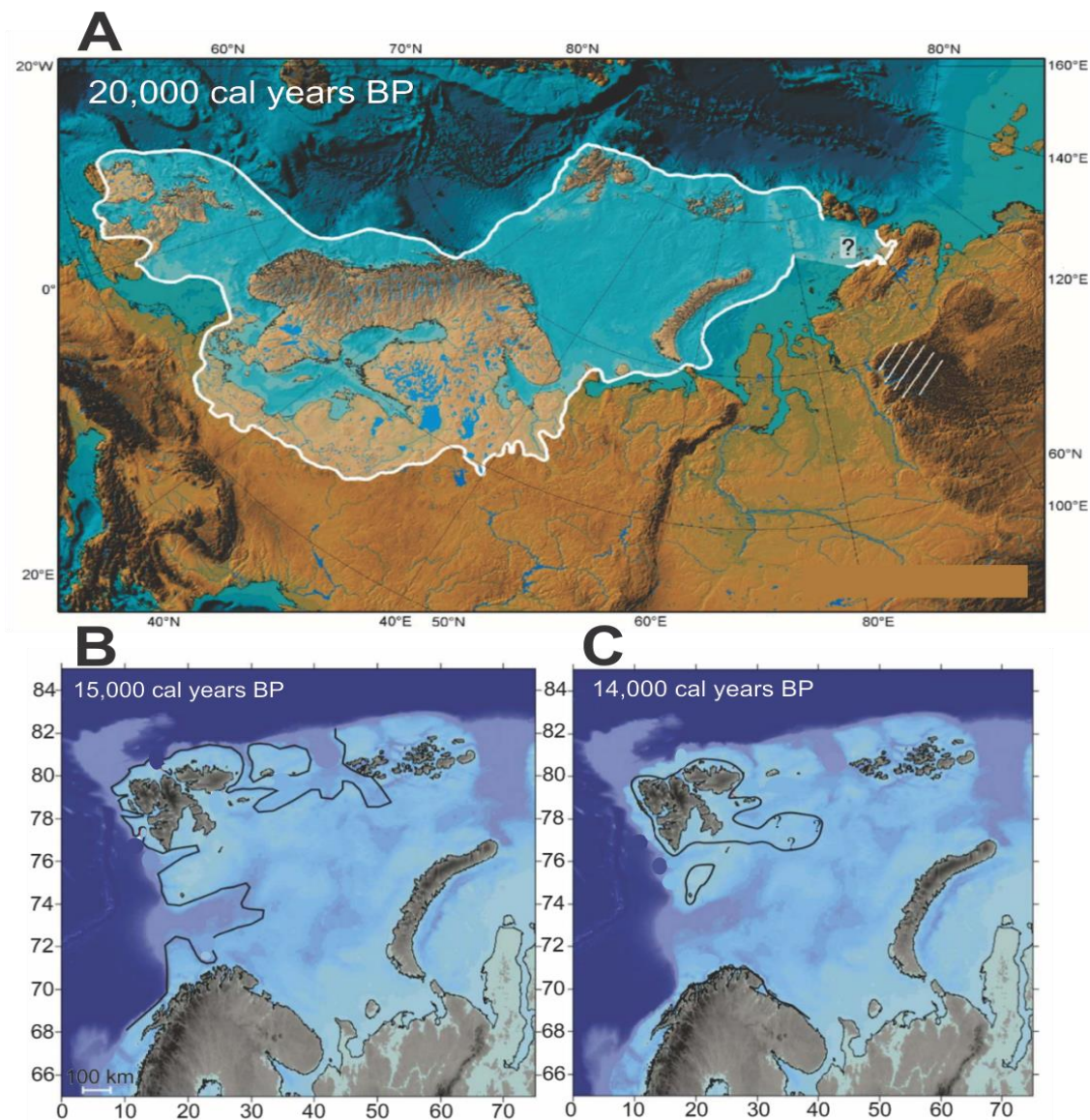
*Figure 5: **A**: Reconstruction of the Eurasian ice sheets at 20,000 cal years BP. The white line illustrates the extent of the ice sheets. Modified from (Svendsen, et al., 2004). **B**: Reconstructed ice-margin at 15,000 cal years BP. The black line shows the range of the ice Modified from (Kristensen, et al., 2013). **C**: Reconstructed ice-margin at 14,000 cal years BP. The black line displays margin of the ice sheets. Modified from (Kristensen, et al., 2013).*

1.4 Methane gas hydrates

Methane can be found as gas hydrates, dissolved gas or free gas located at continental margins across the world (Kvenvolden, 1988; Kvenvolden, et al., 1993; Milkov, 2004). The two main sources of methane emissions in the Arctic region is assumed to come from discharging methane gas hydrates as the climate warms, and from methane originating from microbial degradation of organic carbon as permafrost thaws (Isaksen, et al., 2011). Methane hydrates is defined as a substance similar to ice that develops when water and methane merges at low temperatures up to 25°C and moderate pressure larger than 3-5 MPa in areas with sufficient amounts of gas and water (Sloan, 1998; Ruppel, 2011) and is described as molecules of natural gas trapped inside ice (Demirbas, 2010). They often exist within a gas hydrate stability zone (GHSZ) (Figure 6) near the continental margin in marine sediments (Demirbas, 2010). Ruppel et al 2011 suggest that the deep ocean comprises 95% of the hydrate reservoirs worldwide. Compared to gas at standard temperature and pressure, methane hydrates can contain methane by a quantity of 164 times more on a volumetric basis, meaning that a small amount of gas hydrate can produce a large amount of gas (Ruppel, 2011). Gas hydrates are estimated to contain about two times more carbon in comparison to every other fossil fuels combined which includes oil, natural gas and coal (Demirbas, 2010). These vast storages of carbon makes methane gas hydrates a very interesting field to exploit in order to use for purposes to meet the demand of energy in the world (Krey, et al., 2009; Demirbas, 2010). However, it is important to be careful because these gases are greenhouse gases that may disturb the natural balance of greenhouse gases in the atmosphere which can potentially disturb the climate of the Earth causing considerable positive carbon-climate feedbacks (Krey, et al., 2009; Demirbas, 2010).
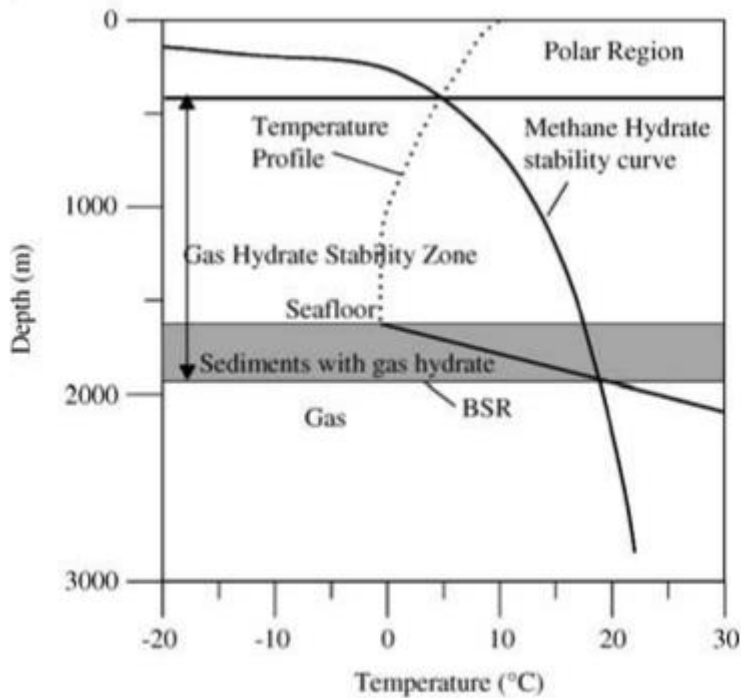
Figure 6: Hydrate stability field for polar regions. (Chand & Minshull, 2003).

Methane hydrates are often located in areas with high biological production (Demirbas, 2010). In marine reservoirs methane forms as a result of degradation of organic matter via microbial methanogenesis or thermogenesis (Whiticar, 1999; Demirbas, 2010). It is important to understand the role of methane in the global carbon cycle as it has a major impact on both the ocean and the atmosphere (Judd, et al., 2002; Kvenvolden, 2002; Dickens, 2003). The Arctic region is believed to contain vast amounts of methane hydrates, but the understanding of these hydrates and the impact they might have on the global carbon budget is not well understood (Biastoch, et al., 2011). The Arctic region is considered to be very sensitive to the ongoing climate change and is expected to have more dramatic effects than in other areas (Screen & Simmonds, 2010; Spielhagen, et al., 2011; Kretschmer, et al., 2015). In the eastern part of the Vestnesa Ridge, studies have registered methane emission in water depths of more than 800 meters. Numerous gas plumes have also been identified in Vestnesa Ridge, which might indicate increased activity of methane gas as it has been interpreted to occur as a consequence of the continuous climate changes in the Arctic region (Westbrook, et al., 2009). It is therefore important to study emissions of methane from the seafloor in relation to natural climate change through time (Bunz, et al., 2012; Smith, et al., 2014).

Studies of seismic data located underneath the pockmarks reveal signs of gas leaking to the seafloor through the hydrate stability zone as possible pathways for gas migration (Bunz, et al., 2012). It is difficult to detect exactly where gas emissions from the eastern part of the Vestnesa Ridge are coming from. The leading hypothesis could be that the gas originates from dissociation from gas hydrates beneath the gas hydrate stability zone or as a mix from shallower and deeper processes through faults and cracks in the subsurface (Figure 7) (Bunz, et al., 2012; Smith, et al., 2014). Further melting of gas hydrates may cause increased concentration of methane in the western Svalbard region (James, et al., 2016).
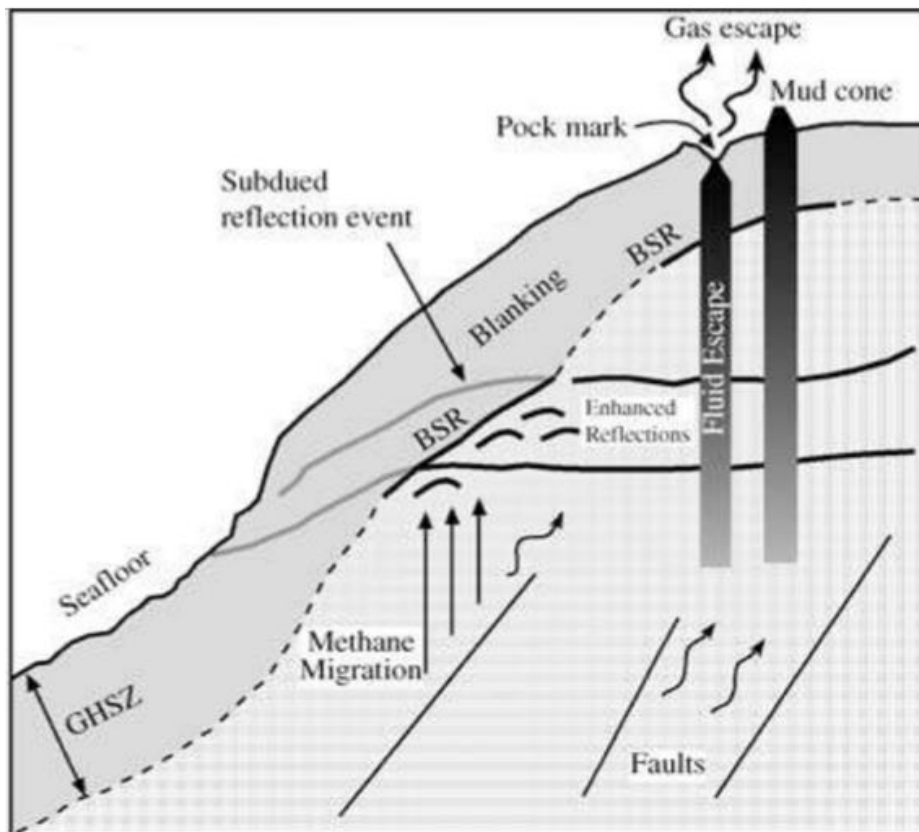
Figure 7: Features of gas hydrates on a passive continental margin. Gas hydrate stability zone (GHSZ) and bottom simulation reflection (BSR) and how they are linked with other features associated with gas migration (Chand & Minshull, 2003).

The structure of the gas and appearance of salts and other elements in seawater is affecting the pressure and temperature conditions for the stability of the hydrates (Desa, 2001). Natural hydrates can develop when the pore water is fully saturated with methane. This occurs when there is a substantial upward flux of methane or when there is a sufficient amount of organic matter in the sediments to develop enhanced methanogenic decomposition (Desa, 2001).

Figure 8 illustrates several different sources of methane and how they may be discharged to the atmosphere through various processes.
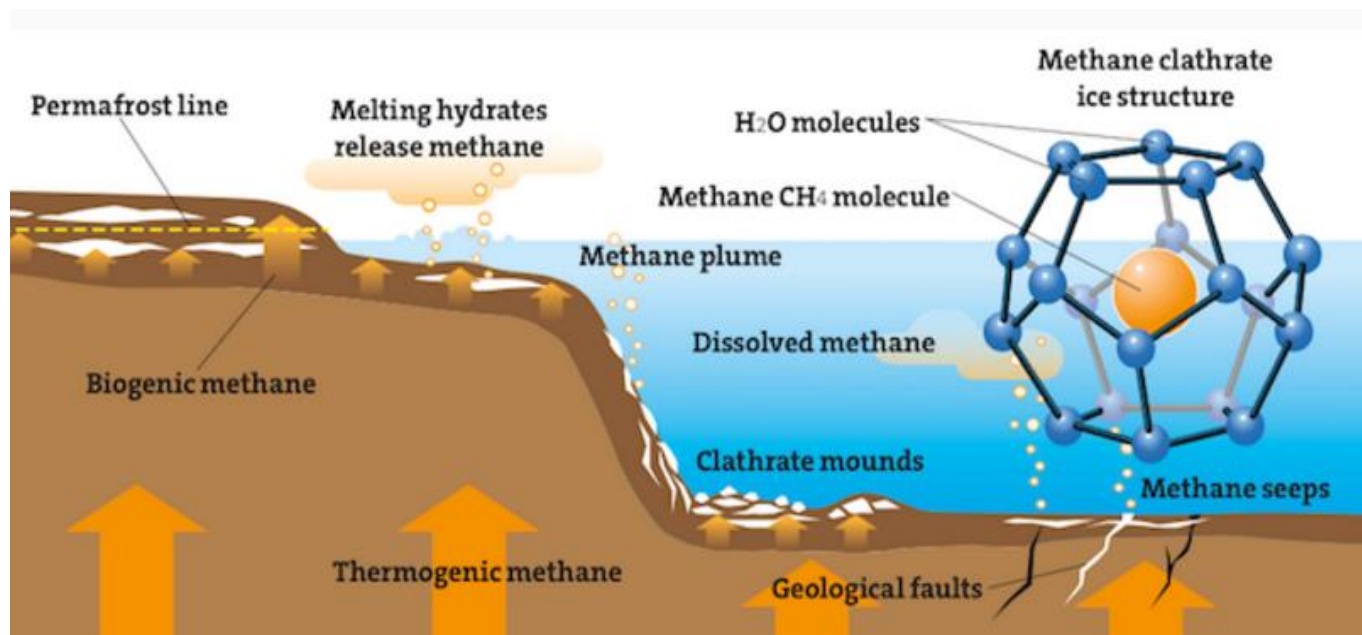
Figure 8: Methane hydrates and various ways methane can dischargee to the atmosphere from several different sources. The source of methane can either be biogenic or thermogenic. (Kimantas, 2014).

By examining the bottom-simulating reflector (BSR), we can identify the base of the gas hydrate stability zone (Figure 7). A negative acoustic impedance contrast is generated when the overlying sediments are in contact with gas hydrates and sediments containing free gas (Shipley, et al., 1979; Maslin, et al., 2010). Methane leaking from dissociating gas hydrates or emerging from free gas below the bottom-simulating reflector may rise towards the seafloor as bubbles, remain trapped as gas or dissolve in pore waters (Archer, 2007). The initiation and formation of the fluid flow are probably caused by pressure due to the loading of shelf ice glaciation and glaciogenic sediments in the mid-Norwegian margin. These reactivation processes and gas emissions are likely to develop in periods of rapid climatic changes (Hustoft, et al., 2009b; Plaza-Faverola, et al., 2011). Chimneys generally occur as a network of connected fractures of smaller scales derived from natural hydraulic fracturing (Figure 9). The formation of chimney structures is linked to various geological processes (Arntsen, et al., 2007). The chimneys have weakness-zones where the fluid flow finds their pathway in the subsurface. The fractures may be filled with gas hydrates in areas with deep-water (Kim, et al., 2011).
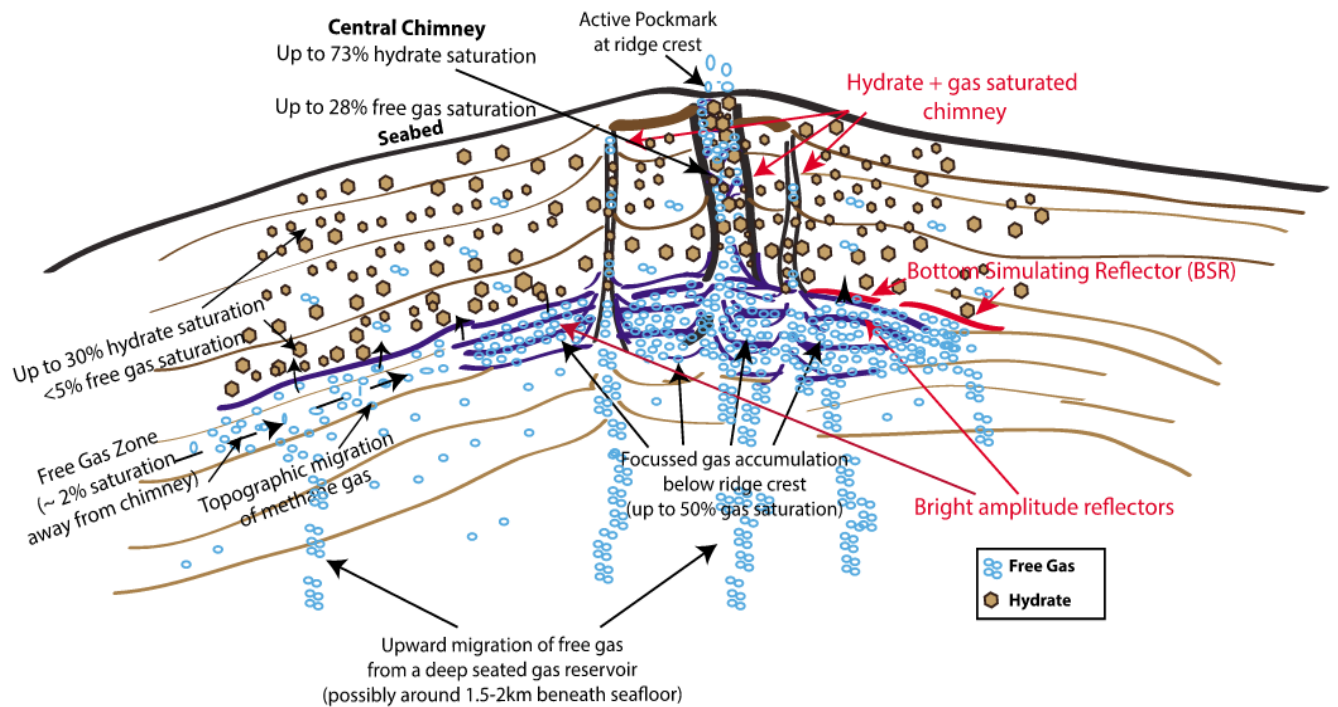
Figure 9: Illustration of the gas hydrate system in Vestnesa Ridge from CSEM and seismic data. (Goswani, et al., 2015).

The hydrates will become less stable when the hydrostatic pressure on the sediments decrease as a result of sea level fall and deglaciation in permafrost regions. This process might lead to further release of methane to the atmosphere and cause a positive climate feedback leading to increased warming of the climate (Desa, 2001). Rising sea levels is likely to cause melting of ice in higher latitudes and will eventually lead to larger hydrostatic pressure on the sediments and is regarded as a negative climate feedback, which is likely to decrease the dissociation of methane from hydrates (Desa, 2001). However, it is worth mentioning that the increased pressure from a sea level rise of 1 meter is inadequate in comparison to the consequences of the predicted warming of the ocean (Maslin, et al., 2010). Warming of the ocean could destabilize the hydrates leading to further release of methane to the atmosphere (Figure 10) as changes in surface climate in turn affects the temperature of the deep ocean (Krey, et al., 2009; Maslin, et al., 2010; Kretschmer, et al., 2015).
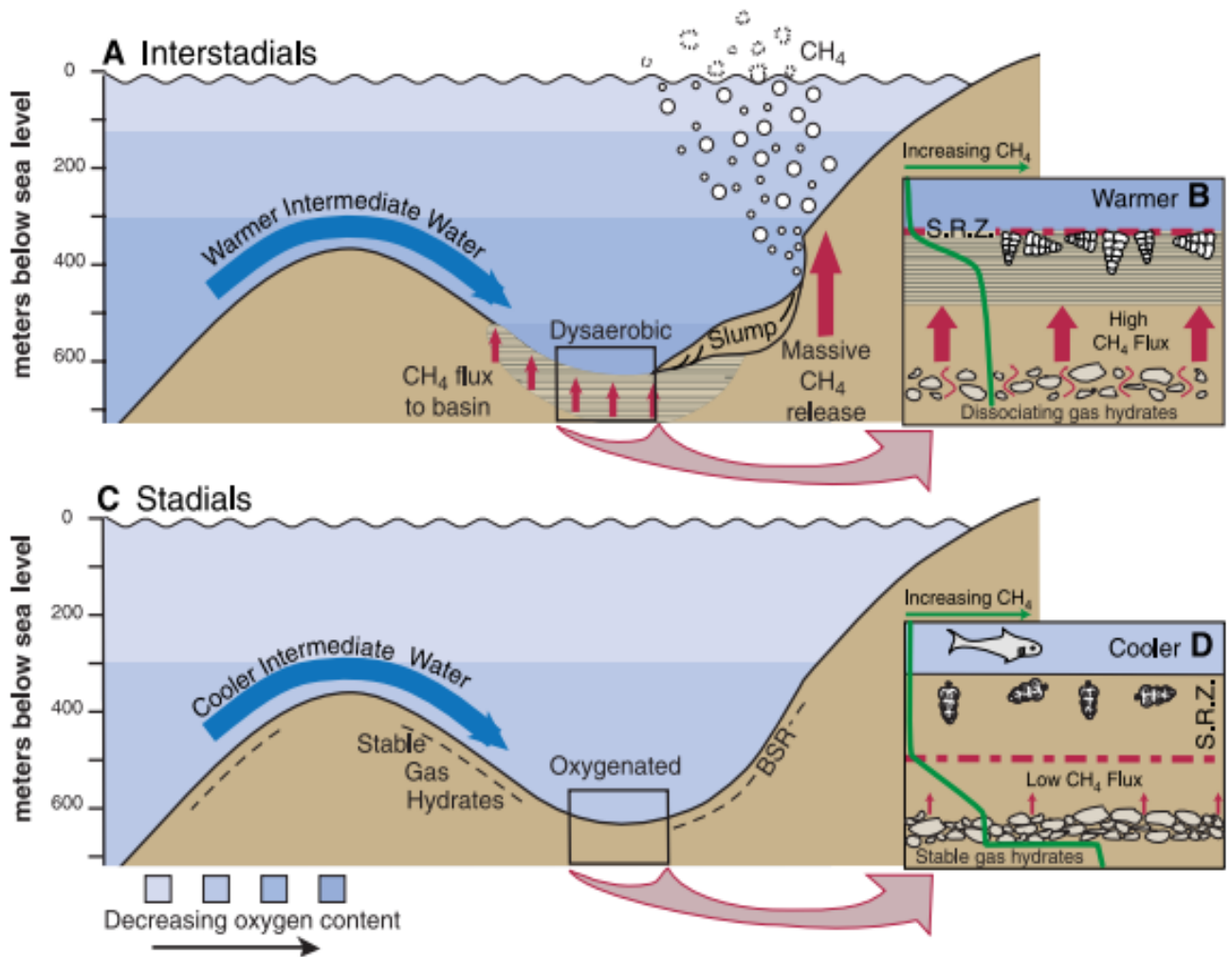
Figure 10: Illustration of methane flux during interstadial and stadial periods in Santa Barbara Basin. Warmer intermediate water influences the stabilization of the gas hydrate making it more unstable, which may lead to an enhanced methane flux upwards. The gas hydrates become more stable during stadials because of cooler intermediate water. In this period the flux of methane going upwards will be diminished. Cooler intermediate water stabilizes the gas hydrates (Kennett, et al., 2000).

The stability of methane hydrates is likely to be altered by varying temperatures, changing flow direction and alterations in ocean currents (Kretschmer, et al., 2015). The primary stability parameters for gas hydrates are low temperature and high pressure, if one of these parameters adjusts the stability will either increase or decrease (Archer, 2007). Instabilities in the hydrates could lead to tsunamis and massive landslides (Figure 11) (Maslin, et al., 2010).
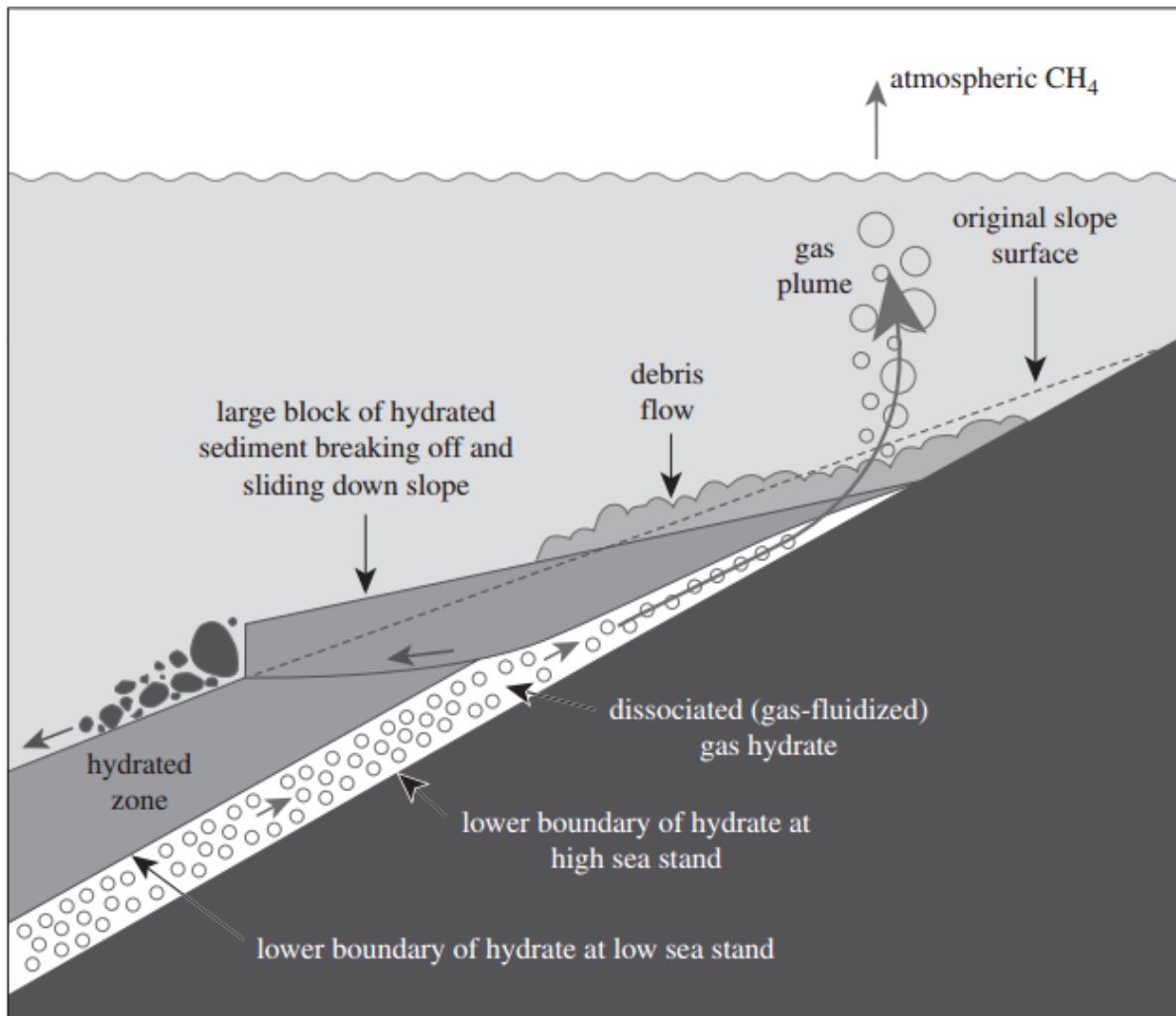
Figure 11: Illustration of the possible consequences following a slope failure over a gas hydrate layer. Large volumes of gas might discharge as a result of this failure (Maslin, et al., 2010).

New research suggest that the gas hydrates up to 400 meters in water depth have already been influenced by the ocean warming in the Arctic Ocean (Shakhova, et al., 2010; Ferré, et al., 2012; Berndt, et al., 2014). Factors responsible for enhanced methane release can be increased seismic activity due to rapid deglaciation, variations in sea-level, higher sediment supply to the seabed and increased temperature in bottom-water after the recession of ice sheets (Judd & Hovland, 2007). These processes lead to increased pressure on the pores, which in turn induces increasing gas venting from the seafloor. However, considering that Vestnesa Ridge is located a long distance from the shelf edge, it is unlikely that increasing load of glaciogenic sediments has a big impact on the gas emissions (Ottesen, et al., 2005; Mattingsdal, et al., 2014). Models of methane flux from the continental shelf and slope in western Svalbard suggest that further warming of the ocean will lead to further methane discharge in the coming years (James, et al., 2016). Over 10% of direct methane emissions to the atmosphere in this region is estimated to come from offshore western Svalbard (James, et al., 2016). Migration of methane to the surface is constrained as a result of higher input of fresh water in Arctic shelf seas leading to increasing stratification in the water masses (James, et al., 2016). It is also important to note that increasing stratification may potentially also lead to more dissociation from the hydrates as a result of warming of sub-pycnocline waters (James, et al., 2016).

During ice-covering periods, the sea ice acts as a natural obstacle to emissions of methane from the sea floor (Shakhova, et al., 2015). Increasing temperatures in the Arctic region is likely to cause longer seasons with less ice cover and more open water (Shakhova, et al., 2015). Enhanced emission of methane is likely to occur as a result of longer periods with open water and increased wind speed due to more events of extreme weather (James, et al., 2016). This process might lead to greater mixing in the deep ocean as a result of a greater boundary between air and sea surface, which in turn can ventilate transportation of bubbles and dissolved methane in the water column (Shakhova, et al., 2015). The bubble-mediated storm-induced methane may force a bigger portion of methane to surpass the aqueous microbial filters and enter the atmosphere as a result of this process (Shakhova, et al., 2015). Methane can only have an impact on global climate if it migrates through the microbial filter and enters the atmosphere (Kretschmer, et al., 2015).

The stability of methane hydrate reservoirs are delicate to the current climate warming, but there are large uncertainties of the consequence of further release of methane from sediments (James, et al., 2016). The relation between the climate of the Earth and gas hydrates requires additional research as the system is complex and not well understood (Desa, 2001). Higher latitudes are especially vulnerable to increasing temperature due to the current climatic changes (Intergovernmental Panel on Climate Change, 2013). Considering that methane is expected to contain 3000 times more methane in methane hydrates than in the atmosphere means that a rapid melting of methane gas hydrates might have a massive impact on the climate and are therefore considered to be a significant concern (Demirbas, 2010; Maslin, et al., 2010).

1.5 Methane seeps

Cold seeps often occur where networks of fractures and faults make a channel where methane-rich fluids are allowed to pass through towards the ocean floor on the continental margins (Paull, et al., 1995; Pohlman, et al., 2009). Strong discharges of fluids may alter the morphology by forming features like mud volcanoes, pingos and pockmarks on the ocean floor *(Judd & Hovland, 2007)*. These features are often related to the discharge of free gas migrating through the water column (Paull, et al., 1995; Suess, et al., 1999). In order to indicate fluid flow in these regions, it is useful to investigate authigenic carbonates and rich chemosynthetic communities (Sibuet & Olu, 1998; Levin, 2005).

Methane ascends through fractures, faults, strata and cracks in solution. It will rise as gas if the pore waters in the sediments are supersaturated (Judd & Hovland, 2007; James, et al., 2016). Greater pressure in the sediments with low permeability is likely to be caused by increased dissociation of the hydrates, which generates cracks and induces slumping and collapse structures (James, et al., 2016). Methane discharged from the seabed migrates through the water column as bubbles (Figure 12). The bubbles of methane may be released from the seabed without leaving any remarkable traces in the water column or dissolve within the water column (Shakhova, et al., 2013). The dissolution of the bubbles depends on the release intensity, rise velocity and the size of the bubbles (Shakhova, et al., 2013). Larger bubbles are able to carry methane through hundreds of meters, whereas smaller bubble dissipates near the ocean floor (Figure 13) (James, et al., 2016).

In the Arctic region, the bubbles are less likely to reach the atmosphere at water depths over 200 meters as gas bubbles of relatively large size (5 mm) is likely to be dissipated entirely first 200 meters from the seafloor (James, et al., 2016). It is likely that the methane gas bubbles will vanish 200 meters from the seafloor in this region and therefore not proceed further to the atmosphere (James, et al., 2016).
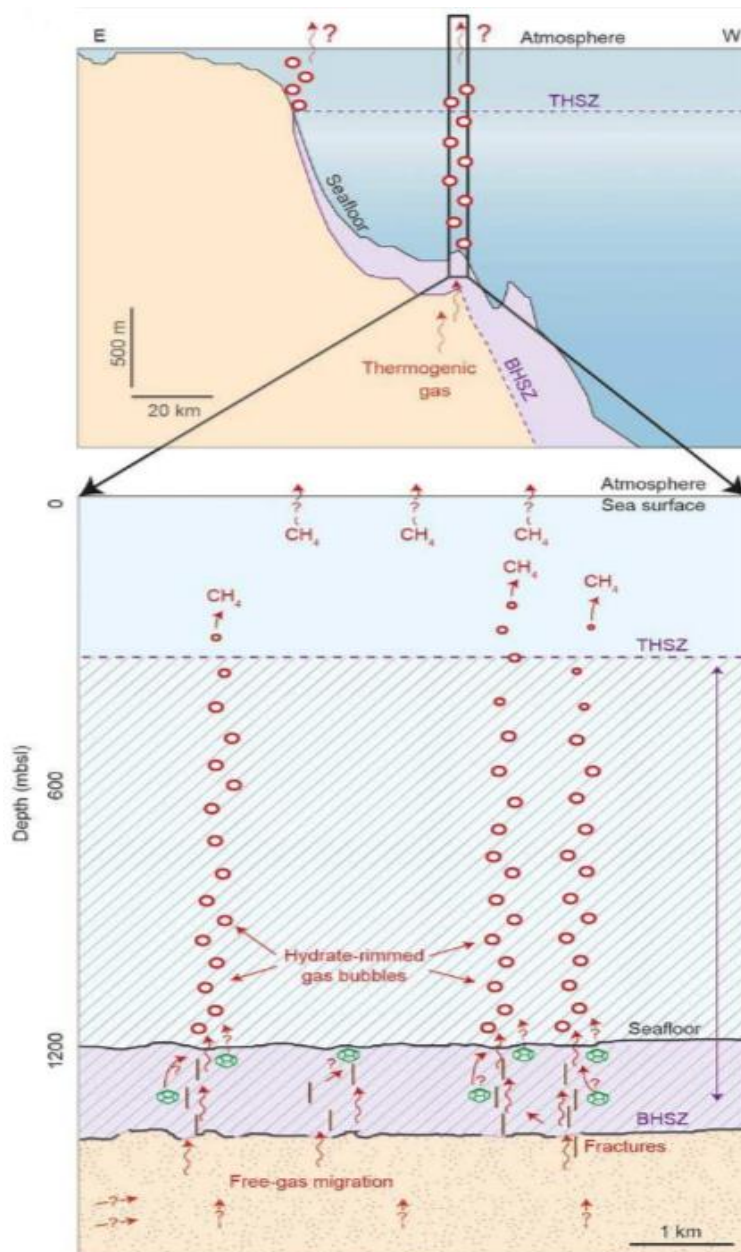
Figure 12: Illustration of the venting system at Vestnesa Ridge and processes occurring from the bottom of the hydrate stability zone (BHSZ) to the top of the hydrate stability zone (THSZ). The red arrows show thermogenic free gas emerging from BSR migrating towards the BSR anticline. The green cages signify gas being sourced from the melting of hydrates in the hydrates stability zone (HSZ) or from hydrothermal activity from the young oceanic crust beneath Modified from (Smith, et al., 2014).
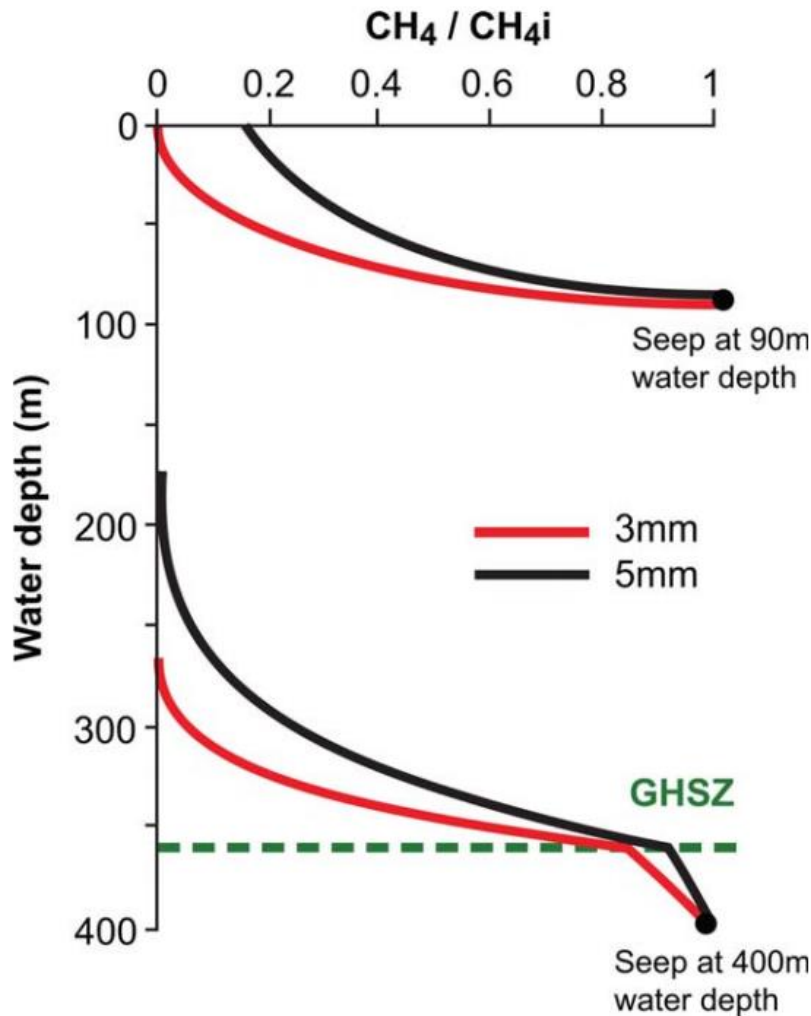
Figure 13: Illustration of the fraction of methane remaining in a gas bubble (CH_4) in relation to the original quantity of methane in the gas bubble (CH_4i). The black curve displays how a 5 mm gas bubble will ascend and the red curve shows how a 3 mm gas bubble will rise towards the surface of the ocean. The dotted green line represents the top of the gas hydrate stability zone.This figure is based on the Arctic continental slope (James, et al., 2016).

The transport of methane to the atmosphere is substantially enhanced by upwelling flow which decreases the residence time of the bubbles and reduces the dissolution (Shakhova, et al., 2013). Bubbling can be an essential contributor to methane emissions to the atmosphere, although it is very difficult to estimate the amount because the seeps often develop in big bubble plumes (Shakhova, et al., 2013). These bubbles can be identified by using backscattered image of the bubbles as is records a noticeable difference in acoustic impedance between the bubbles and the surrounding water (Shakhova, et al., 2015).

There are large uncertainties of how much methane enters the atmosphere from deep marine sediments through the ocean floor. Emitted methane from the seafloor is however regarded to rarely reach the top of the water column or enters the atmosphere (Ruppel, 2011). The rising methane at water depths larger than 100 meters is usually replaced by O_2 and N_2 (Ruppel, 2011). The greenhouse effect of methane gas is diminished by the oxidation of methane in the water column. However, this effect also reduces the amount of oxygen in the water, which makes the ocean waters more acidified and in turn releases more carbon dioxide into the atmosphere (Liro, et al., 1992). Further release of methane in the ocean might therefore affect the marine biodiversity (Westbrook, et al., 2009). Increase bottom water temperatures is likely to result in more dissociation of methane in the water column in the coming years (James, et al., 2016).

1.5.1 Sulfate-Methane transition zone

In the sulfate-methane transition zone (SMTZ), sulfate-depleted and methane-rich sediments below are separated from sulfate-bearing and methane-depleted sediments above (Borowski, et al., 1996; Roberts, 2001). In this area, methane is normally consumed and becomes more oxidized due to anaerobic oxidation (Orcutt, et al., 2004; Treude, et al., 2005; James, et al., 2016). Anaerobic oxidation of methane is considered to be the most crucial process in cold seep environments. The transportation of methane that passes the sulfate-methane transition zone can escape marine sediments through venting in the water column. When methane leaves the marine sediments, it is oxidized by aerobic processes (Hinrichs, et al., 2003; Orphan, et al., 2004). A combination of sulfate-reducing bacteria and archaea transform sulfate and methane to hydrogen sulfide and bicarbonate by the process of anaerobic oxidation of methane (Reeburgh, 1976; Hinrichs, et al., 1999; Boetius, et al., 2000). The sulfate-methane transition zone moves closer to the seafloor when the flux of methane increases (Figure 14) (Borowski, et al., 1996; Bhatnagar, et al., 2011). Methane discharges easier to the water column when the sulfate-methane transition zone is shallow in seep areas with high flux (Paull, et al., 2005; Castellini, et al., 2006).
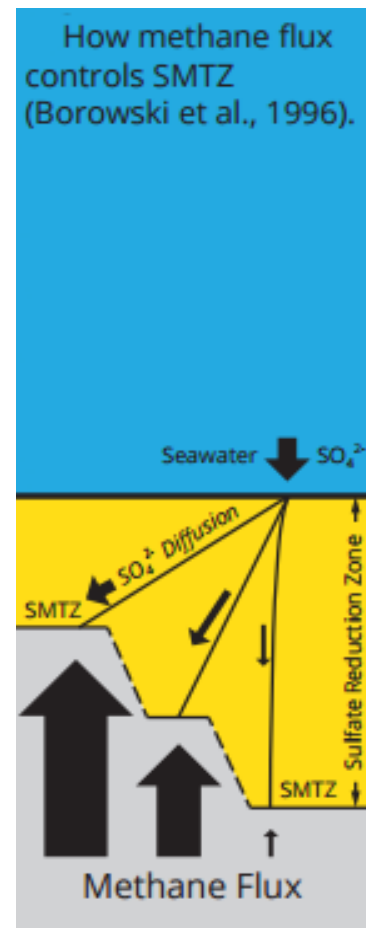
Figure 14: Illustration of how sulfate-methane transition zone profiles is controlled by the flux of methane (Borowski, et al., 1996).

Aerobic and anaerobic oxidation of methane is contributing to a substantial reduction of the flux of dissolved methane (James, et al., 2016). However, the effect of the methanotrophic sink will diminish if the portion of methane flux increases, leading to more methane migrating by advection or in the gas phase (James, et al., 2016). Microbial consumption is considered to be the second largest methane sink on Earth with disaggregation of fecal pellets being the largest (Hinrichs & Boetius, 2002; Reeburgh, 2007).

Up to 90% of the methane is estimated be consumed by anaerobic oxidation in the sediments near the seafloor. Sulfate diffusing the seawater and methane moving against the seafloor reacts simultaneously in the SMTZ in the process of anaerobic oxidation of methane (Reeburgh, 1976). This statement is supported by the equation:

$$CH_4 + SO_4^{2-} \rightarrow HCO_3^- + HS^- + H_2O \quad (1)$$
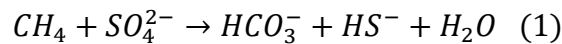
Equation (1) describes the process by methanotrophic archaea and sulfate-reducing bacteria in the sulfate-methane transition zone (SMTZ) (Barnes & Goldberg, 1976; Borowski, et al., 1996; Boetius, et al., 2000; Hinrichs & Boetius, 2002; Treude, et al., 2003; Reeburgh, 2007). The availability of sulfate is restricted by its rate of diffusion from seawater, which makes the SMTZ migrate towards the seafloor as a consequence of swift consumption of sulfate. This happens in regions with significant supply of methane (Borowski, et al., 1996). Calcium carbonate may precipitate as a result of production of bicarbonate from anaerobic oxidation of methane in accordance with the equation:

$$Ca^{2+} + 2HCO_3^- \rightarrow CaCO_3 + CO_2 + H_2O \quad (2)$$
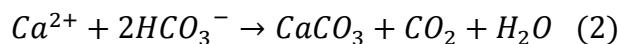
These authigenic carbonates derived from methane occurs as a result of enhanced alkalinity from the accumulation of bicarbonate and generally has negative value of $\delta^{13}C$ (Snyder, et al., 2007; Magalhães, et al., 2012). An illustration of these processes can be seen in figure 15.

Aerobic oxidation of methane develops with oxygen as the terminal electron acceptor in the water column and in surface sediments with abundant oxygen supply (James, et al., 2016).

$$CH_4(aq) + 2O_2(aq) \rightarrow CO_2(aq) + 2H_2O \quad (3)$$
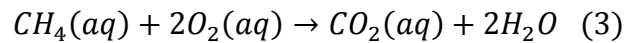
Methane that surpasses the SMTZ is likely to be oxidized in the water column aerobically, if it occurs in shallower water depths it may even be released to the atmosphere (McGinnis, et al., 2006).
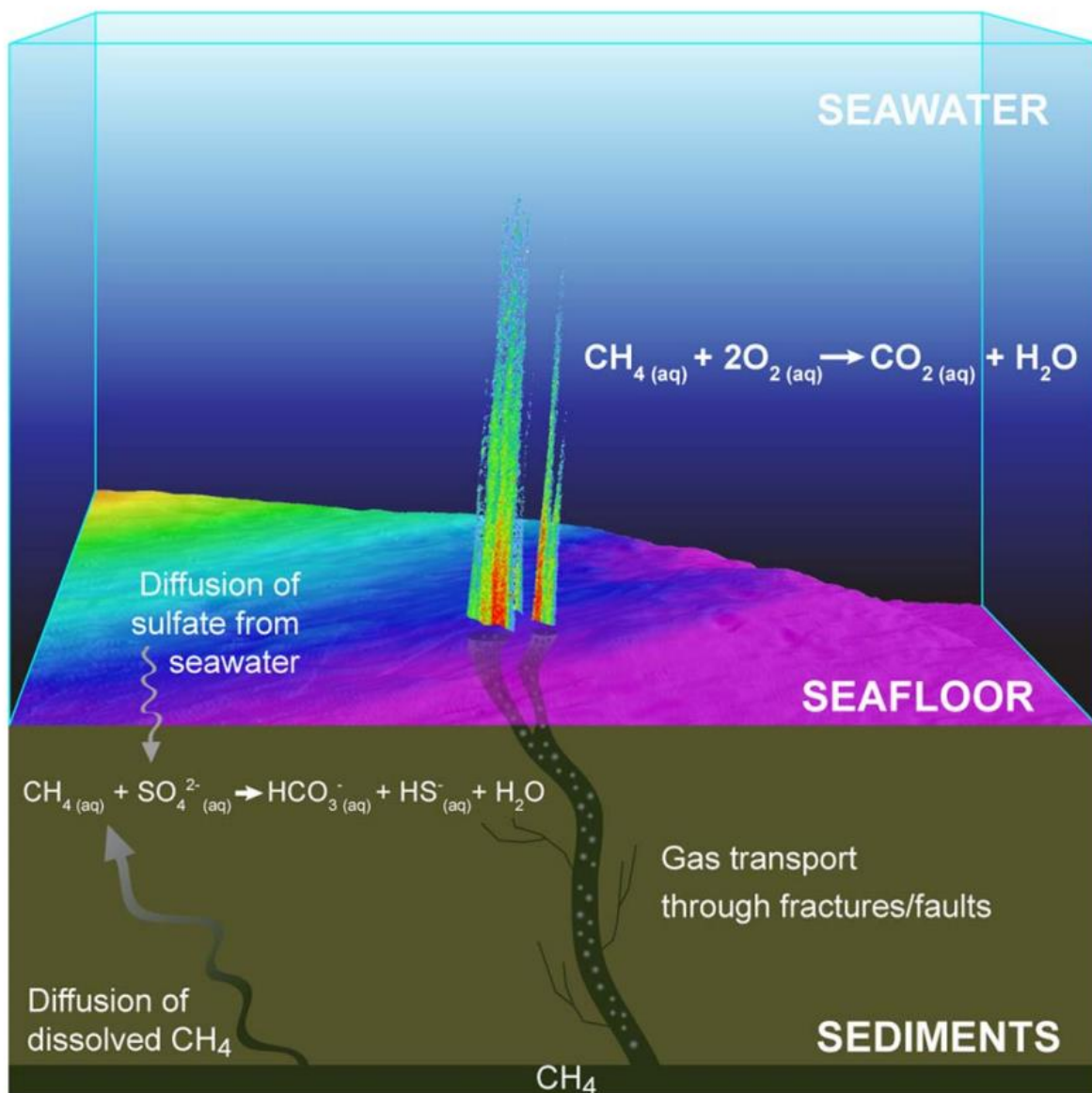
Figure 15: Illustration of how methane can be consumed both by anaerobic ($CH_4 + SO_4{}^{2-} \rightarrow HCO_3{}^- + HS^- + H_2O$) and aerobic ($CH_4 + 2O_2 \rightarrow CO_2 + H_2O$) oxidation. The microbes can only approach dissolved methane meaning the methane in gas form can pass through the oxidation reaction from the microbes (James, et al., 2016).

Dissolved methane in porous sediments migrates as gas by buoyancy in a steady gas phase or as bubbles and by advection or diffusion (James, et al., 2016). Darcy's equation expresses how gas migration and pore-water advection are driven by pressure gradients, and how the gas and fluid viscosity and the permeability of the sediments are influenced by this process (James, et al., 2016). In general there are three ways methane can migrate from the sediments to the water column: 1) Methane being discharged as gas bubbles, 2) Dissolved methane being discharged through the processes of advection and diffusion, 3) Solidified methane hydrates ascending due to the fact that it has lower density than seawater and becoming buoyant when it is removed from the sediments (James, et al., 2016).

Methane is discharged into the water column and possibly to the atmosphere if the flux of methane exceeds the re-supply of sulfate by diffusion from the seawater or exceeds the oxidizing capacity of the microbial consortia (Graves, et al., 2017). Methane can escape oxidation in gas form as it is unavailable for microbes in this state (Graves, et al., 2017), or be transported through the sediments and into the water column as bubbles (James, et al., 2016). Figure 16 illustrates cold-seep methane and carbon fluxes on the continental shelf
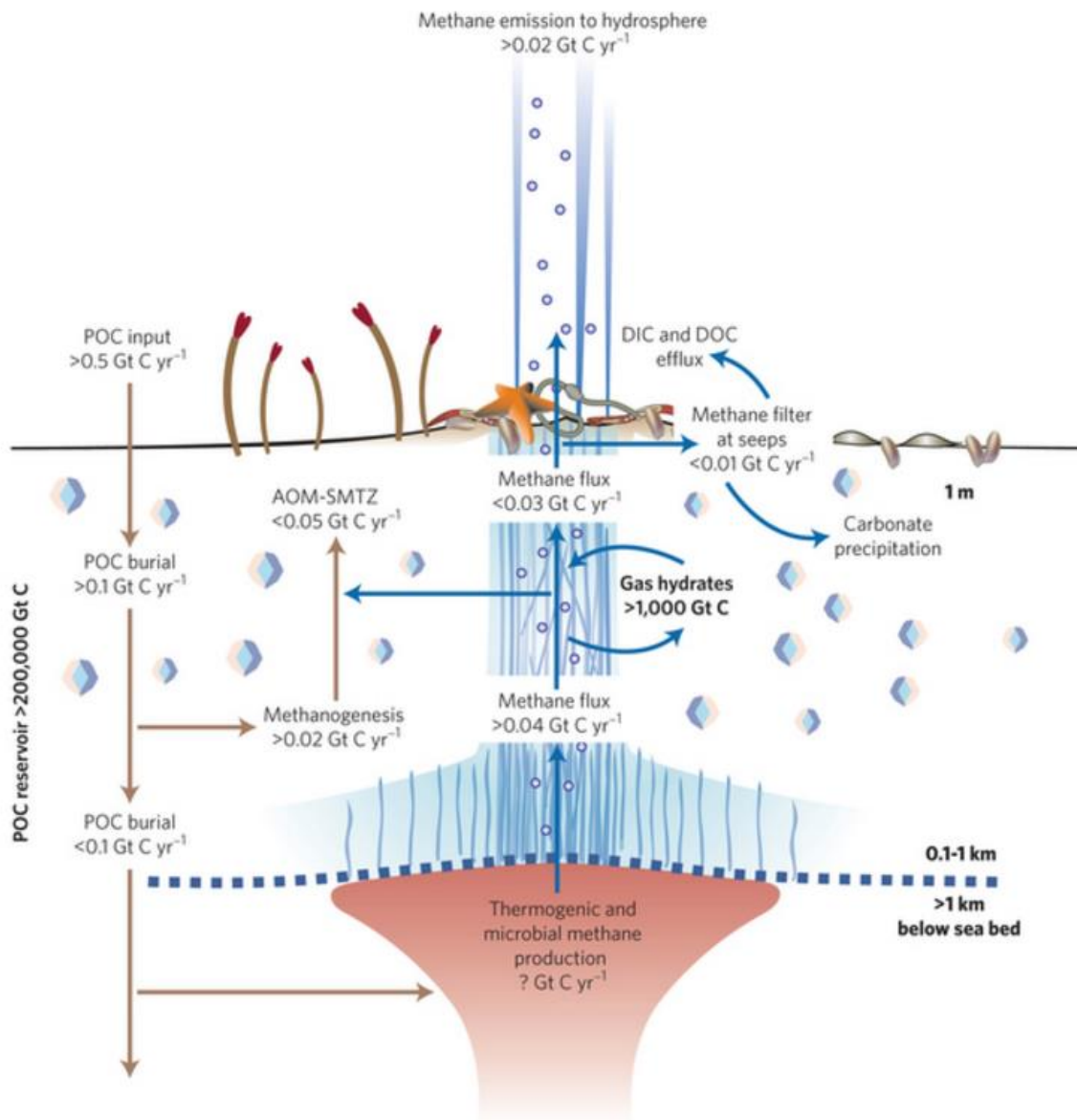
*Figure 16: Illustration of cold-seep methane and carbon fluxes located on the continental slope. Blue arrows indicate fluxes in advective seep systems, Brown arrows indicate fluxes in diffusion driven systems. **DOC**: Dissolved organic carbon. **DIC**: Dissolved inorganic carbon. **POC**: Particulate organic carbon. **AOM-SMTZ**: Anaerobic oxidation of methane in the sulfate-methane transition zone. (Boetius & Wenzhofer, 2013).*

1.6 Methane as a climate gas

Methane gas hydrates are an interesting subject to investigate due to three reasons: 1) Its potential as a new clean energy source, 2) its impact on the atmosphere and 3) the hazard it represents considering that gas hydrates can be a threat to the conventional exploration of hydrocarbon (Demirbas, 2010). Methane might act as a bridge between the world's energy demand and the required reduction in human-induced greenhouse gases as is considered the least carbon-intensive of all hydrocarbons (Krey, et al., 2009).

As the Earth warms up, we might experience a "snowball effect" where warmer climate warms up marine gas hydrates causing the hydrates to be more unstable and release more greenhouse gases to the atmosphere (Demirbas, 2010). A large amount of methane released to the atmosphere can potentially have major impacts on the global climate especially regarding concerns about their long-term stability (Ruppel, 2011). The fourth IPCC assessment report estimate that methane is 25 times stronger as a greenhouse gas than carbon dioxide on a 100-year timescale (Intergovernmental Panel on Climate Change, 2007; Schaefer, et al., 2012). However, the effect of methane might be up to 33 times stronger as a greenhouse gas due to methane's effect on aerosols (Schaefer, et al., 2012). It is also worth mentioning that methane might alter the chemistry of the atmosphere which in turn can enhance the radiative forcing (Lelieveld, et al., 1998). The radiative and chemical balance of the Earth is heavily influenced the amount of methane in the atmosphere and therefore has an impact on global climate change (Intergovernmental Panel on Climate Change, 2001). Figure 17 displays the main greenhouse gases in the atmosphere and their contribution to the greenhouse effect.

Legend:
- N_2O (6 %)
- CH_4 (15 %)
- CFCs (24 %)
- CO_2 (55 %)
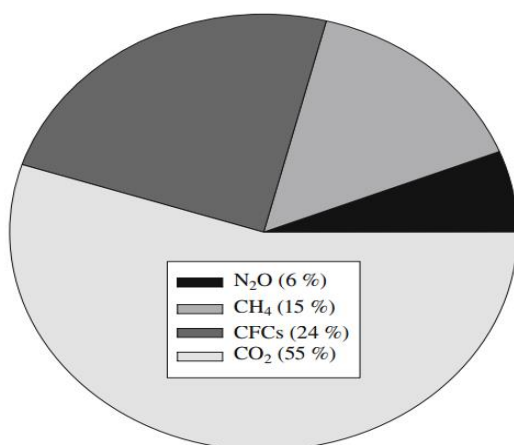
Figure 17: Greenhouse gases and their contribution to the greenhouse effect (Demirbas 2010).

Methane is regarded to be the second largest contributor after carbon dioxide to in terms of global warming historically (Gentz, et al., 2013). Methane emissions from marine seeps to the upper part of the ocean is estimated to be 30 $Tg\ CH_4 yr^{-1}$. However, only 10 $Tg\ CH_4 yr^{-1}$ of these emissions is assumed to enter the atmosphere (Gentz, et al., 2013). The remaining 20 $Tg\ CH_4 yr^{-1}$ left is generally dissolved and microbially oxidized to CO_2 (Gentz, et al., 2013). The growth rate of methane in the atmosphere has generally increased through the 20th century, but it has been relatively stable in the period from 1999-2005 (Metz, et al., 2007). The total budget of methane is dominated by human emissions (Metz, et al., 2007). Over the past 150 years the concentrations of methane has more than doubled from 850 ppb (parts per billion) to 1750 ppb (McGinnis, et al., 2006; Demirbas, 2010). 20% of methane in the atmosphere is estimated to come from thermal decomposition of organic matter and 80% is suggested to occur as consequence of past or present methanogenic activity (Intergovernmental Panel on Climate Change, 2001).

Temperature variability in the Northern Hemisphere is closely linked to the concentration of methane, there are however uncertainties of how changes in concentration are affected by different methane sinks and sources (Möller, et al., 2013). It is anticipated that the increased temperatures due to the discharged methane at the seafloor have a time lag of 30 years in the offshore western Svalbard region (James, et al., 2016). The amount of methane in the atmosphere is not expected to be heavily affected by methane coming from the ocean in this region (Reeburgh, 2007), only 2-4% of the total atmospheric methane concentration is suggested to originate from the ocean (McGinnis, et al., 2006). There are big uncertainties about the quantity of sources of methane to the ocean water column and the estimation of direct water column oxidations rates of methane (Reeburgh, 2007). Further investigation is needed to understand the balance between reactions of microbial oxidation and added methane occurring from the continental shelf (Reeburgh, 2007).

2 Materials and methods

The sediment core HH16-549GC retrieved from Vestnesa Ridge in Fram Strait, west of Svalbard, was investigated in this study. HH16-549GC was collected at a water depth of 1207 meters on a cruise with the research vessel Helmer Hanssen from the University of Tromsø on April 25th, 2016.

2.1 Previous work

The sediment core was collected using a gravity corer. The research vessel Helmer Hanssen employs a gravity corer which consists of a 6-meter steel barrier with an inner diameter of 11 centimeters and a plastic tube (core liner) inside with a diameter of 10 cm. The gravity corer is connected to a wire that can reach water depths up to 3000 meters deep. The gravity corer penetrates the sediments and capture sediments from the ocean floor. A core catcher on the gravity corer makes sure the sediments are contained inside the core liner and does not allow any sediments to leave the system. When the gravity core is on board the ship, the liner is pulled out before it is measured and cut into 1-meter sections to make it easier to handle. It has been reported that the lower parts of the core smelled of gas when it was retrieved. The HH16-549GC core investigated in this thesis was cut into four sections of approximately 1 meter and the last section in 62 cm. The core measures a total of 4,62 meters. After the core was enclosed in plastic caps, it was stored in a cooling room until it was studied further in the laboratory. Table 1 displays further details of the HH16-549GC sediment core. A gravity corer is a useful tool in order to study sediment layers at the bottom of the ocean. The retrieved sediment cores can be studied in order to investigate and reconstruct paleoclimate by examining several different environmental parameters in the sediments recovered in the gravity corer.

Table 1: Location and time for when the core HH16-549GC was retrieved

Station	Location	Latitude (N) Longitude (E)	Water depth (m)	Recovery (cm)	Comment
HH16-549GC	Inner Vestnesa Ridge	79.00.582' 006.54.490'	1207	475	5 Sections

The core has previously been through analyses to determine total sulfur, total carbon and total organic carbon using an equipment called Leco CS-744 at the Geology Lab at UiT the Arctic University of Tromsø. The weight percentage of calcium carbonate ($CaCO_3$) can also be determined by the following equation:

$$CaCO_3 = (TC - TOC) * 8,33$$

The samples were put in a combustion crucible, and later put into a heater with oxygen atmosphere and temperature at 1375°C. This process causes the carbon to be oxidized and decomposed to carbon dioxide, and the sulfur to be oxidized and decomposed to sulfur dioxide. The gases are identified by infrared measurement cells.

The sediment core has also previously been analyzed for pore water data at Geological Survey of Denmark and Greenland (GEUS).

2.2 Laboratory work

The laboratory work on this core was performed at the Faculty of Technology and Science, Department of Geosciences at UiT the Arctic University of Tromsø.

2.2.1 Core Liner Saw

An equipment called Marinetechnik Kawohol sediment liner saw was used to split the core into two halves. The saw is equipped with two vibrating saws moving along the rails which cut the liner on both sides at the same time. The halves were characterized as one work half and one archive half. The work half was the thicker half and was used to take out the samples. This half was later cleaned to describe the lithology of the core. The archive half was the thinner half and was used for imaging, point sensor logging of magnetic susceptibility and colour-scan. Both halves were packed and sealed in plastic bags and stored in cooling rooms to avoid contamination if they needed further studying.

2.2.2 Sieving and weighing

56 samples were taken out from the sediment core. Since the core was 462 centimeters in total, the average distance between each sample taken out was 8,25 centimeter. Each sample was labeled and put in plastic bags before they were weighed to determine the wet weight of the samples. The samples were later put in a freezer and then in a freeze drier (3.2.3) for 24 hours. After the freeze drying process, the dry weight of the samples was measured before they were sieved in fractions of >1000 µm, 500-1000 µm, 100-500 µm and 63-100 µm.

After the samples were sieved, the residues were dried in an oven at 40° Celsius over night. After the residues were fully dried, each sample was weighed in accordance to the different fractions.

2.2.3 Freeze dryer Alpha 1-4 LSC plus
The samples were freeze-dried in a freeze-drying equipment called Alpha 1-4 LSC plus. The samples were frozen and dried in an ice condenser on a heated shelf. After the wet samples had been dried, wet and dry weight as well as water percentage was calculated.

2.2.4 GEOTEK X-ray photography (MSCL-XCT)
Linear digital X-ray images can be obtained by using the Geotek X-ray core imaging system. Radiography is commonly used for doing sedimentological studies in a nondestructive method (Migeon, et al., 1998). It can be used to indicate and investigate sedimentary records and structures as well as bioturbation in the sediment core (Migeon, et al., 1998). By using this tool, we can acquire information about the internal structure of the core by studying variations in lithology, the presence of shells, the degree of bioturbation and ice-rafted debris.

The Geotek MSCL-S is an elemental tool to investigate sediment cores for climatic research. This tool can measure different parameters like magnetic susceptibility, electrical resistivity, gamma density, P-wave velocity and water content. The archive half of HH16-549GC was measured with 1 cm resolution for every 10 seconds.

2.2.5 XRF core scanner
Avaatech XRF core scanner was used to get high-resolution color images of the five sections of the core. To get clear images, the surface of the core was scraped and cleaned by using plastic cards. To avoid reflections on the surface due to evaporation of the surface, the core was taken out from the cooling room to a room with room temperature 24 hours before the images were taken. The images can be used to distinguish features and coloring in the core.

2.2.6 GEOTEK Multi Sensor Core Logger (MSCL-S)
The Geotek Multi Sensor Core Logger with spectrophotometer was used on the archive half from the core HH16-549GC to measure parameters like magnetic p-wave velocity, p-wave amplitude, wet-bulk density and coloring of the core. A photo equipment was installed on the core logger which was used to photograph the sediment core as well as retrieving information of the Munsell color system of the core.

2.2.7 Magnetic susceptibility

The magnetic susceptibility was measured by using a Bartington handheld point sensor. The magnetic susceptibility was measured every centimeter in the core. The equipment is called Magnetic Susceptibility System 2E – High- Resolution Surface Scanning Sensor Bartington. The sensor is designed to do measurements for magnetic susceptibility for soft sediment cores.

Magnetic susceptibility is described as the degree of magnetization of a material in relation to an applied magnetic field. Positive values are associated with ferromagnetic, antiferromagnetic, ferrimagnetic or paramagnetic material meaning the magnetic field is enhanced by the presence of the material. Oppositely, negative values are diamagnetic and weakened by the presence of the material. A low intensity alternating magnetic field ranging from 0,565 kHz to 2kHz is generated in an oscillator circuit in the sensor. Materials containing magnetic susceptibility will make the frequency of the oscillator change and later convert it to values of magnetic susceptibility.

Changes in glacial activity and oceanography are the main components that determine the magnetic susceptibility (Jessen, et al., 2010). The magnetic susceptibility in the North Atlantic Ocean is associated with the strength of bottom currents and in turn also the intensity of formation of deep water (Rasmussen, et al., 1996). Magnetic susceptibility in this region is likely to be dependent on grain size distribution and mineralogy (Rasmussen, et al., 1996). Higher values are linked with coarse grain sizes (63µm to 1 mm), whereas lower values are associated with finer grain sizes (clay and silt) (Rasmussen, et al., 1996).

Magnetic susceptibility is not regarded as a trustworthy tool to use in areas where methane release is large (Sztybor & Rasmussen, 2016). This is probably caused as a result of the magnetic susceptibility being disturbed due to the dissolution of magnetic minerals occurring in methane seep sediments, which is likely to be related to the formation of paramagnetic minerals and anaerobic oxidation of methane (Sztybor & Rasmussen, 2016). Palaeo-reductive environments linked with methane seepage can possibly be recognized by examining the magnetic susceptibility due to this process (Sztybor & Rasmussen, 2016).

2.2.8 Weighing room

Some samples of foraminifera were weighed in a weighing room to estimate the average weight of a foraminifera in HH16-549GC. This was done in order to calculate the satisfactory amount of foraminifera for the stable isotope analysis and radiocarbon dating. The equipment used for this purpose was Mettler Toledo XP2U Ultra Micro Balance.

2.2.9 Radiocarbon dating

Two samples of about 1100 specimens of the planktic foraminifera *Neogloboquadrina pachyderma* was collected from the core depths 258 cm and 407 cm in HH16-549GC (Table 2). The samples were sent to [14]CHRONO centre at Queens University in Belfast, United Kingdom for ^{14}C dating. The calibrated age from the radiocarbon dating was calculated by using Calib 7.1, Marine 13 (Stuiver, et al., 2016).

Table 2: Radiocarbon dating from the core HH16-549 using Neogloboquadrina pachyderma.

Depth (cm)	Material type	^{14}C age	$\pm$	$F^{14}C$	$\pm$
258	*N. pachyderma sinistral*	16085	71	0,1350	0,0012
407	*N. pachyderma sinistral*	24783	159	0,0457	0,0009

2.2.10 Mass spectrometry lab

Stable isotope analysis was carried out in the mass spectrometry lab in the geology lab at the University of Tromsø – The Arctic University of Norway. The equipment used to determine values of $\delta^{13}C$ and $\delta^{18}O$ of the foraminifera is called Thermo-Fisher MAT253 IRMS with Gasbench II. These analysis were carried out by using well preserved tests of the planktic foraminifera species *Neogloboquadrina pachyderma* (sinistral) and the benthic foraminifera species *Melonis barleeanum* and *Cassidulina neoteretis*. In total 43 samples of planktic foraminifera and 35 samples of benthic foraminifera were analyzed. Some of the samples lacked sufficient amounts of foraminifera to fulfill the requirement of 50 µg in each sample.

Foraminifera build their tests from seawater and incorporates the chemical signals from the seawater when they develop. The most used indicators are stable isotopes of carbon and oxygen (Armstrong & Braiser, 2005)

The delta value (δ) is defined as the proportion of heavier and lighter isotopes in parts per thousand (‰), which in this thesis is represented by (^{13}C/^{12}C) and (^{18}O/^{16}O).

2.2.10.1 Carbon isotope

The carbon isotopic ratio can be calculated by investigating the (^{13}C/^{12}C) ratio. To determine the value of $\delta^{13}C$, the following equation is used:

$$\delta^{13}C_{sample} = 1000 * \frac{\left(^{13C}/_{12C_{sample}}\right) - \left(^{13C}/_{12C_{standard}}\right)}{\left(^{13C}/_{12C_{standard}}\right)}$$

Carbon isotopes retrieved from benthic foraminifera are considered to be one of the best tools to reconstruct past deepwater circulation (Katz, et al., 2010). By analyzing measurements of carbon isotopes in deep-sea sediments, information of the ^{13}C content of carbon dioxide dissolved in the ocean throughout history can be recorded (Shackleton, 1987). The tests of the foraminifera are obtained by deriving $CaCO_3$ from the seawater (Armstrong & Braiser, 2005). Carbon isotopes can essentially be affected by seven different parameters: Surface water productivity, biological oxidation, upwelling and mixing, microhabitat effect, carbon burial, vital effects and diagenesis (Armstrong & Braiser, 2005). These studies are carried out by correlating the $\delta^{13}C$ values of the benthic foraminifera between several regions in the deeper part of the oceans (Katz, et al., 2010). The ^{12}C- enriched organic matter is accumulating at the ocean floor as it sinks from the surface ocean when the water masses descend and diverge (Katz, et al., 2010). Low values of $\delta^{13}C$ and higher nutrient levels occur when the organic matter oxidizes as the deepwater masses moves away from their original locality (Katz, et al., 2010). Older water masses presumably have increased nutrient levels and lower values of $\delta^{13}C_{DIC}$, whereas deepwater masses adjacent to the original locality tend to have lower nutrient levels and higher values of $\delta^{13}C_{DIC}$ (Katz, et al., 2010).

The value of $\delta^{13}C_{DIC}$ in the uppermost part of the ocean can be obtained by investigating the registered value of $\delta^{13}C$ in planktic foraminifera. This can also provide information of symbiont photosynthesis and foraminiferal respiration (Katz, et al., 2010). Carbon is supplying the atmosphere with oxygen through carbon burial and photosynthesis and is also contributing to modify the Earth's climate through time (Armstrong & Braiser, 2005). Carbon isotopes are convenient to use in order to examine palaeoproductivity of the oceans and to study the carbon cycle in a historic perspective (Armstrong & Braiser, 2005).

The content of ^{13}C in deep water masses is determined by organic carbon as well as oxidized organic matter and dissolving carbonate which provides the deep waters with carbon (Shackleton, 1987). During glacial periods, higher value of $\delta^{13}C$ is anticipated in the upper parts of the ocean. During interglacial periods, the value of $\delta^{13}C$ is likely to be low due to the fact that analysis from ice cores reveals partial pressure of atmospheric being high in interglacial periods and low in glacial periods. Changes in primary production during climatic cycles can also be revealed by changes in $\Delta\delta^{13}C$ (Armstrong & Braiser, 2005).

2.2.10.2 Oxygen isotope

The ratio of oxygen isotope (^{18}O/^{16}O) can be determined by examining the value of $CaCO_3$ in the tests of both benthic and planktic foraminifera (Katz, et al., 2010). The value of $\delta^{18}O$ is calculated by the following equation:

$$\delta^{18}O_{sample} = 1000 * \frac{\left(^{18}O/_{16}O_{sample}\right) - \left(^{18}O/_{16}O_{standard}\right)}{\left(^{18}O/_{16}O_{standard}\right)}$$

Investigating oxygen isotopes is considered a useful tool to reconstruct past paleoceanographic settings as an indicator of sea-level, volume of ice and paleothermometer (Katz, et al., 2010). The proportion of stable isotopes [18]O and [16]O in tests containing $CaCO_3$ can be influenced by primarily five different factors, which is temperature, isotopic composition of the water, diagenesis, mineral phase and vital effects (Armstrong & Braiser, 2005). Oxygen isotopes are useful to determine changes in ice volume and past temperature and salinity conditions (Armstrong & Braiser, 2005).

2.3 Microscopy

The microscopy work in this thesis was performed in the micropaleontology laboratory at the University of Tromsø – The Arctic University of Norway. Studying microfossils provide information about various environmental parameters giving valuable knowledge to reconstruct paleo-environmental conditions. In this thesis, foraminifera is studied to reconstruct past environmental conditions by examining faunal assemblages, radiocarbon dating and stable isotope analysis.

The microscope used for this purpose was Leica CLS150X-MZ12s. The fraction from 100-500µm was used to investigate foraminifera for HH16-549GC. The samples were evenly distributed on a tray to get more reliable results for picking foraminifera. Another tray was placed underneath the picking tray to collect the foraminifera for further analyzes. If a sample contained too much sediments, a sample splitter was used to obtain smaller portions on the tray. To get a good statistical result, 300 foraminifera were picked for each sample. In this thesis, the foraminifera was only distinguished by planktic or benthic species.

2.3.1 Foraminifera

Foraminifera single-celled organism that lives with marine plankton or on the sea bottom (Armstrong & Braiser, 2005). The cytoplasm of the cell of the foraminifera is placed within a shell or a test. The test can consist of organic matter, calcareous material or agglutinated particles, and can have either single or multiple chambers connected by one or several openings (Armstrong & Braiser, 2005). Foraminifera are easy to study, has a great variety of species and are abundant which makes them important biostratigraphical indicators in marine sediments, especially in Cenozoic, Mesozoic and Late Palaeozoic age (Armstrong & Braiser, 2005).

Foraminifera lives in a wide variety of conditions ranging for polar to tropical regions, and in the upper water column to the deep sea which makes them a very suitable tool to investigate both recent and past environmental conditions (Armstrong & Braiser, 2005). It is useful to investigate the composition of the assemblages of foraminifera to track the depth of seawater and circulation of water masses (Armstrong & Braiser, 2005) Foraminiferal tests with $CaCO_3$ can be used to study changes in ocean chemistry and temperature when investigating stable isotopes of the tests (Armstrong & Braiser, 2005). The shells can be used to calculate absolute age by radiocarbon dating of ^{14}C (Schiebel & Hemleben, 2005).

2.3.2 Planktic foraminifera

Planktic foraminifera are marine organisms with single cells, chambered tests and calcareous shells (Schiebel & Hemleben, 2005). They first appeared in the mid-Jurassic period and has been spread across the oceans of the world since mid-Cretaceous (Schiebel & Hemleben, 2005). The distribution of planktic foraminifera is mainly controlled by temperature, availability of food and chemistry of the surrounding ocean water (Schiebel & Hemleben, 2005). Studying planktic foraminifera has been important in order to investigate stratigraphy, paleoceanography and ecology (Schiebel & Hemleben, 2005).

Planktic foraminifera generally does not record negative values of $\delta^{13}C$ obtained from methane in their tests because almost all methane discharged from the seafloor is absorbed by methanotrophic aerobic microbes in the water column (Niemann, et al., 2006; Reeburgh, 2007). The coiling mode of the planktic foraminifera is useful to study in order to reconstruct past marine environments and how they are connected to environmental parameters (Darling, et al., 2006).

2.3.2.1 Neogloboquadrina pachyderma sinistral

The dominating planktic foraminifera in HH16-549GC is *Neogloboquadrina pachyderma sinistral*, which are superior in higher polar latitudes (Darling, et al., 2004). *N. pachyderma* is the prevailing assemblage of foraminifera in Arctic waters (Moller, et al., 2013) and is considered to be the only planktic foraminifera that reveals glacial conditions and polar surface water (Bauch, et al., 2001). *N. pachyderma sinistral* is assumed to comprise over 90% of the marine surface sediment assemblage in the Norwegian, Iceland and Greenland Sea (Pflaumann, et al., 1996). Changes in the abundance of *N. pachyderma sinistral* have been linked with time periods with swift climatic changes in the North Atlantic region. An example of such an event is the Younger Dryas (Kohfeld & Fairbanks, 1996). It is regarded as a useful geochemical and ecological proxy to reconstruct salinity, sea ice, temperature and nutrient conditions in past polar ocean in polar latitudes (Kohfeld & Fairbanks, 1996; Darling, et al., 2004).

N. pachyderma dextral inhabits the warmer subpolar regions, whereas *N. pachyderma sinistral* is located in the colder polar water. Comparing these two species is useful to indicate changing climate as the fluctuation between the two coiling forms is understood to occur as a result of varying climate conditions throughout time (Kucera & Kennett, 2002). The exchange of subpolar surface water from the Atlantic Ocean is assumed to have less influence in the core areas as *N. pachyderma sinistral* is the predominant species in HH16-549GC (Jansen, et al., 1983).

2.3.3 Benthic foraminifera

Benthic foraminifera of smaller size are the most prevailing and commonly used for regional stratigraphy (Armstrong & Braiser, 2005). Their tests are usually well preserved, which is part of the reason why they are very useful indicators of past environment as they can be found in the marine sediments from the deepest trenches in the sea to extreme tidal marshes (Armstrong & Braiser, 2005). In marine environments, benthic foraminifera are widespread and are found at various locations (Rasmussen & Thomsen, 2014).

They can be used to investigate environmental parameters like water temperature, salinity, food supply, bottom currents, oxygen level, pollution and as an indication of the distribution of sea ice (Rasmussen & Thomsen, 2014). The $\delta^{13}C$ of benthic foraminifera may record significantly depleting values in areas with higher intensity of marine seepage. (Wefer, et al., 1994; Rathburn, et al., 2003; Hill, et al., 2004).

2.3.3.1 Cassidulina neoteretis

The most dominating benthic species in the core HH16-549GC is *Cassidulina neoteretis*. It was used as a proxy in this study for all the samples for stable isotope dating apart from the three uppermost samples (0-67 cm). *Cassidulina neoteretis* is described as an infaunal species which thrives in cold bottom water temperatures in fine-grained, organic-rich and terrigenous mud (Seidenkrantz, 1995). It is the most abundant living benthic foraminifera in regions with cold bottom water with low salinity and is characteristically present in several different cold glaciomarine environments (Mackensen & Hald, 1988). The distribution pattern of *Cassidulina neoteretis* typically follows specific water masses and can be used as an indicator of cold water masses in the regions of the Norwegian Shelf and the northern North Atlantic (Seidenkrantz, 1995), which has caused the species to retreat to colder areas in the western Barents Sea in the last 7,800 years BP (Mackensen & Hald, 1988). It is commonly found on northern continental slopes and shelves and is related to cold polar deep water in Arctic regions, and is also known to thrive in lower middle slopes of the Norwegian Sea with cold-water conditions (Mackensen & Hald, 1988) in both deep water and shallower parts of the ocean (Seidenkrantz, 1995). It inhabits boreal and arctic regions at water depths ranging from 150 to 3000 meters, but is most prevailing at water depths from 1000 to 1500 meters (Seidenkrantz, 1995).

Cassidulina neoteretis is regarded as the younger and evolutionary offspring of the elder type *Cassidulina teretis*, which possibly was extinct 0,7 Ma BP (Seidenkrantz, 1995). The evolution of the species probably occurred between 2,0 – 2,3 Ma in the North Atlantic Ocean before it migrated towards the Norwegian Sea and displaced *Cassidulina teretis* (Seidenkrantz, 1995). *Cassidulina neoteretis* is considered to be smaller and have a narrower ecological range than *Cassidulina teretis* (Seidenkrantz, 1995). The notch on the marginal end of *Cassidulina neoteretis* is described be shaped like a triangle with an extensive and smooth apertural plate (Lazar, et al., 2016). There is generally an increasing abundance of *Cassidulina neoteretis* throughout the last deglaciation and a reduction in the cold Younger Dryas period (Spielhagen, et al., 2011).

2.3.3.2 Melonis barleeanum

The benthic foraminifera *Melonis barleeanum* was used for stable isotope analysis in HH16-549GC in three uppermost samples (0-67 cm). *Melonis barleeanum* was used as a proxy as the abundance of *Cassidulina neoteretis* was lacking in the three uppermost samples, which made them unable to satisfy the requirement of 50 μg of foraminifera in each sample for stable isotope analysis.

Melonis barleeanum is occurring both in remaining deposits from the last glacial period and in present-day sediments (Caralp, 1989). It is characterized as an infaunal species that eats organic matter buried in muddy, basinal sediments which thrive in relatively degraded organic matter coming from redeposition in shallow areas (Jennings, et al., 2004). A higher concentration of Melonis barleeanum might be caused as a result of a transition from fresh organic matter to degraded organic matter (Slubowska, et al., 2005). The quality of the organic matter is likely to affect the distribution of *Melonis barleeanum* (Caralp, 1989). Assemblages of *Melonis barleeanum* is closely linked with plentiful, little-altered, marine organic matter, which is favorable conditions in upwelling zones (Caralp, 1989) and is regarded to be a flexible species in terms of fluctuating environmental conditions and availability of food (Linke & Lutze, 1993). Increasing amounts of *Melonis barleeanum* can be an indication of glacial climate and a general cooling trend worldwide (Caralp, 1989) and is suggested to imply escalating influx of cold Atlantic water into the Arctic Ocean as well as higher bottom water temperatures and increasing salinity (Slubowska, et al., 2005).

3 Results

The sediment core HH16-549GC was retrieved from inside a pockmark from Vestnesa Ridge, Svalbard. Colour images have been taken of this core using the XRF core scanner (Figure 18), while X-ray photographs have been taken using GEOTEK X-Ray photography (MSCL-XCT) (Figure 19). The lithological log along with Munsell values is presented in figure 20. The Munsell values from this core have been studied by using the XRF core scanner, these values have also been visually determined to validate the values. The density has been measured by using the GEOTEK Multi Sensor Core Logger (MSCL-S) (Figure 21). The magnetic susceptibility was measured using a Bartington handheld point sensor recording values for every centimeter in the core (Figure 21). Figure 22 illustrates the percentage of all grain sizes in the fractions ranging from 63-100 µm, 100-500 µm, 500-1000 µm and IRD >1 mm. Stable isotope analysis of foraminifera is presented in figure 23, while Leco CS-744-data along with the concentration of both planktic and benthic foraminifera are displayed in figure 24. The flux of foraminifera has not been calculated in this thesis due to uncertainties of the water content because of pore water samples that were taken out for analysis.

Analysis of pore water data is presented in figure 25. The analysis was performed at the Geological Survey of Denmark and Greenland (GEUS) in Copenhagen, Denmark. The lower parts of the core have been reported to be smelly when it was retrieved. The core has been divided into six different units based on distinctive features particularly interesting in HH16-549GC and will be described further in chapter 3.1 to 3.6.
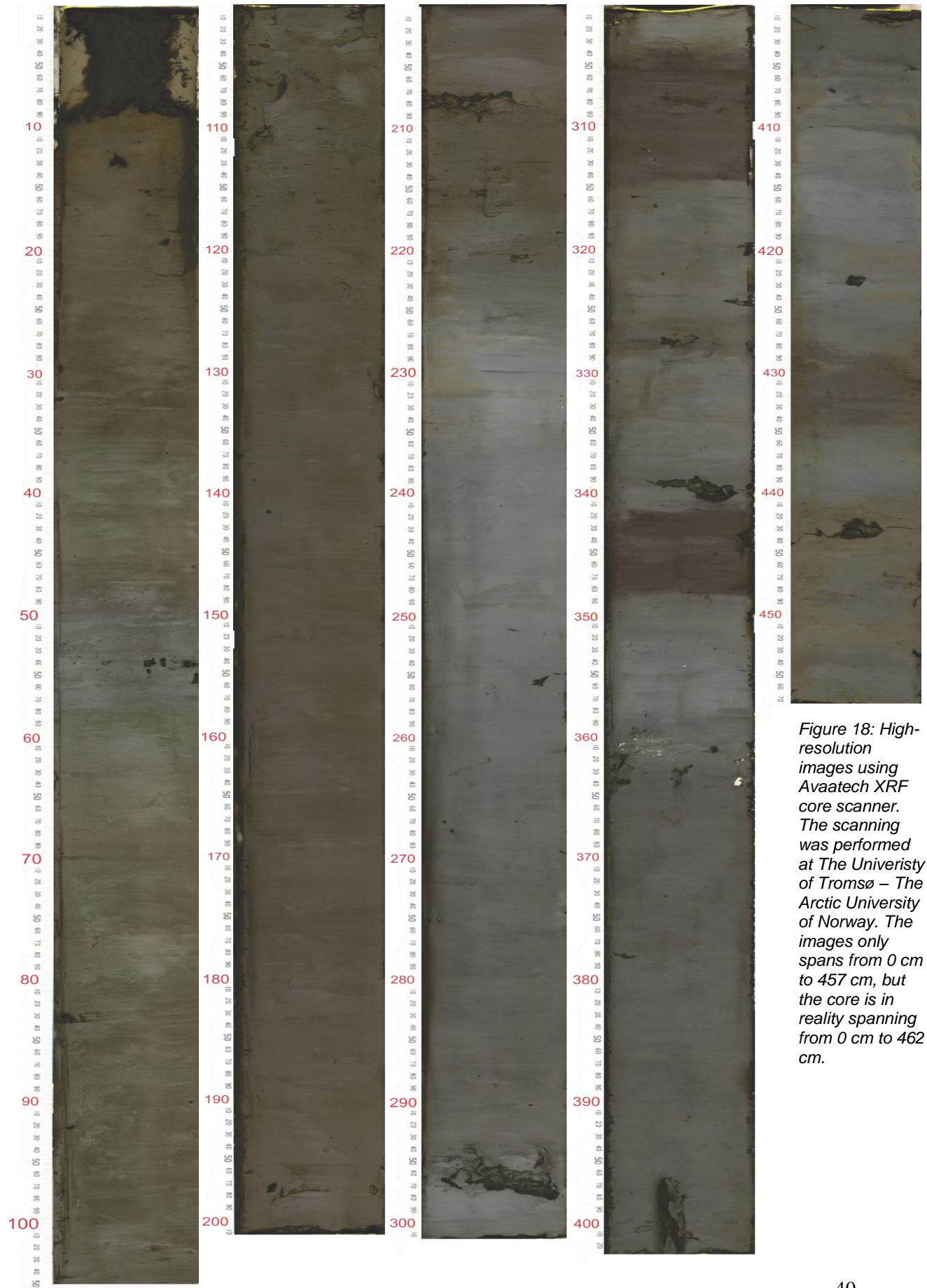
Figure 18: High-resolution images using Avaatech XRF core scanner. The scanning was performed at The Univeristy of Tromsø – The Arctic University of Norway. The images only spans from 0 cm to 457 cm, but the core is in reality spanning from 0 cm to 462 cm.

40
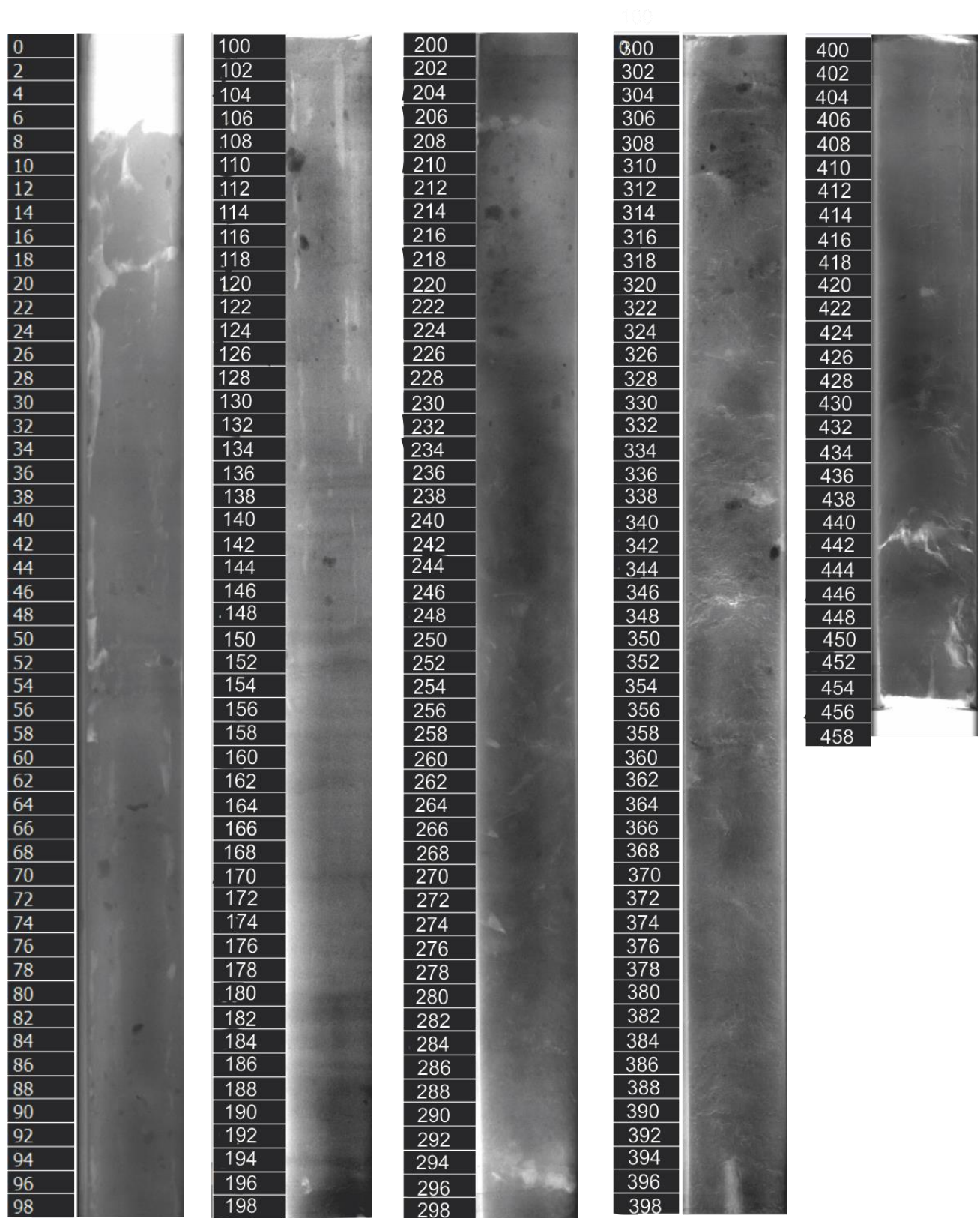
Figure 19: X-ray image of the sediment core HH16-549GC using Geotek X-ray core imaging system.
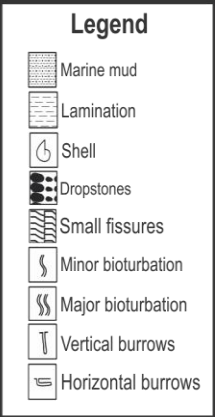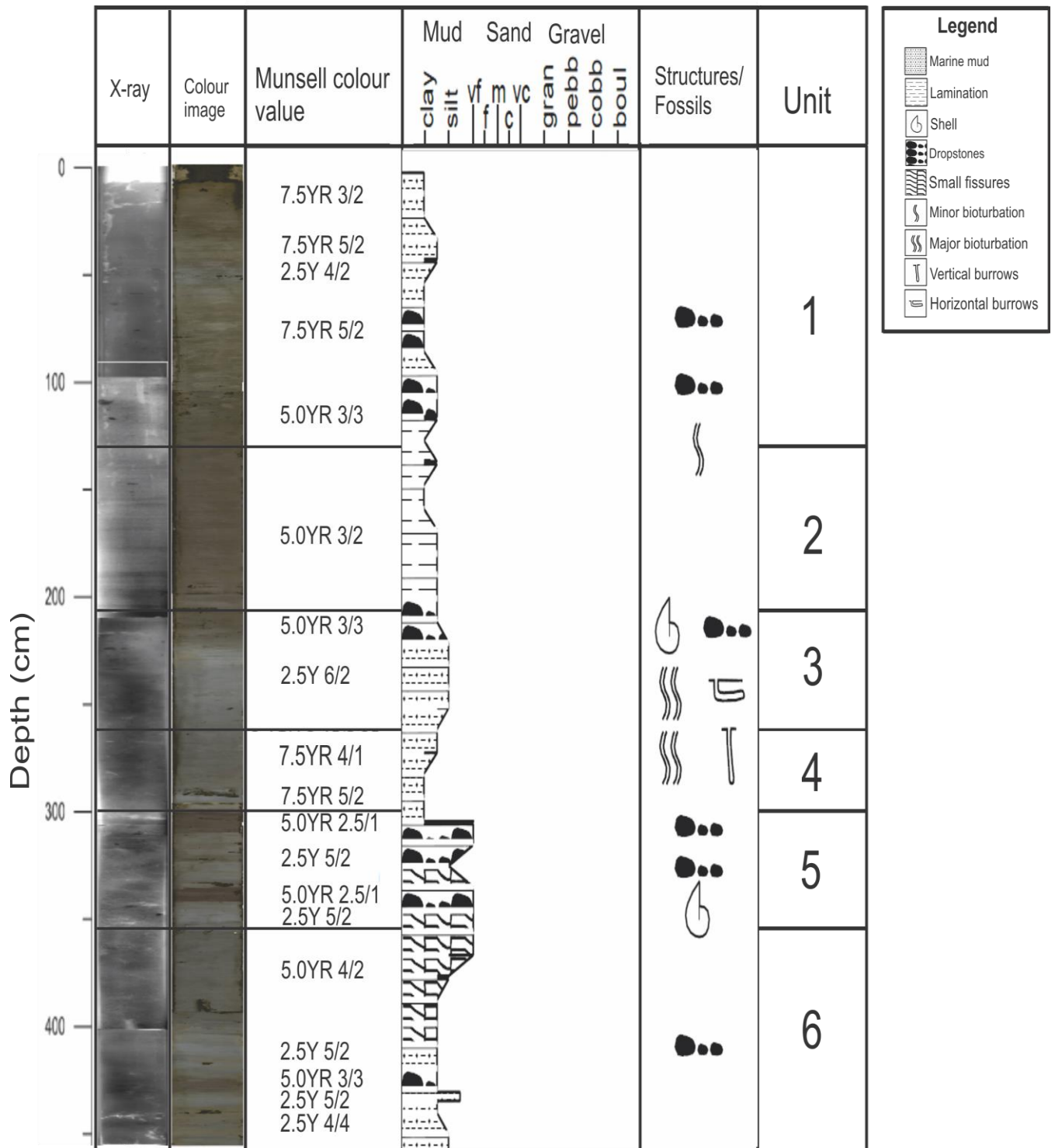
Figure 20: Comparison of the lithological log, x-ray and colour image. The core is divided into six different units which will be described in section 4.1 to 4.6.
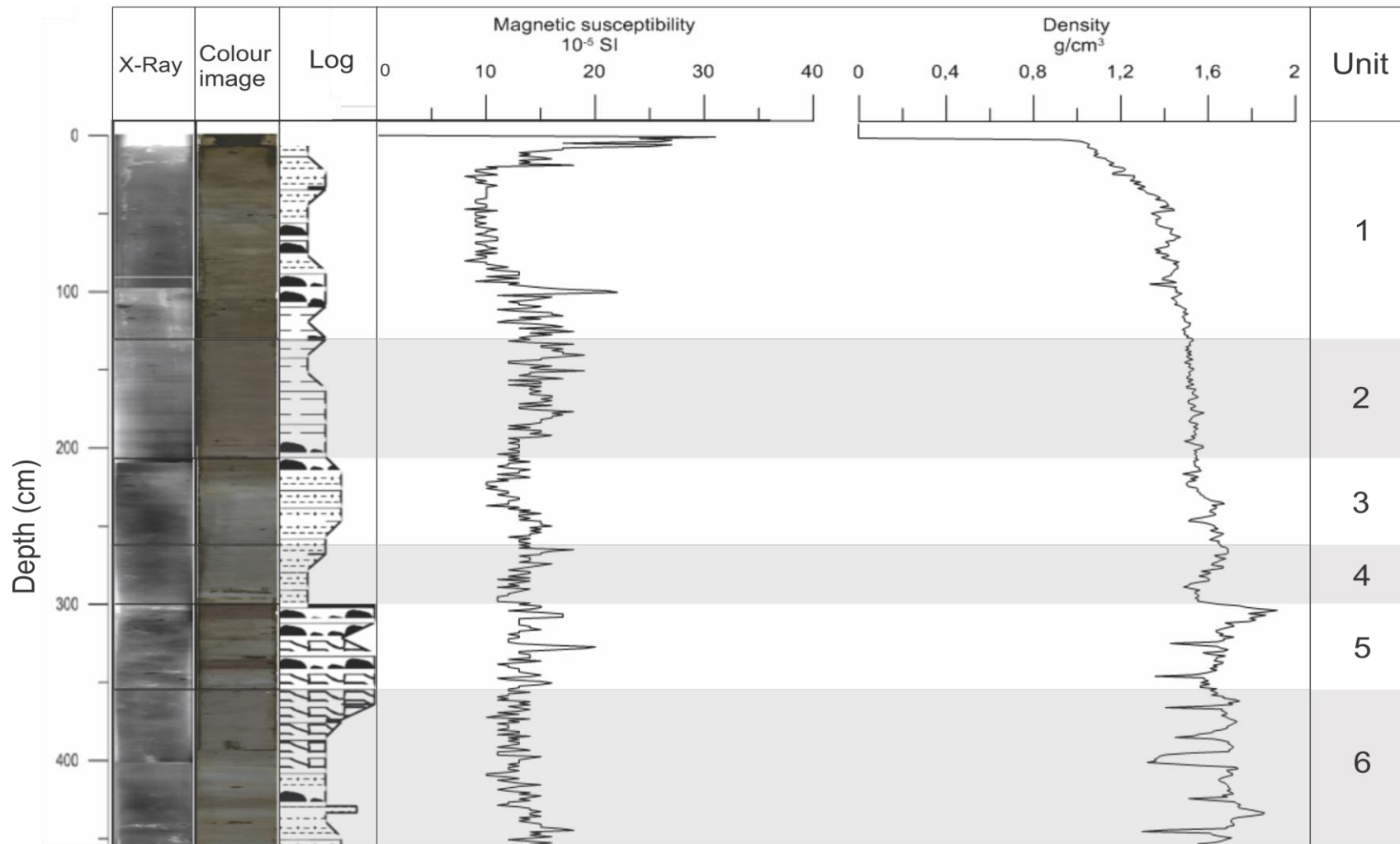
Figure 21: Illustration of x-ray,- and colour image in comparison to the lithological log, magnetic susceptibility and density of HH16-549GC..
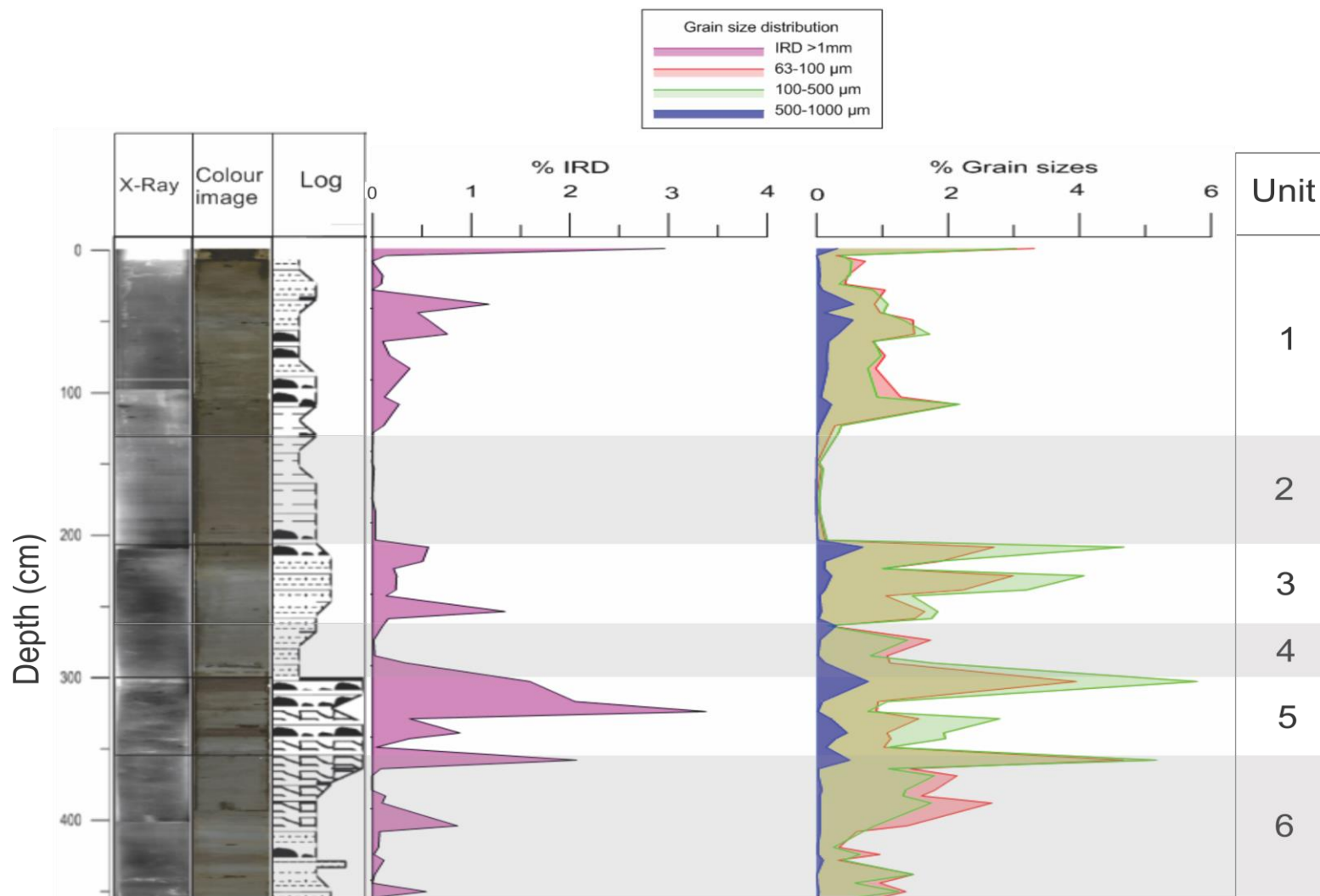
Figure 22: Illustration of x-ray,- and colour image in comparison to the lithological log and percentage of all the different fractions.
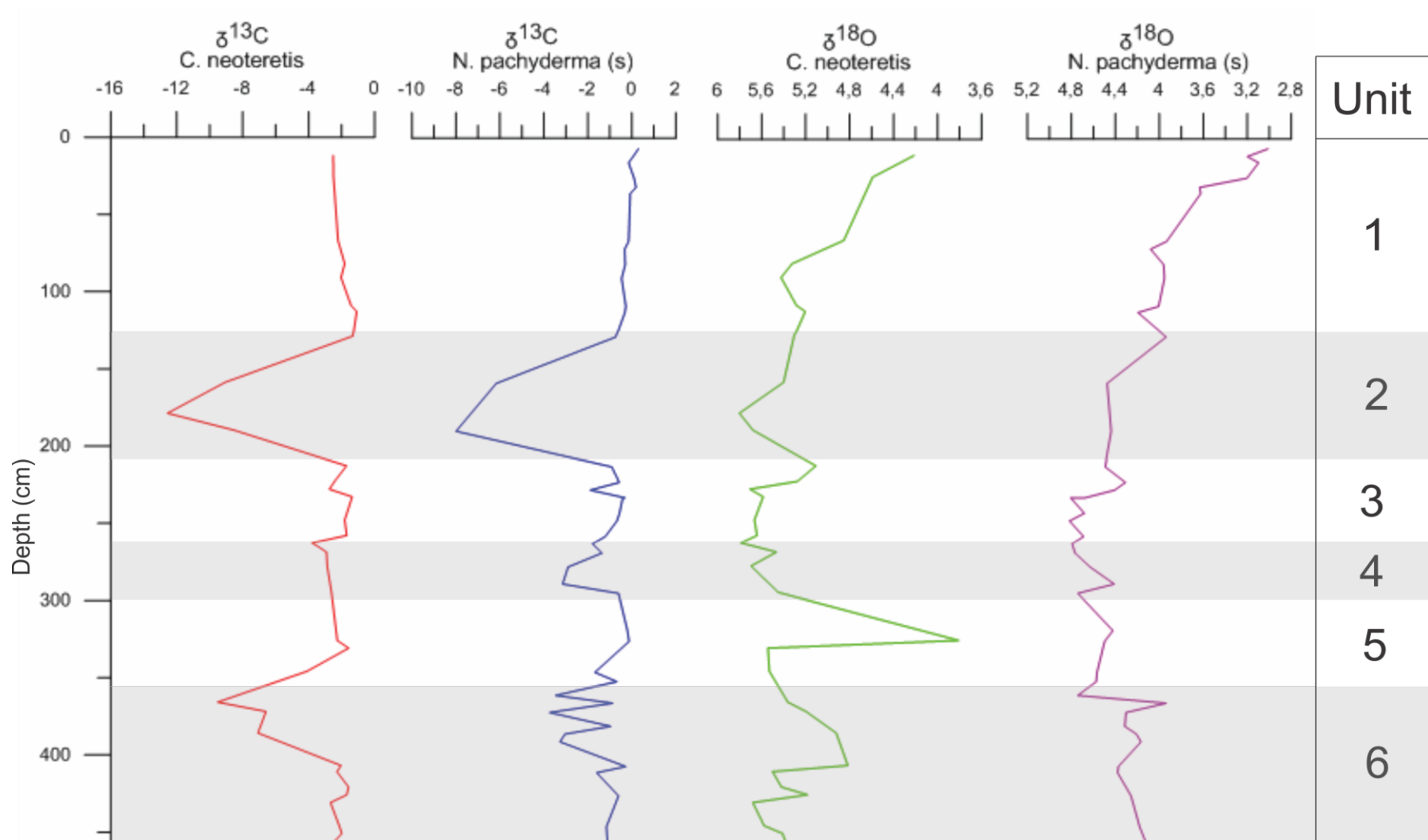
Figure 23: Stable isotope analyses in HH16-549GC for $\delta^{13}C$ using the benthic foraminifera C. neoteretis and $\delta^{18}O$ using N. pachyderma sinistral.
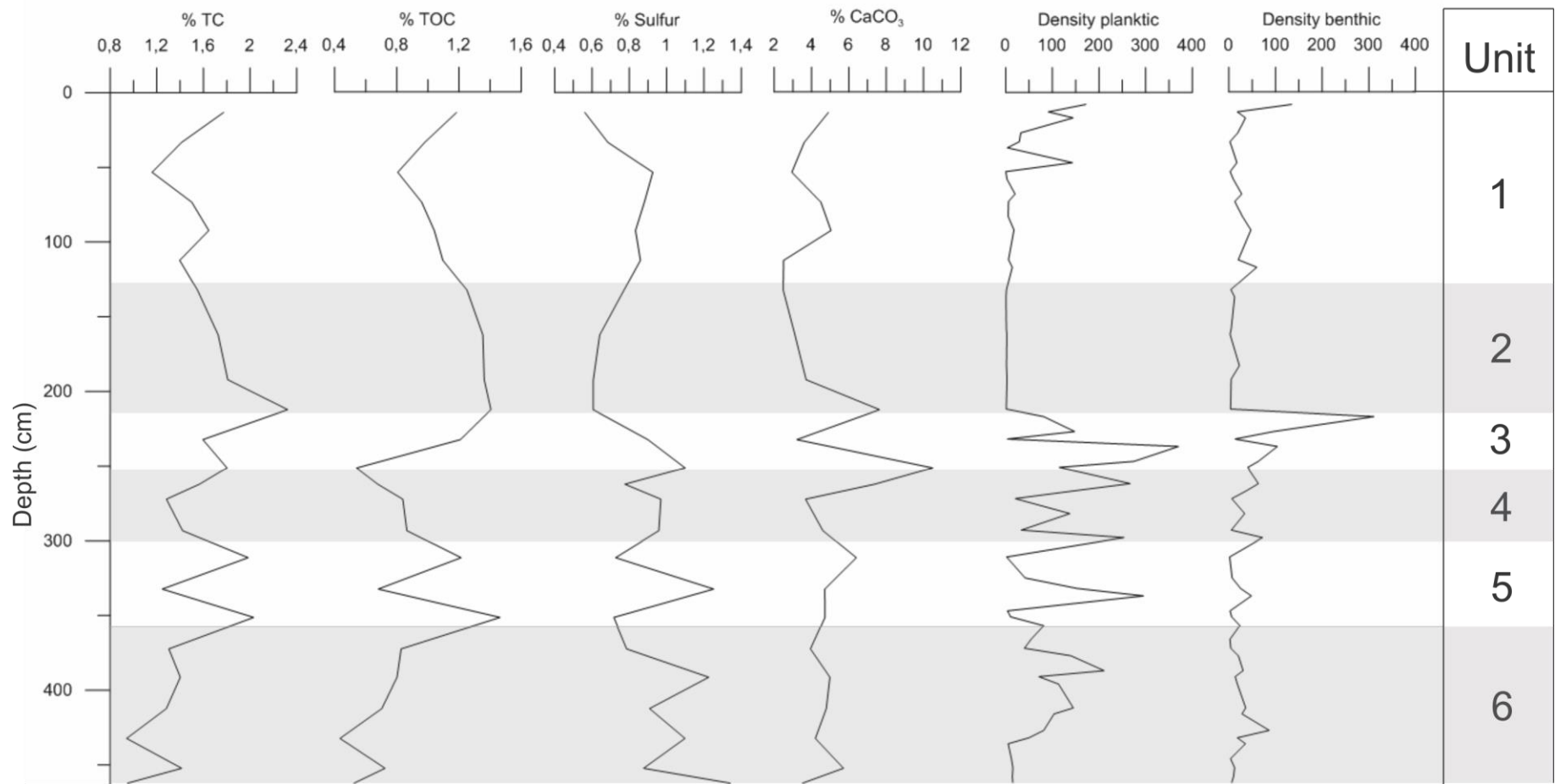
Figure 24: Values from total carbon (TC), total organic carbon (TOC), sulfur, calcium carbonate ($CaCO_3$) and the concentration of planktic and benthic foraminfera.

The analysis of pore water data from HH16-549GC is presented in figure 25. The analysis was performed at the Geological Survey of Denmark and Greenland (GEUS) in Copenhagen, Denmark.
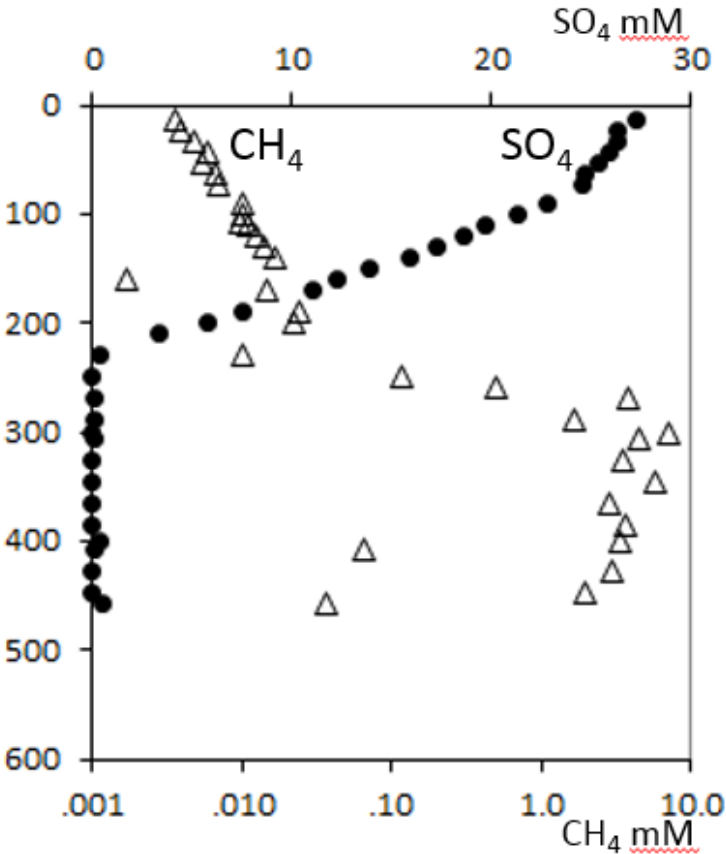
Pore water core HH16-549GC

Figure 25: Pore water data from core HH16-549GC. The sulfate-methane transition zone is located at approximately 185 meters in the core. The pore water data is provided by Troels Laier from the Geological Survey of Denmark and Greenland (GEUS) Copenhagen, Denmark.

Table 3 displays the two radiocarbon datings for the HH16-549GC core.

Table 3: Uncalibrated age of 14_C and the calibrated age using Calib 7.1, Marine 13.

Core	Depth (cm)	Species	14_C age	Cal. Yr BP 2σ range	Cal. Yr BP 2σ mean
HH16-549GC	258	*N. pachyderma sinistral*	16,085±71	19,110-18,764	18,914
HH16-549GC	407	*N. pachyderma sinistral*	24,783±159	28,757-28,013	28,439

3.1 Unit 1 (0-130 cm)

The first 10 cm of the core did not contain any sediments (Figure 18). Thin layers of lamination have been detected from 120 cm to 130 cm (Figure 19). The sediments mainly consist of marine mud with dropstones located from 70 cm to 80 cm and from 110 cm to 120 cm (Figure 20). The coloring at the upper part of the core is dark brown (7.5YR 3/2). Further down it changes to the slightly lighter brown (7.5YR 5/2). At around 50 cm in the core, a small section changes to dark grayish brown (2.5Y 4/2) before it returns to brown (7.5YR 5/2) again. Towards the end of the unit, the colour gets darker to dark reddish brown (5.0YR 3/3) (Figure 20).

The first 16 cm records the highest value of magnetic susceptibility in the whole core with the highest value at 10 cm being 31 ($10^{-5}SI$) (Figure 21). Following the high peak there is a gradual decrease of magnetic susceptibility down to 29 cm (10 ($10^{-5}SI$)) before it reaches a steady value at 102 cm. From 102 cm to 130 cm the magnetic susceptibility shows a gradual increase with a large peak at 109 cm (22 ($10^{-5}SI$)). The density reveals increasing values throughout the section ranging from 1 g/cm^3 to 1,5 g/cm^3 (Figure 21). The grain size in this section is moderately fluctuating through the section (Figure 22). In the upper 50 cm all grain sizes >63 µm are low. From 50 cm to 130 cm the fractions of 63-100 µm and 100-500 µm are relatively high in comparison to the other fractions. The concentration of ice-rafted debris is relatively high from 30 cm to 130 cm.

Both benthic and planktic $\delta^{13}C$ show high values throughout the section, while benthic and planktic $\delta^{18}O$ both have an increasing trend from the start of the unit to the end (Figure 23). The concentration of benthic foraminifera is relatively low in this section with peaks at 92 cm and 117 cm (Figure 24). Distribution of planktic foraminifera shows greater variation in the first 50 cm with large peaks at 8 cm, 17 cm and 47 cm. From 50 cm to 130 cm there is generally a low abundance of planktic foraminifera. Percentage of total carbon and calcium carbonate shows similar trends in this section with high peaks at 13 cm (1,77% and 4,91% respectively) and 92 cm (1,65% and 5,05%) and with low peaks at 53 cm (1,16% and 2,95%) and 112 cm (1,40% and 5,05%) (Figure 24). Total organic carbon starts off with relatively high value (1,18%) decreasing until 53 cm (0,81%) before it gradually increases towards the end of the section. Percentage of sulfur for total carbon has relatively low values at 13 cm and 130 cm with a high peak at 53 cm (0,93%).

3.2 Unit 2 (130-215 cm)

Both X-ray photographs and colour images show clear indications of lamination from 135 cm until 215 cm in this section (Figure 18 and 19). A small abundance of dropstones is located towards the end at approximately 205 cm to 215 cm (Figure 20). The coloring in this section is more or less monotone being dark reddish brown (5.0YR 3/2) throughout the section (Figure 20). The magnetic susceptibility fluctuates between (12 ($10^{-5}SI$)) and (19 ($10^{-5}SI$)) with a marginally decreasing trend throughout the section (Figure 21). The density has a slight increasing trend in this unit. The grain size >63 μm are at its minimum throughout the whole core with values close to zero (Figure 22).

Planktic and benthic $\delta^{13}C$ have largely negative values located at around 185 cm in the core. Benthic $\delta^{18}O$ shows high value at 185 cm, while planktic $\delta^{18}O$ generally has an increasing trend throughout the section (Figure 23). This section records the lowest concentration of planktic foraminifera during the whole sediment core with roughly any specimens (Figure 24). The same applies for benthic foraminifera, except there are a slightly higher concentration of these specimens at 183 cm. Percentage of carbon and calcium carbonate has a gradual increase in this section with a high peak at 212 cm (2,32% and 7,65%) (Figure 25).

Total organic has a slightly increasing trend through the whole unit, while sulfur has an opposite steady decrease in the same zone. The sulfate-methane transition zone is located at approximately 185 cm in the core (Figure 25).

3.3 Unit 3 (215-262 cm)

A small layer of bivalve shells is found in this section from 235 cm to 240 cm (Figure 18). Dropstones are observed from 215 cm to 225 cm (Figure 19), while the remaining part consists of marine mud (Figure 20). The coloring at the top of the unit is similar to the section above, characterized as dark reddish brown (5.0YR 3/3) (Figure 20). From 225 cm to 262 cm the coloring changes to light brownish gray (2.5YR 6/2). Moderate bioturbation and horizontal burrows occur towards the end of this unit. (Figure 20).

The magnetic susceptibility shows a slightly increasing trend with values oscillating from (10 $(10^{-5}SI)$) to (16 $(10^{-5}SI)$) in this section (Figure 21). The density generally increases through this unit with relatively small fluctuations. The distribution of grain sizes shows greater variations in comparison to the previous section (Figure 22). The fractions ranging from 63-100 µm and 100-500 µm shows high peaks at 217 cm, 237 cm and 262 cm. The fraction from 500-1000 µg has relatively low values in this section, but has a peak at 217 cm. IRD >1 mm records moderate values with a large peak at 262 cm.

Benthic and planktic $\delta^{13}C$ both have fairly stable high values with small fluctuations (Figure 23), while planktic and benthic $\delta^{18}O$ has low values at the start of the section before it increases for the rest of the unit. Large assemblages of planktic foraminifera are recorded in this section with high peaks at 227 cm, 237 cm and 262 cm (Figure 24). The highest peak of benthic foraminifera in throughout the core is found at 217 cm in the core. There is also a small peak at 237 cm. The concentration of total carbon has a generally decreasing trend in this section with a low peak at 232 cm (1,60%) and a high peak at 251 cm (1,80%) (Figure 24). Percentage of total organic carbon also has a rapid decreasing trend recording its lowest peak throughout the core at 251 cm (0,54%). The content of calcium carbonate fluctuates greatly and has a low peak at 232 cm (3,22%) and a high peak at 251 cm (10,51%). Percentage of sulfur has an increasing trend with a high peak located at 251 cm (1,10%).

3.4 Unit 4 (262-300 cm)

A large hole in the sediments is observed at 296 cm in the core (Figure 18), which is revealed as a white layer in the X-ray photograph (Figure 19). Similar to unit 3, this section also contains moderate bioturbation and vertical burrows (Figure 20). From 262 cm to 290 cm the coloring is dark gray (7.5YR 4/1) before it changes to brown (7.5YR 5/2) in the last 10 cm of the unit (Figure 20).

The magnetic susceptibility has slightly decreasing values in this unit with fluctuating values from $(11 \ (10^{-5}SI))$ to $(18 \ (10^{-5}SI))$ with the highest peak located at 273 cm (Figure 21). The density has relatively high values at the start of the section, but decreases rapidly towards the end of the unit. The abundance of IRD >1 mm is relatively low in the start of the unit but increases rapidly towards the end of the unit. The grain sizes ranging from 63-100 µm, 100-500 µm and 500-1000 µm fluctuates greatly with increasing values approaching the end of the section.

The values of benthic $\delta^{13}C$ has a drop at the start of the unit before it increases slightly (Figure 23). Planktic $\delta^{13}C$ has a negative excursion located at around 285 cm. Both benthic and planktic $\delta^{18}O$ decreases throughout the section. The concentration of benthic foraminifera is generally low in this section with high peaks occurring at 262 cm and 298 cm (Figure 24). The assemblage of planktic foraminifera is however large, with peaks located at 282 cm and 298 cm. Percentage of total carbon and calcium carbonate reveals similar trends with high values in the start and the end of this unit with a low peak occurring at 272 cm (1,28% and 3,71% respectively) (Figure 24). The content of sulfur has the opposite trend with low values at the start and the end of the unit and a high peak occurring at 272 cm (0,97%). The concentration of total organic carbon is in a transition zone with a gradually increasing trend with low peak occurring in unit 3 and high peak at the start of unit 5.

3.5 Unit 5 (300-357 cm)

Figure 18 reveals two remarkably dark areas centered at 310 cm and 345 cm with a small hole at 340 cm. Layers with small fissures are dominating this disturbing the lithology (Figure 19). Dropstones are observed at around 305 cm and 343 cm (Figure 19). The coloring gets remarkably darker from 300 cm to 310 cm and 338 cm to 343 cm the coloring and is classified as dark reddish brown (5.0YR 2.5/1) (Figure 20). The coloring gets lighter between 310 cm to 338 cm and 343 cm to 357 cm, labeled as grayish brown (2.5Y 5/2).

The magnetic susceptibility reveals large variations ranging from (11 ($10^{-5}SI$)) to (20 ($10^{-5}SI$)) (Figure 21). The density has its highest values throughout the core in the start of the section (307 cm) before it reduces rapidly toward the end of the unit. The grain sizes fluctuates greatly in this section (Figure 22). The fractions from 63-100 µm 100-500 µm and 500-1000 µm records high peaks at 311 cm and 351 cm in this unit. IRD >1 mm records its highest peak throughout the core at 311 cm before it declines significantly towards the end of the unit.

Both planktic and benthic $\delta^{13}C$ have fairly steady values up to 325 cm before it decreases significantly towards the end of the unit (Figure 23). Benthic $\delta^{18}O$ shows a large negative excursion at 325 cm (3,81‰), while planktic $\delta^{18}O$ remains fairly stable in the section. The assemblage of planktic foraminifera in this unit decreases rapidly up to 311 cm (Figure 24), before it increases significantly to 337 cm. From 337 cm to 357 cm the concentration of planktic foraminifera decreases considerably again. The concentration of benthic foraminifera generally shows the same trend but in a remarkably lower magnitude. The concentration of total carbon and total organic carbon displays the exact same trends in this unit with high peaks at 311 cm and 351 cm and a low peak at 332 cm (Figure 24). The percentage of sulfur reveals a completely opposite trend with low peaks at 311 cm and 351 cm and a high peak at 332 cm. Calcium carbonate has a slightly decreasing trend throughout the unit.

3.6 Unit 6 (357-462 cm)

A large assemblage of bivalve shells centered at 363 cm in this unit (Figure 18). Cracks in the sediments are observed at 398 cm, 422 cm and 443 cm (Figure 18) and are revealed by white spots in the x-ray photography (Figure 19). The lithology is dominated by small fissures from 357 cm to 400 cm, similar to observations in unit 5 (Figure 20). The coloring in the first section from 357 cm to 400 cm the coloring is classified as dark reddish brown (5.0YR 4/2) (Figure 20). Lighter coloring labeled as grayish brown (2.5Y 5/2) occurs from 400 cm to 425 cm and 430 cm to 435 cm. A noticeable darker layer observed from 425 to 430 cm is classified as dark reddish brown (5.0YR 3/3). Towards the end of the unit the coloring changes to olive brown (2.5Y 4/4).

The magnetic susceptibility increases slightly in this section with fluctuating values ranging from (10 ($10^{-5}SI$)) to (18 ($10^{-5}SI$)) (Figure 21). The density shows significantly fluctuating values throughout the unit. All grain sizes have a large peak situated at 366 cm before they all record a steep decrease towards 377 cm (Figure 22). The grain size from 500-1000 µm remains low from 377 cm to 462 cm. The fractions ranging from 63-100 µm, 100-500 µm has relatively high and fluctuating values towards the end of the unit. IRD >1 mm remains low with high peaks at 400 cm and 455 cm.

Benthic $\delta^{13}C$ reveals negative values at the start of the unit (-9.60‰) before it gradually increases towards the end (Figure 23). Planktic $\delta^{13}C$ shows great fluctuations. Benthic $\delta^{18}O$ has gradually decreasing trend towards around 410 cm, before it increases towards the end of the section. Planktic $\delta^{18}O$ records a rapid decrease at the start of the unit and becomes fairly stable towards the end.

The concentration of benthic foraminifera has relatively low but slightly fluctuating assemblage except for a peak at 427 cm (Figure 24). The concentration of planktic foraminifera records a greater abundance with peaks located at 387 cm and 412 cm before it gradually decreases towards the end of the core. The concentration of total carbon and total organic carbon displays a similar decreasing trend with low peaks at 432 cm and 462 cm, and high peak at 452 cm (Figure 24). The content of sulfur is highly fluctuating with generally increasing trend toward the end of the unit. The value of calcium carbonate is fairly low with small fluctuations.

4 Correlation and age model establishment

In a study from Jessen et al (2010), eleven sediment cores from 76° to 80° located west of Svalbard were investigated. The sediment cores were retrieved in water depths ranging from 630 meters to 1880 meters. Figure 26 illustrates the position of the cores investigated the study.
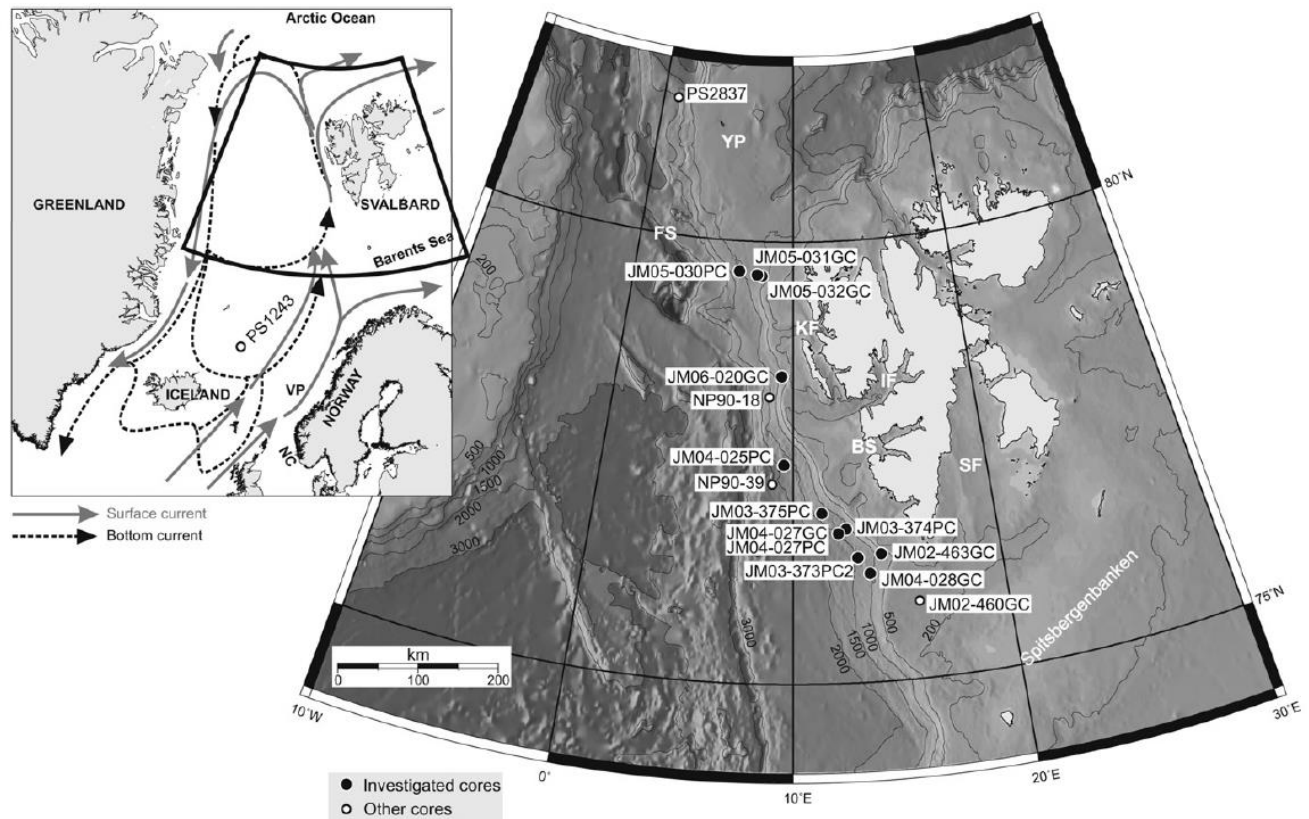
Figure 26: Map of the location of the cores investigated for the stacked magnetic susceptibility by (Jessen, et al., 2010). The arrows illustrate both surface and bottom currents. Fram Strait (FS), Yermak Plateau (YP), Bellsund (BS), Isfjorden (IF), Storfjorden (SF), Norwegian Channel (NC) and Vøring Plateau (VP) is indicated on the figure.

The stratigraphy, lithology and magnetic susceptibility in HH16-549GC is correlated with the study from Jessen et al (2010). Figure 18 and 19 reveals two distinctive events that are particularly interesting to correlate with the study from Jessen et al (2010). The first one is a distinctive laminated layer with fine-grained sediments between tie-point 5 and 6, suggested to occur at 14,600 cal years BP and 15,070 BP, respectively. This feature is interpreted to occur from 134 cm to 200 cm in HH16-549GC (Figure 19).

The second feature is associated with dark, coarse-grained deposits interpreted to be related to glacigenic mass transport deposits aged from 23,770 cal years BP to 24,240 cal years BP. The same event is understood to occur from around 305 cm to 315 cm in HH16-549GC (Figure 18). These are both valuable events to consider in order to construct an age model for the HH16-549GC core. Figure 27 illustrates the stacked magnetic susceptibility in Western Svalbard
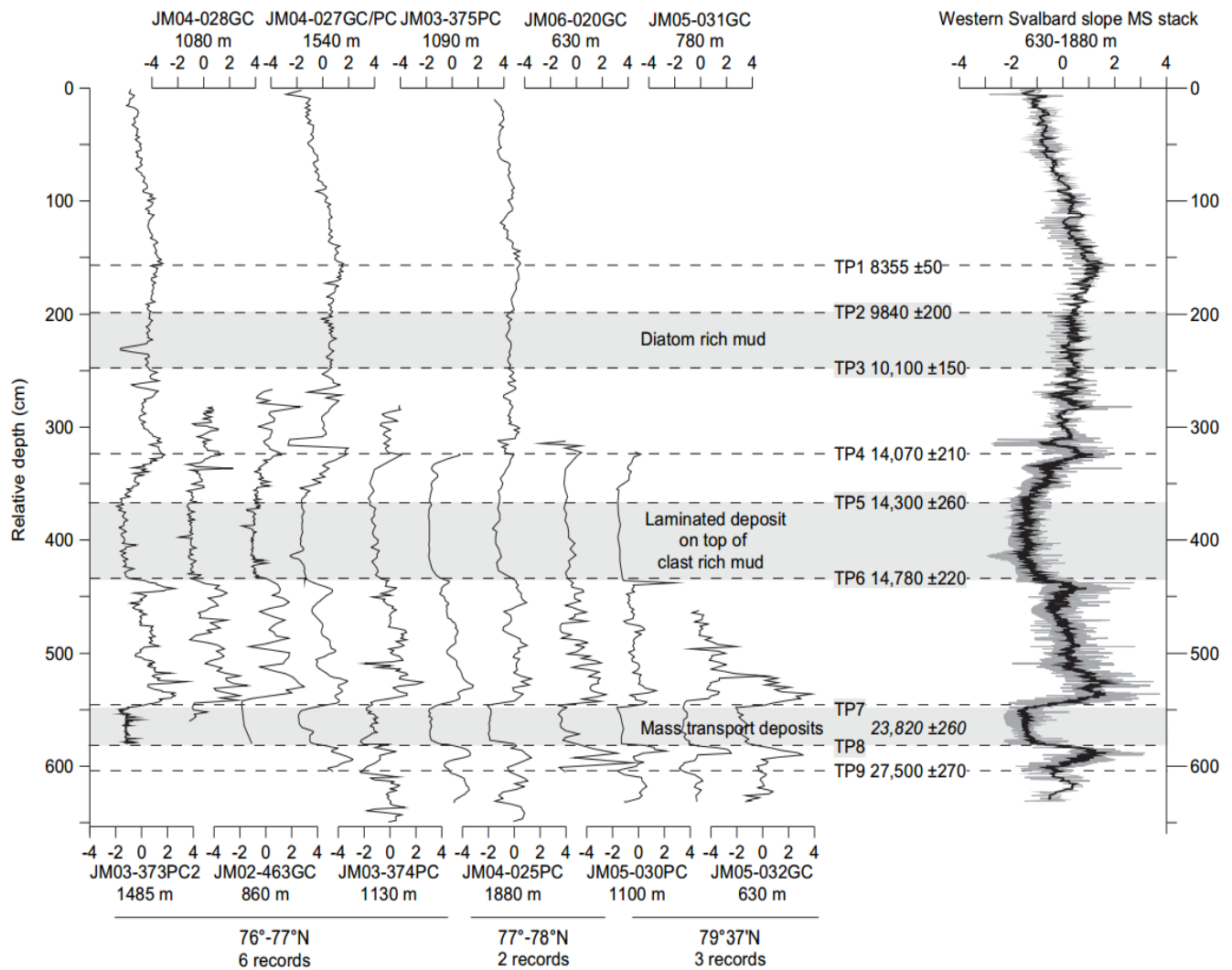
Figure 27: Magnetic susceptibility from all 11 cores from Jessen's study from western Svalbard. All the data from the magnetic susceptibility is stacked together in the figure to the right. (Jessen, et al., 2010)

Glacial activity and alterations in oceanography largely influence the magnetic susceptibility in ocean sediments. The magnetic susceptibility in the North Atlantic Ocean is linked with the strength of the bottom current and the deep-water formation in the Nordic Seas (Rasmussen, et al., 1996). Meltwater plumes and mass transportation substantially affects the magnetic susceptibility on glaciated margins (Rasmussen, et al., 2007).

Jessen (2015) provides an update from the study by Jessen et al (2010) with new calibrations of AMS ^{14}C dates based on Calib 7.1, Marine 13 on the stacked magnetic susceptibility from western Svalbard for the last 30,000 years BP. Figure 28 presents the updated ages of the tie-points. Tie-points 5 to 6 represents the event with laminated layers (15,070 to 14,600 cal years BP), and tie-points 7 to 8 signifies the mass transfer deposits (24,240 to 23,770 cal years BP).
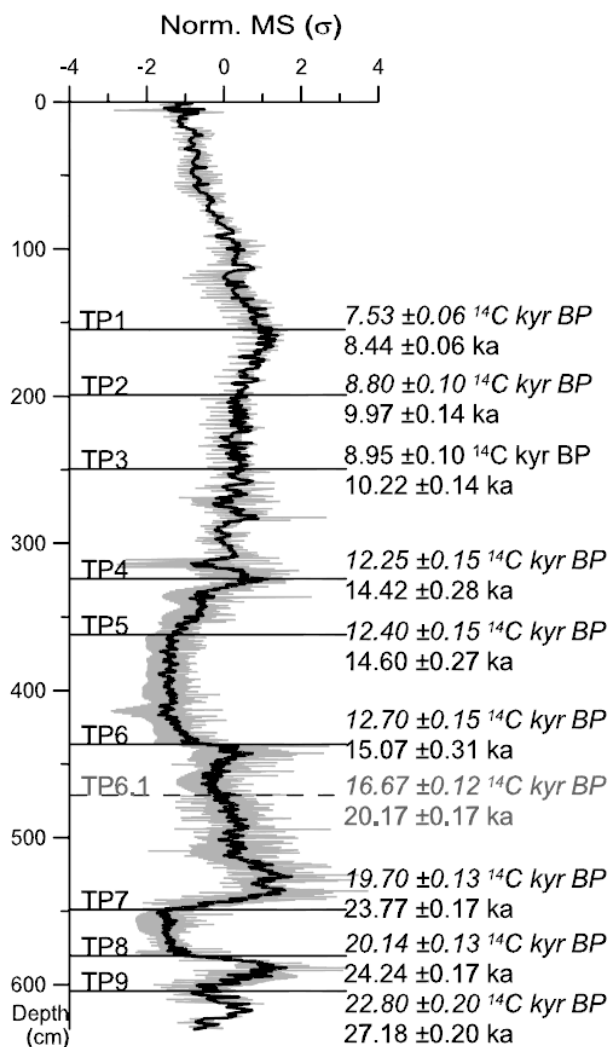
Figure 28: New ages for the stacked magnetic susceptibility from 11 cores from the western Svalbard region (Jessen, 2015).

Even though the events with laminated and dark coarse-grained sediments correlates well with features in HH16-549GC, the magnetic susceptibility does not seem to have the similar distinctively low values in HH16-549GC (Figure 29) as in the stacked magnetic susceptibility from Jessen et al (2010). This may be related to the fact that the core was retrieved within a pockmark, which might disturb the magnetic susceptibility (Sztybor & Rasmussen, 2016).

A study from Sztybor & Rasmussen (2016) reveals that the magnetic susceptibility for cores taken within an active pockmark consistently shows lower values of magnetic susceptibility in comparison to other cores taken from non-seep areas in western Svalbard. Low magnetic susceptibility in cores retrieved from pockmarks is suggested to be a local incidence associated with methane seepage (Jessen, et al., 2010; Müller & Stein, 2014). Since the HH16-549GC core has been retrieved from within a pockmark at Vestnesa Ridge, the magnetic susceptibility might be disturbed due to the dissolution of magnetic minerals occurring in methane seep sediments, which is likely to be related to the formation of paramagnetic minerals and anaerobic oxidation of methane (Sztybor & Rasmussen, 2016). The lower parts of the core have been reported to be smelly when it was retrieved, which is quite common for cores retrieved from within pockmarks. The smell can reveal the presence hydrogen sulfide in the core (Sztybor & Rasmussen, 2016). Hydrogen sulfide may imply continuous anaerobic oxidation of methane due to low accumulation rate of organic matter west of Svalbard (Müller & Stein, 2014). Hydrogen sulfide reacting with iron-bearing minerals leads to the generation of pyrite in anoxic environments containing large amounts of organic carbon. Pyrite is a paramagnetic material which is likely to alter the magnetic susceptibility with values close to zero (Rowan, et al., 2009). High content of sulfur and total organic carbon along with the presence of paramagnetic pyrite gives reason for decreasing magnetic susceptibility in periods with higher sedimentation rates as the organoclastic sulfate reduction of accumulating total organic carbon may influence the results (Sztybor, 2017).

A study from Sztybor & Rasmussen (2016) investigates a core (JM10-335GC) taken within a pockmark and another core outside the pockmark (JM10-333GC). This study records comparable coloring and shell layers to HH16-549GC studied in this thesis. The shell layer in JM10-335GC is dated to be 17,789 cal years BP. However, these results might have been altered due to diagenesis and are therefore excluded in the age establishment. The shell layer in the core retrieved outside the pockmark is estimated to occur at 16,385 cal years BP and is established as the valid dating for the shell occurrence in both cores. JM10-335GC does not reveal distinctively lower values of magnetic susceptibility during the events of laminated and mass transfer deposits, which is a similar trend to the magnetic susceptibility in HH16-549GC. Figure 29 displays the correlation of HH16-549GC in comparison to other cores retrieved from adjacent areas
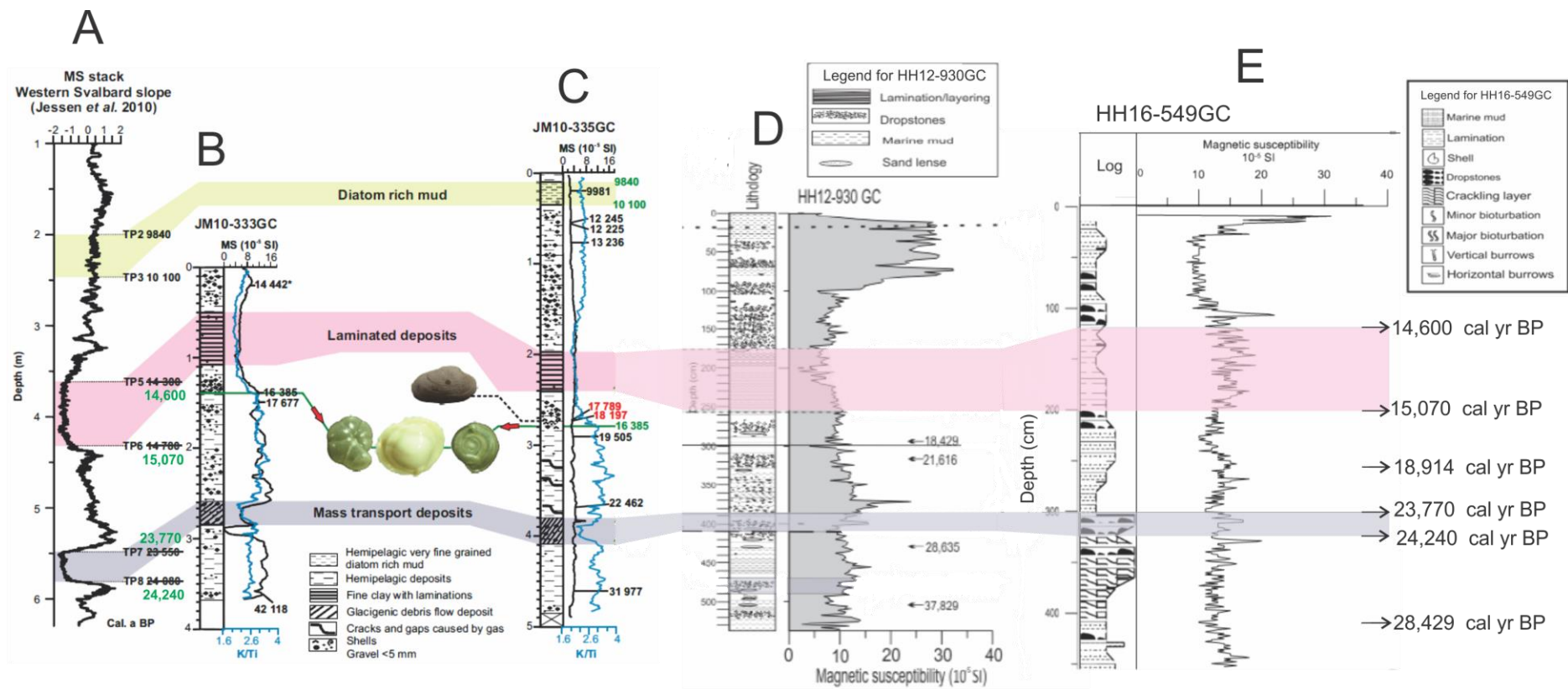
*Figure 29: Correlation of the HH16-549GC core in comparison to adjacent cores. **A**: Stacked magnetic susceptibility from the western Svalbard region in a study from Jessen et al (2010). **B**: Magnetic susceptibility from JM10-333GC taken from outside a pockmark in Vestnesa Ridge by Sztybor & Rasmussen (2016). **C**: Magnetic susceptibility from JM10-335GC taken from inside a pockmark in Vestnesa Ridge by Sztybor & Rasmussen (2016). **D**: Magnetic susceptibility from HH12-930GC taken from within a pockmark in Vestnesa Ridge by Myrvang (2015). **E**: Magnetic susceptibility for in HH16-549GC.*

In addition to the tie-points revealed by Jessen et al (2010), two radiocarbon datings have been analyzed at the [14]CHRONO centre at Queens University in Belfast, United Kingdom. These results were calibrated using Calib 7.1, Marine 13 (Stuiver, et al., 2016). The samples contained *N. pachyderma sinistral* at 258 cm and 407 cm in HH16-549GC. The sample at 258 cm has been calibrated to occur at 18,914 cal years BP, while the sample at 407 cm is estimated to be 28,249 cal years BP. The results are presented in table 4.

Table 4 reveals the sedimentation rate for the two radiocarbon datings that has been analyzed along with four tie-points from Jessen (2015) in HH16-549GC. The sedimentation rates between each of the six different tie-points are assumed to be linear and is calculated by:

$$\frac{(depth\ of\ second\ calibrated\ radiocarbon\ date\ depth\ of\ first\ calibrated\ radiocarbon\ date}{(second\ calibrated\ age - first\ calibrated\ age)} * 1000$$

Table 4: Sedimentation rates for the HH16-549GC core consisting of two radiocarbon dating and four estimates from Jessen et al (2015).

Core	Depth in HH16-549GC core (cm)	Species	14_C age	Cal. Years BP	Sedimentation rate (cm/ka)
Jessen et al (2015)	134	Nucula sp./Thyasura so./Cylichna occulta	12,450±110	14,600	140,43 (between 134 to 200 cm)
Jessen et al (2015)	200	Nucula sp./Thyasura so./Cylichna occulta	12,640±140	15,070	15,09 (between 200 to 258 cm)
HH16-549GC	258	*N. pachyderma sinistral*	16,085±71	18,914	9,68 (between 258 to 305 cm)
Jessen et al (2015)	305	*N. pachyderma sinistral*	19,570±130	23,770	21,28 (between 305 to 315 cm)
Jessen et al (2015)	315	*N. pachyderma sinistral*	21,430±160	24,240	21,91 (between 315 to 407 cm)
HH16-549GC	407	*N. pachyderma sinistral*	24,783±159	28,439	

Figure 30 displays the plot of the sedimentation rate in HH16-549GC core based on the radiocarbon datings and four tie-points from Jessen (2015)
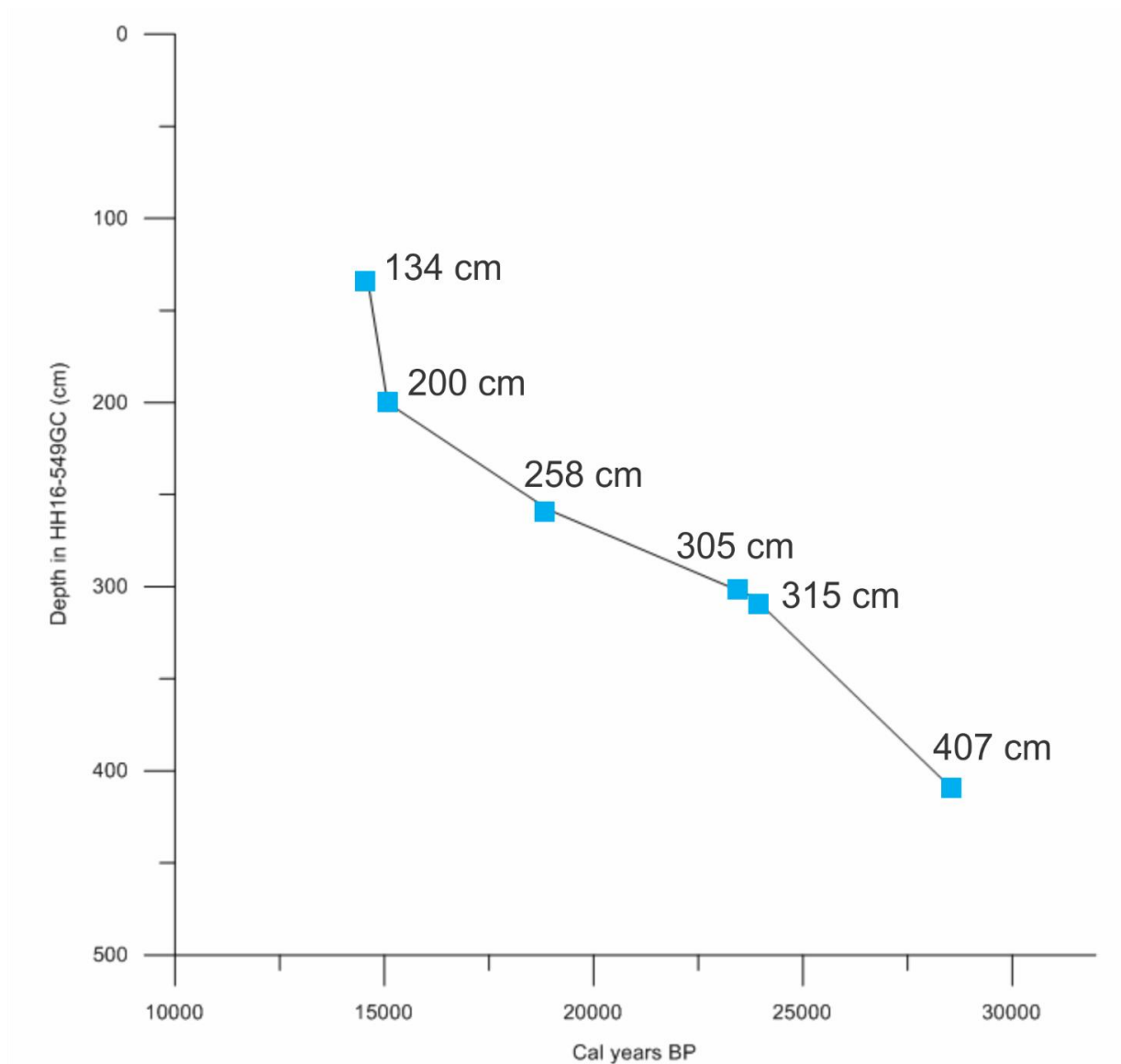
Figure 30: Plot of the sedimentation rate in the core using two radiocarbon datings and four tie-points from Jessen (2015) (Table 4). The depth of the core is plotted in relation to calibrated years BP.

The sedimentation rate in HH16-549GC has a decreasing trend from 407 cm (21,91 cm/ka) to 258 cm (9,68 cm/ka). From 258 cm the sedimentation rate increases to 15,09 cm/ka before increases significantly after 200 cm (140,43 cm/ka).

Age estimations in HH16-549GC is carried out by assuming a linear sedimentation rate between the calibrated radiocarbon dates. The calculation was carried out by the following equation:

$$y = ax + b$$

$$a = \frac{y - b}{x}$$

$$a = \frac{(second\ calibrated\ date - first\ calibrated\ date)}{(depth\ of\ second\ calibrated\ date - depth\ of\ first\ calibrated\ date)}$$

$$b = y - (ax)$$

$$b = calibrated\ date - (a * depth\ of\ calibratet\ date)$$

$$y = ax + b$$

$$y = a * (desired\ depth\ for\ age\ estimation) + b$$

5 Discussion

5.1 Age model

The events of laminated and mass transfer deposits described in the study from Jessen et al (2010) and the transition between three Marine Isotope Stages has been crucial to construct an age model for the HH16-549GC core. The laminated deposits are found between 134 cm to 200 cm with an age of 14,600 cal years BP and 15,070 cal years BP respectively. The deposit is from the mass transport event and occurs from 305 cm (23,770 cal years BP) to 315 cm (24,240 cal years BP) in the core. These results are correlated with Marine Isotope Stages (MIS) in HH16-549GC to get an even more detailed age model. Three Marine Isotope Stages have been identified in this study (Figure 35). Zamelczyk et al (2014) suggest that Marine Isotope Stage 2 (MIS 2) lasted from 28,800 cal years BP to 15,400 cal years BP. Lisiecki & Raymo (2005) however, proposes that MIS2 occurred from 29,000 ka to 14,000 ka, which will be the basis for this study. The age of the core from bottom to top is suggested to be from 31,000 to 7500 cal years BP by assuming linear sedimentation rates between the datings. MIS 2 is characteristic for having maximum $\delta^{18}O$ values and is therefore presumed to occur from 85 cm to 445 cm in the core (Figure 35). Benthic $\delta^{18}O$ does however negative excursion at 233 cm (≈17,400 cal years BP) to 361 cm (≈26,300 cal years BP), which could be related to Heinrich events (Bond, et al., 1993) and the presence of bivalve shells (Figure 32).

The transition between Marine Isotope Stage 1 (MIS 1) and MIS 2 is interpreted to occur at around 85 cm (≈ 14,000 cal years BP) and is indicated by decreasing benthic $\delta^{18}O$ (Figure 35). The transition from MIS 2 and MIS 3 is suggested to be distinguished by an increasing abundance of foraminifera and a peak in IRD concentration just before the event (Bylinskaya, et al., 2016). Figure 36 shows that this event is likely to be located 445 cm in HH16-549GC.

Table 5 is the foundation of the sedimentation rate in the HH16-549GC core. The table includes two radiocarbon datings done in this study at the [14]CHRONO centre at Queens University in Belfast, United Kingdom, four tie-points from Jessen (2015) and three tie-points situated at the the transition between MIS 1 and MIS 2, shift from MIS 2 to MIS 3 and the transition from Bølling-Allerød/Younger Dryas to the Holocene period.

Table 5: Sedimentation rates for the HH16-549GC core consisting of two radiocarbon dating, four estimates from Jessen et al (2015) and the interpretation of the transition between Bølling-Allerød and Holocene, and from marine isotope stage 1 to marine isotope stage 2

Core	Depth in HH16-549GC core (cm)	Species	14_C age	Cal. Years BP	Sedimentation rate (cm/ka)
Transition from Bølling-Allerød to Holocene	53			11,700	13,91 (between 53 cm and 134 cm)
Shift from MIS1 to MIS2	85			14,000	81,6 (between 85 cm and 134 cm)
Jessen et al (2015)	134	Nucula sp./Thyasura so./Cylichna occulta	12,450±110	14,600	140,43 (between 134 to 200 cm)
Jessen et al (2015)	200	Nucula sp./Thyasura so./Cylichna occulta	12,640±140	15,070	15,09 (between 200 to 258 cm)
HH16-549GC	258	*N. pachyderma sinistral*	16,085±71	18,914	9,68 (between 258 to 305 cm)
Jessen et al (2015)	305	*N. pachyderma sinistral*	19,570±130	23,770	21,28 (between 305 to 315 cm)
Jessen et al (2015)	315	*N. pachyderma sinistral*	21,430±160	24,240	21,91 (between 315 to 407 cm)
HH16-549GC	407	*N. pachyderma sinistral*	24,783±159	28,439	67,74 (between 407 and 445 cm)
Shift from MIS2 to MIS3	445			29,000	

Figure 31 displays the plot of the final sedimentation rate in the HH16-549GC core with all 9 identified dating points from table 5.
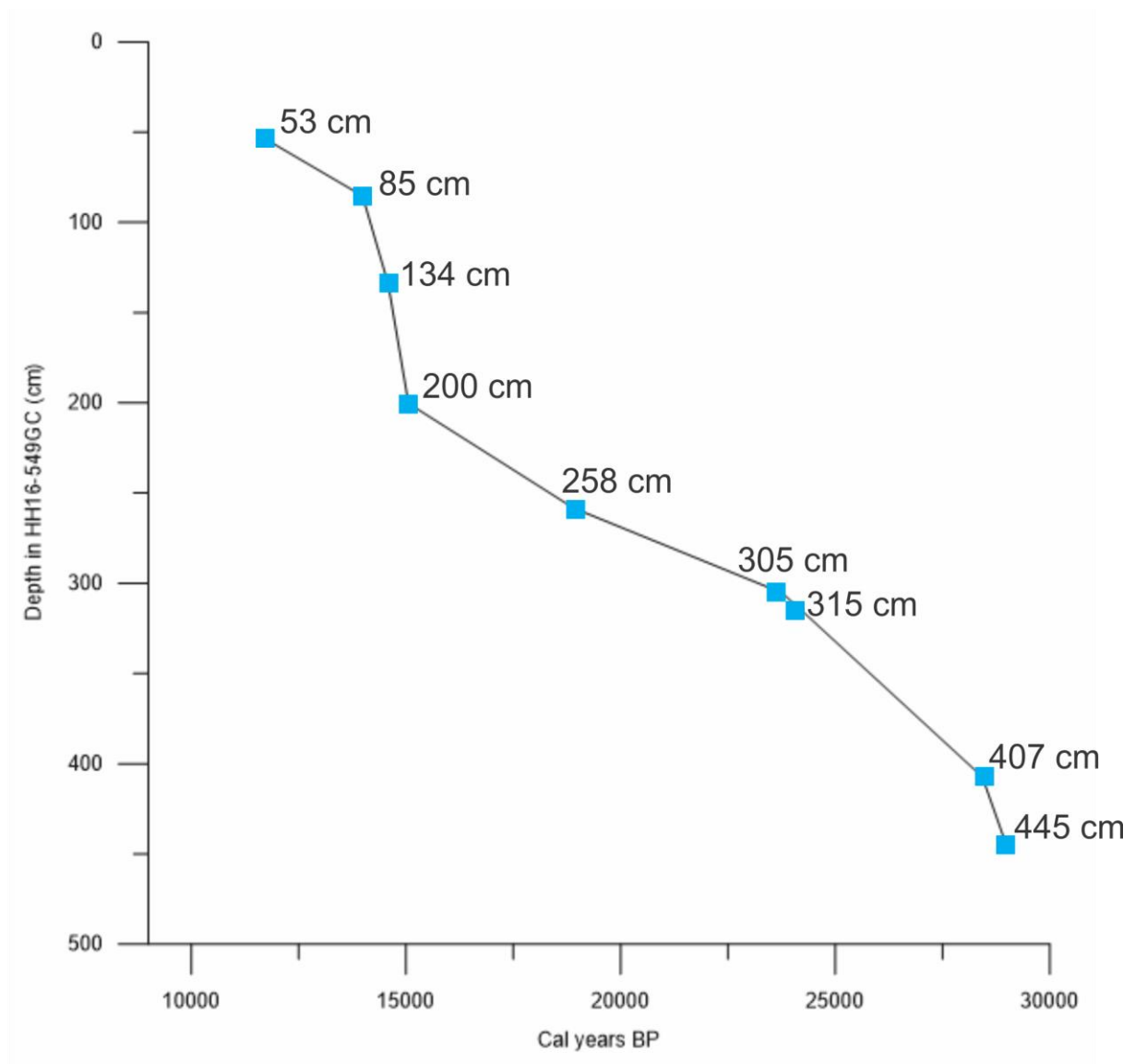

Figure 31: Plot of the sedimentation rate in the core using two radiocarbon datings, four tie-points from Jessen (2015), as well as the interpreted transition between MIS 1 and MIS 2, shift from MIS 2 to MIS 3 and the transition between Bølling-Allerød interstadials and Younger Dryas to Holocene (Table 5). The depth of the core is plotted in relation to calibrated years BP.

The sedimentation rate in HH16-549GC is relatively high from 462 cm to 407 cm (67,74 cm/ka) before it decreases from 407 cm to 315 cm (21,91 cm/ka). During the mass transport deposition event (Heinrich event 2) from 315 cm to 305 cm the sedimentation rate decrease marginally to 21,28 cm/ka. The sedimentation rate is at its lowest point throughout the core recording 9,68 cm/ka from 305 cm to 258 cm. The sedimentation rate from 258 cm to 200 cm increased slightly to 15,09 cm/ka. The laminated layers occurring from 200 cm to 134 cm recorded remarkably higher sedimentation rates at 140,43 cm/ka. At the transition from MIS 1 and MIS 2 (85 cm), the sedimentation rate decreased slightly to 81,6 cm/ka. From 85 cm the sedimentation rate decreased significantly to 13,91 cm/ka. The sedimentation rate at the top and the bottom of the core lacks data and is therefore assumed to have the same sedimentation rate as the closest date record. The sedimentation rate in HH16-549GC correlates relatively well with the stacked sedimentation rate in the study from Jessen et al (2010) except for deviations occurring in the Holocene and during Heinrich event 2 (Figure 36), which is probably caused by lack of more detailed data in HH16-549GC.

The time periods in HH16-549GC is defined by investigating the available data in this study in comparison to other relevant studies. The Marine Isotope Stages are characterized mainly by examining $\delta^{18}O$. In HH16-549GC MIS 3 is interpreted to occur from around 31,000 to 29,000 cal years BP, MIS 2 from 29,000 to 14,000 cal years BP and MIS 1 from 14,000 to 7500 cal years BP. Other relevant and more detailed time periods interpreted to occur in HH16-549GC are the Last Glacial Maximum (26,800-20,671 cal years BP), the early deglaciation (20,671-19,327 cal years BP), Heinrich event 1 (19,327-15,600 cal years BP), Bølling-Allerød interstadial (15,600-11,700 cal years BP) and Holocene (11,700-7,500 cal years BP).

MIS 3 only comprises the very end of the core and will not be discussed in details. MIS 3 is characterized with decreasing $\delta^{18}O$, low concentration of benthic and planktic foraminifera at the transition zone between MIS 3 and MIS 2, and a small peak in the concentration of IRD towards the very end of the zone (Chauhan, et al., 2014). Heinrich event 3 is marked by a yellow-like coloring (Figure 33) and is assumed to occur around 30,500 cal years BP (Bond, et al., 1993). This event is correlated with Rasmussen & Thomsen (2013) and can be seen in figure 32.

Lisiecki & Raymo (2005) suggest that MIS 2 spans from 29,000 to 14,000 cal years BP in HH16-549GC (445-85 cm) (Figure 35). This isotope stage is identified by high $\delta^{18}O$ values and comprises time periods like the Last Glacial Maximum, early deglaciation, Heinrich event 1 and 2 and the start of the Bølling-Allerød interstadials.

Heinrich event 2 is revealed by a distinctive dark coloring (Figure 33) and correlates with Jessen (2015) as an event with mass transfer deposits from 24,240 cal years BP to 23,770 cal years BP (Figure 29). This event has along with Heinrich event 3 been correlated with a study from Rasmussen & Thomson (2013) (Figure 32). Similar for both Heinrich event 2 and Heinrich event 3 is that both events recorded increased concentration of detrital calcium carbonate from ice rafting (Figure 32) (Hemming, 2004).
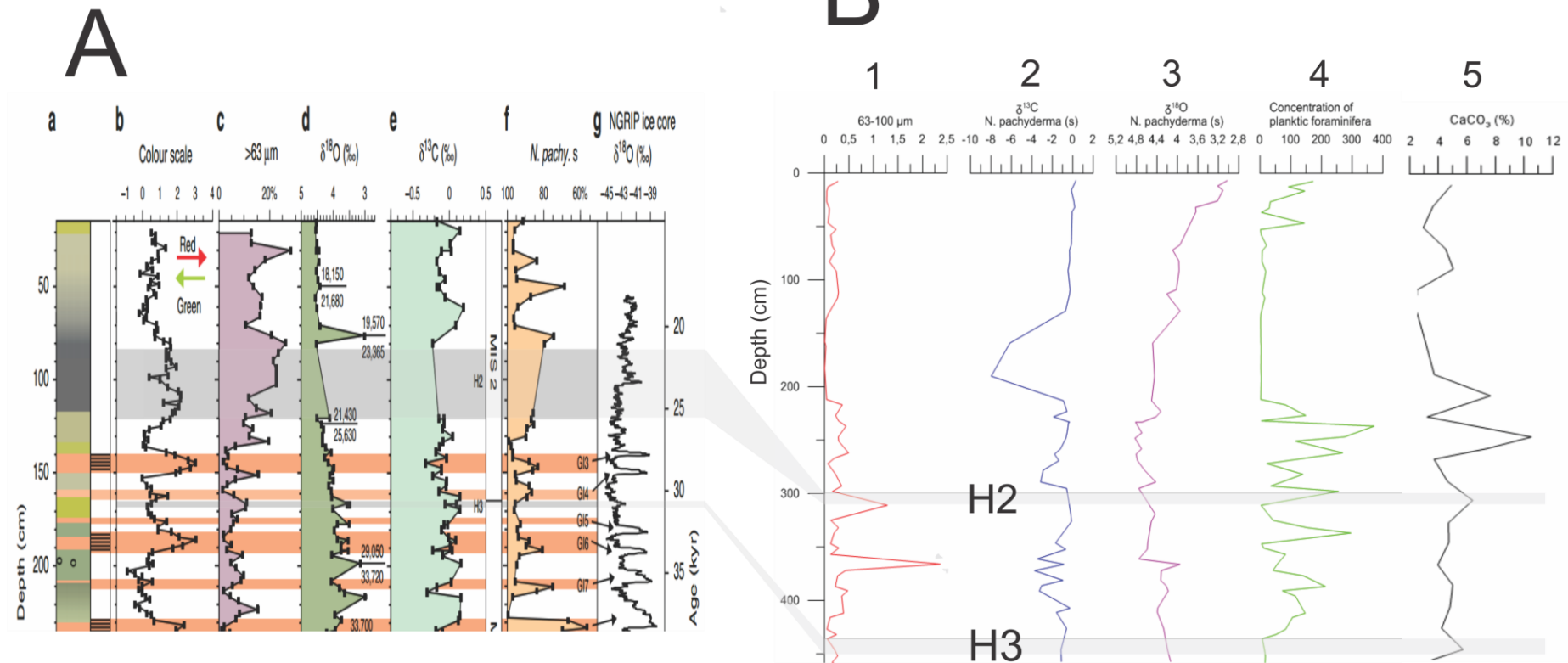
Figure 32: **A**: Illustration from (Rasmussen & Thomson, 2013) with highlighting features from Heinrich event 2 and 3. **B**: Graphs from the HH16-549GC core. **(a)** Lithological log with colour differences. **(b)** Colour scale. **(c)** >63 µm fraction. **(d)** Planktic $\delta^{18}O$ values. **(e)** Planktic $\delta^{13}C$ values. **(f)** Amount of N. pachyderma sinistral. **(1)** 63-100 µm fraction from HH16-549GC. **(2)** Planktic $\delta^{18}O$ values from HH16-549GC **(3)** Planktic $\delta^{18}O$ values from HH16-549GC. **(4)** Concentration of planktic foraminifera from HH16-549GC. **(5)** Percentage of calcium carbonate in HH16-549GC.

70

The Last Glacial Maximum is characterized by fluctuating grain sizes and varying concentration of foraminifera with seasonally ice-free conditions and is distinguished by having high $\delta^{18}O$ values (Hebbeln, et al., 1994; Nørgaard-Pedersen, et al., 2003; Rasmussen, et al., 2007; Zamelczyk, et al., 2014). This period is interpreted to occur from around 26,800 to 20,671 cal years BP in HH16-549GC.

The early deglaciation is proposed to occur from 20,500 cal years BP to 17,400 cal years BP (Jessen, et al., 2010), but in HH16-549GC this period is suggested to occur from 20,671 to 19,327 cal years BP. The transition from the Last Glacial Maximum to the early deglaciation is marked by increasing concentration of all grain sizes (Figure 36), increased concentration of both planktic and benthic foraminifera (Figure 36), increasing content of total carbon and decreasing concentration of total organic carbon (Figure 38) (Hebbeln, et al., 1994; Knies, et al., 2001).

Heinrich event 1 is interpreted to occur from 19,327 to 15,600 cal years BP in HH16-549GC, which is fairly similar to the study from Jessen et al (2010) which suggest the period to occur from 19,637 to 15,732 cal years BP. This period is characterized by a higher concentration of planktic foraminifera as a result of retreating ice sheets leading to more open-ocean conditions (Figure 36) (Zamelczyk, et al., 2014). A study from Heinrich (1988) reveals that mineral grains in the grain sizes from 63-100 µm and 100-500 µm increase in this period before it diminishes towards the end of the event. These results coincide well with results from HH16-549GC (Figure 36). Bond et al (1993) records low values of both benthic and planktic $\delta^{18}O$ and high concentration of IRD in this period. In HH16-549GC low values of benthic and planktic $\delta^{18}O$ are occurring during the later stages of Heinrich event 1 (Figure 37) with a low peak at 218 cm (≈16,400 cal years BP). These results correlates well with results from Sztybor & Rasmussen (2017) revealing a drop in planktic $\delta^{18}O$ at 16,500 cal years BP.

The Bølling-Allerød interstadial and Younger Dryas is suggested to occur from 15,600 cal years BP to 11,700 cal years BP in HH16-549GC. Laminated deposits are proposed to be deposited in the start of this period from 15,070 to 14,600 cal years BP (Jessen, 2015). The laminated layers are observed from 134 cm to 200 cm in HH16-549GC in the x-ray photography (Figure 34). The laminated deposit is revealed by very low grain sizes of all fractions and low concentration of benthic and planktic foraminifera (Figure 36) (Jessen, et al., 2010).

A study from Aagaard-Sørensen et al (2014) records a remarkable depletion in both planktic and benthic $\delta^{13}C$ during the event, which correlates well with HH16-549GC (Figure 37).

Jessen et al (2010) propose that the Holocene started at 11,700 cal years BP. The transition from Bølling-Allerød interstadials and Younger Dryas to the Holocene period is marked by increasing concentration of planktic foraminifera (Figure 36) and further decreasing values of planktic and benthic $\delta^{18}O$ (Figure 37) (Slubowska-Woldengen, et al., 2007). Slubowska et al (2005) report of high concentration of IRD from the start of the Holocene until 10,100 cal years BP. Jessen et al (2010) indicate that hardly any icebergs were present from 10,100 cal years BP to 7600 cal years BP on the western Svalbard margin. Figure 36 reveals that these trends also occur in HH16-549GC and is considered to be a good indicator of the Holocene period. A small assemblage of diatoms was possibly found in the 63-100 µm fraction at 26 cm (≈ 9800 cal years BP) in HH16-549GC, which possibly can be correlated to diatom-rich layers observed in several cores from western Svalbard occurring from around 10,100 to 9840 cal years BP (Jessen, et al., 2010). The assemblage of diatoms in HH16-549GC is however limited, which makes the assumption uncertain.

*Figure 33: Interpretation of the high-resolution images in HH16-549GC using Avaatech XRF core scanner. **A**: Laminated deposits. **B**: Heinrich event 2 (mass transfer deposits). **C**: Bivalve shell-layer. **D**: Heinrich event 3.*
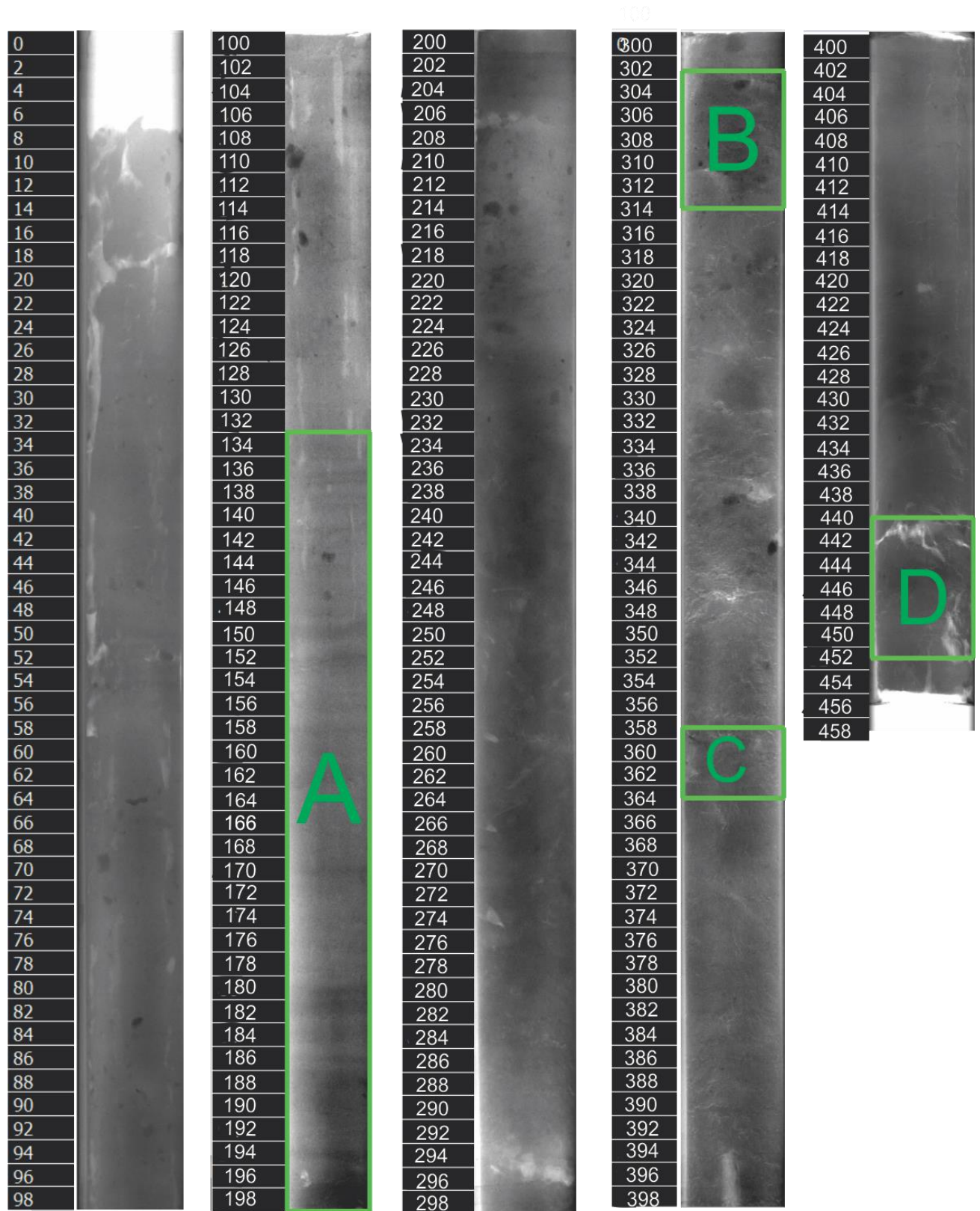
Figure 34: X-ray images of the HH16-549 GC core. **A**: Laminated deposits. **B**: Heinrich event 2 (mass transfer deposits). **C**: Bivalve shell-layer. **D**: Heinrich event 3.
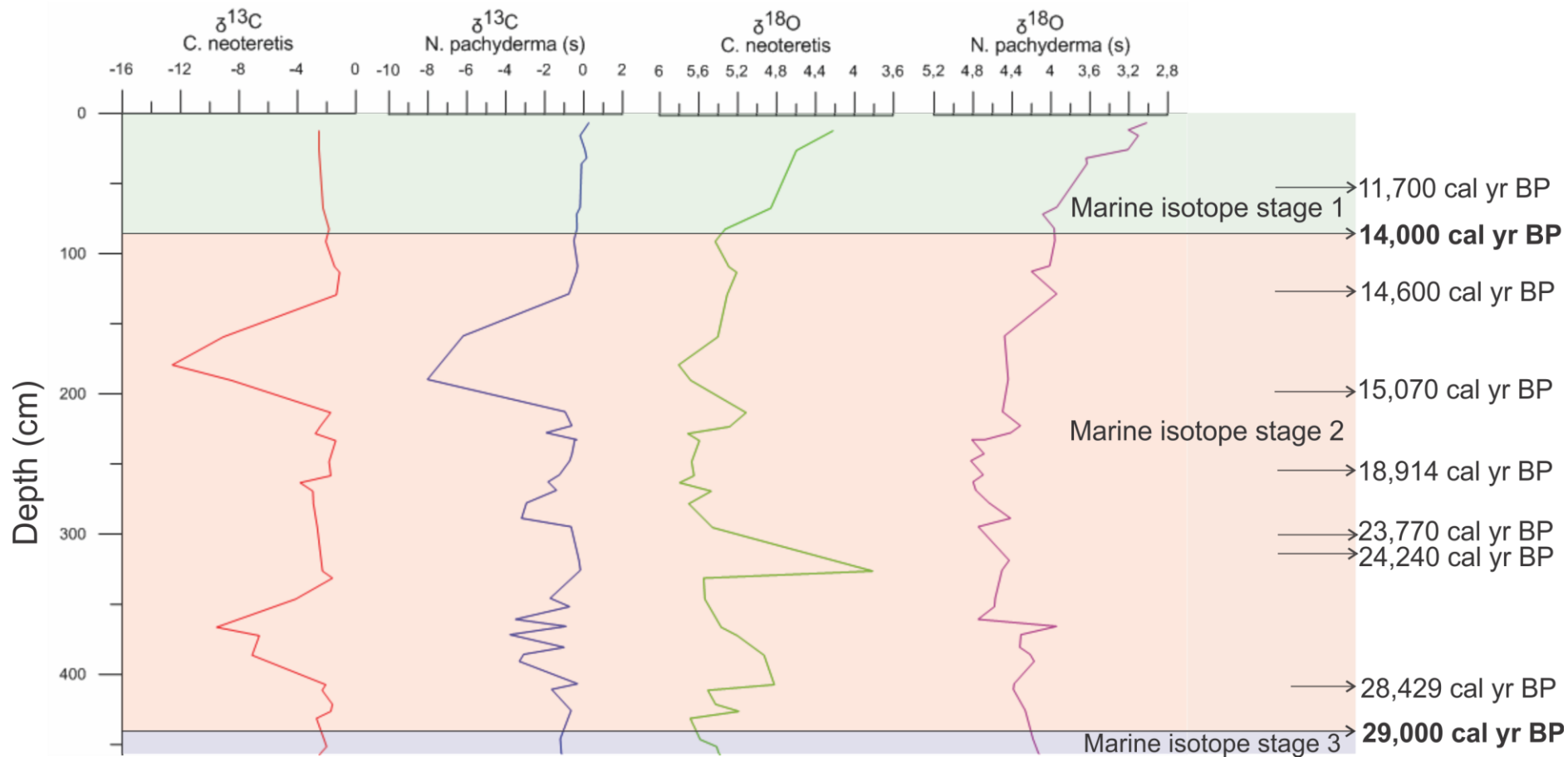
Figure 35: Interpretation of marine isotope stages in HH16-549GC. The shift between Marine Isotope Stage 1 and Marine Isotope Stage 2 is suggested to occur at 14,000 cal years BP, while the transition from Marine Isotope Stage 2 and Marine Isotope Stage 3 is proposed to occur at 29,000 cal years BP (Lisiecki & Raymo, 2005).
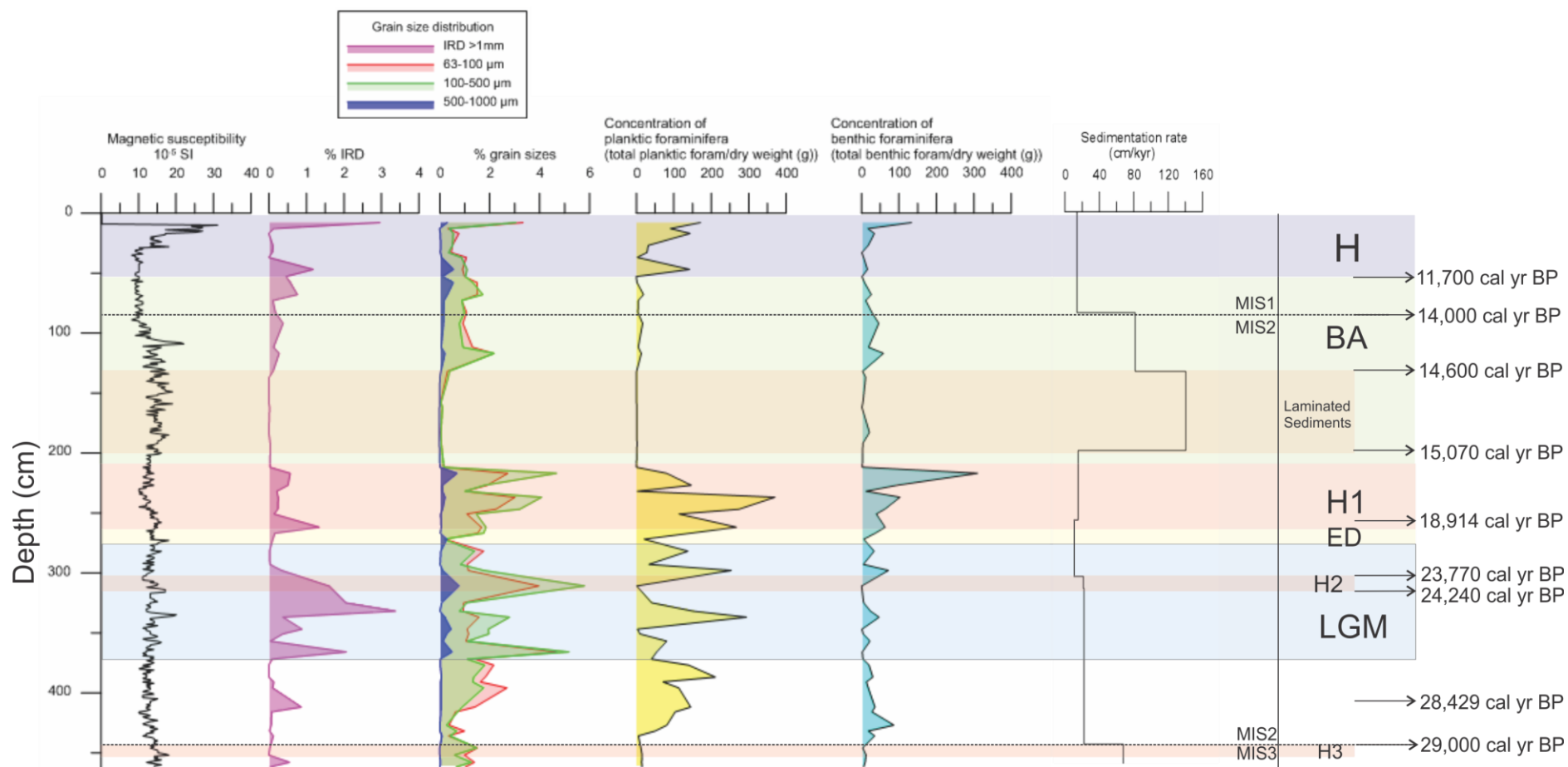
*Figure 36: Interpretation of the time periods in the HH16-549GC core. This figure presents the magnetic susceptibility, distribution of grain sizes, concentration of planktic and benthic foraminifera and the sedimentation rate for the core. The dotted line represents the transition between the Marine Isotope Stages. **H**: Holocene. **BA**: Bølling-Allerød. **H1**: Heinrich event 1. **ED**: Early deglaciation. **H2**: Heinrich event 2. **LGM**: Last Glacial Maximum. **H3**: Heinrich event 3. **MIS 1**: Marine Isotope Stage 1. **MIS 2**: Marine Isotope Stage 2. **MIS 3**: Marine Isotope Stage 3.*
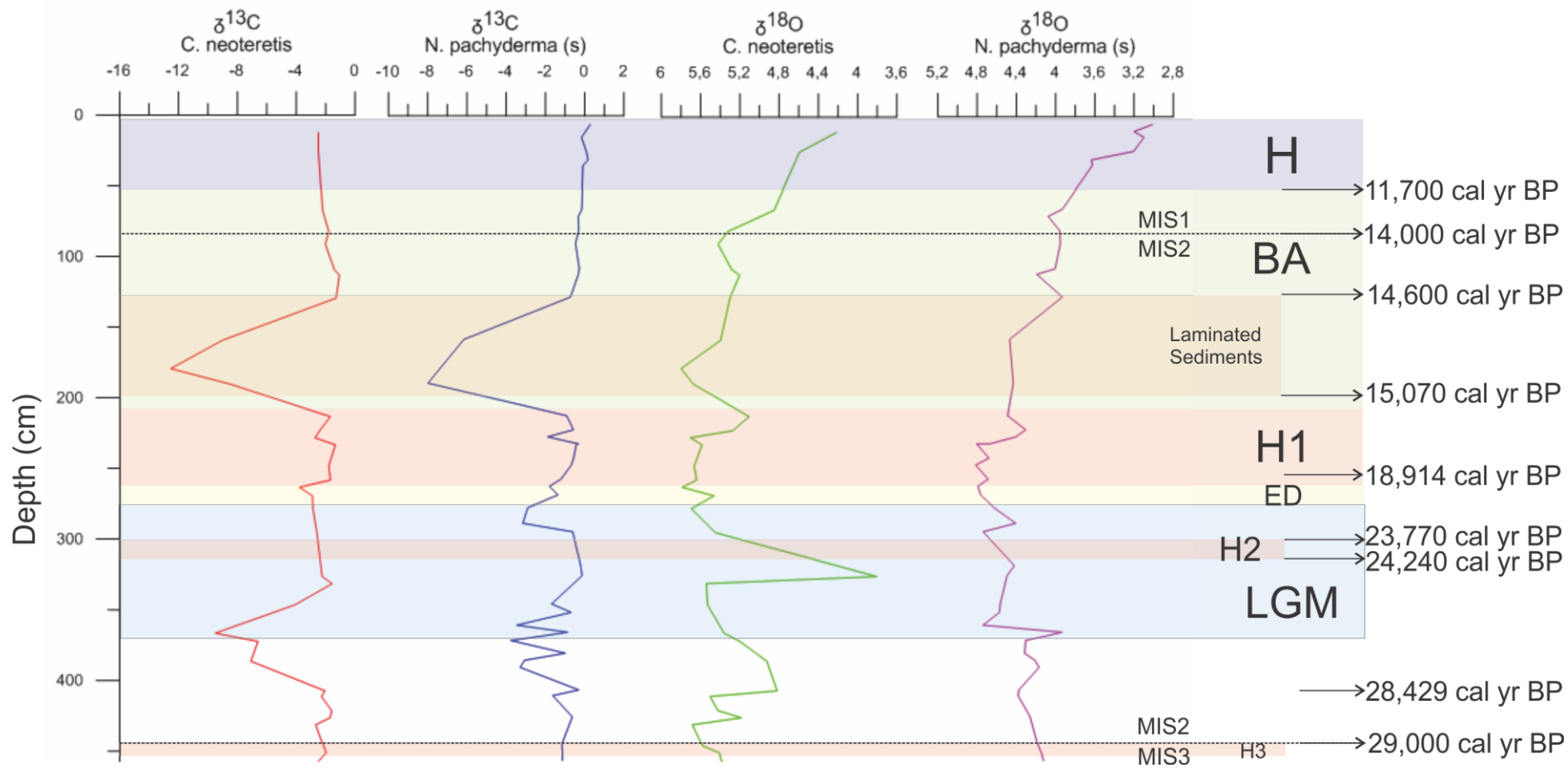
Figure 37: Interpretation of the stable isotope analysis for the HH16-549GC core. The dotted line represents the transition between the Marine Isotope Stages. **H**: Holocene. **BA**: Bølling-Allerød. **H1**: Heinrich event 1. **ED**: Early deglaciation. **H2**: Heinrich event 2. **LGM**: Last Glacial Maximum. **H3**: Heinrich event 3. **MIS 1**: Marine Isotope Stage 1. **MIS 2**: Marine Isotope Stage 2. **MIS 3**: Marine Isotope Stage 3.
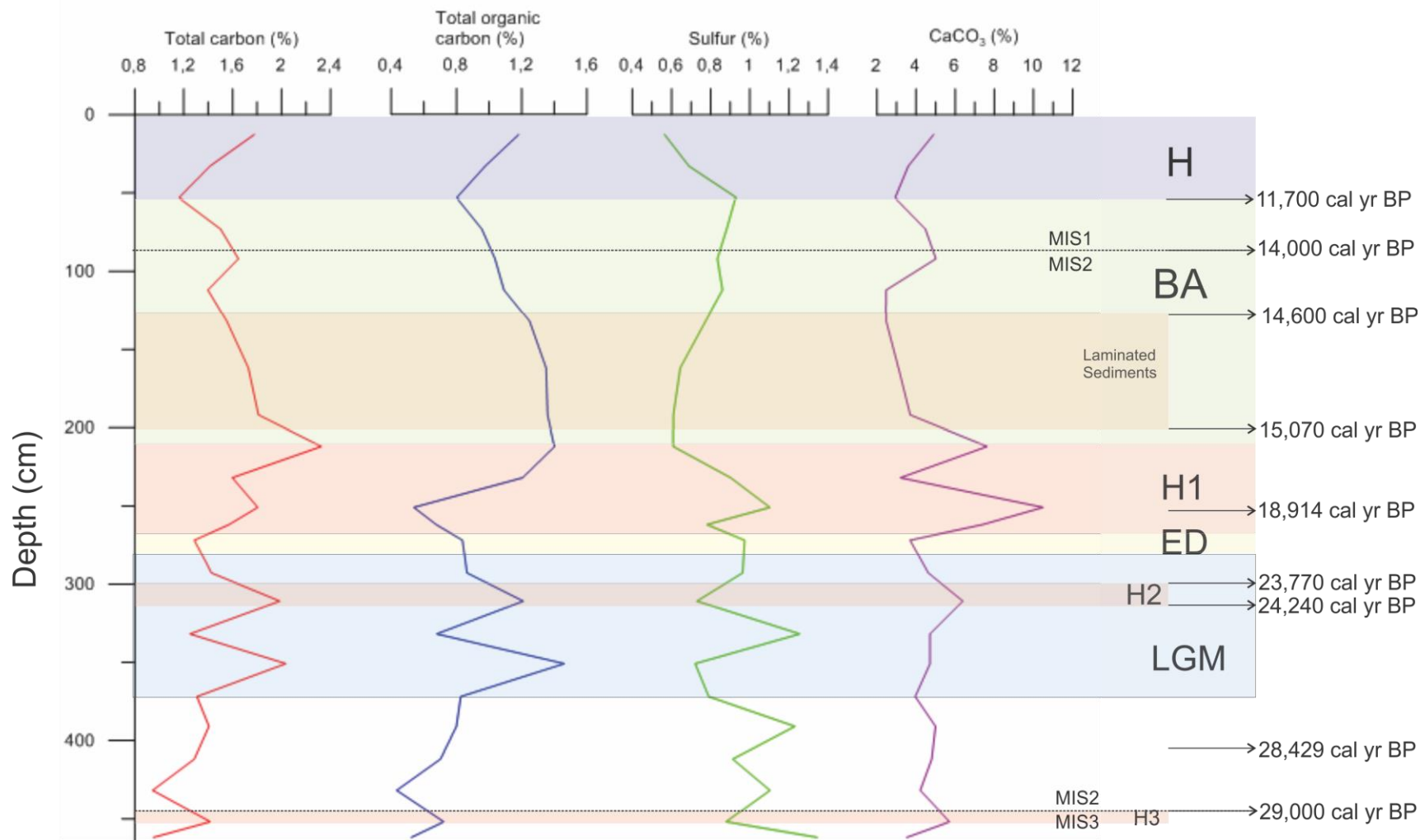
Figure 38: Interpretation of total carbon, total organic carbon, sulfur and calcium carbonate ($CaCO_3$) in the HH16-549GC core. The dotted line represents the transition between the Marine Isotope Stages. **H**: Holocene. **BA**: Bølling-Allerød. **H1**: Heinrich event 1. **ED**: Early deglaciation. **H2**: Heinrich event 2. **LGM**: Last Glacial Maximum. **H3**: Heinrich event 3. **MIS 1**: Marine Isotope Stage 1. **MIS 2**: Marine Isotope Stage 2. **MIS 3**: Marine Isotope Stage 3

5.2 Paleoceanography at Vestnesa Ridge (31,000-7500 cal years BP)

5.2.1 Marine Isotope Stage 3 (31,000-29,000 cal years BP)

Lisiecki & Raymo (2005) has defined the Marine Isotope Stage 3 to occur from 57 ka to 29 ka. In HH16-549GC this stage is interpreted to occur from 462 cm to 445 cm in the core with estimated ages from 31,000 to 29,000 cal years BP respectively (Figure 35). The concentration of IRD in the sediments often increases in transitions between glacial and interglacial periods, but not in the transition from MIS 3 to MIS 2. (Chauhan, et al., 2014). The shift from MIS 1 to MIS 2 records high abundance of IRD, whereas the concentration is very low in the transition from MIS 3 to MIS 2 (Figure 36). A study from Chauhan et al (2014) from Yermak Plateau reports of decreasing concentration of both planktic and benthic foraminifera towards the very end of MIS 3, which is similar to records in HH16-549GC (Figure 36). Heinrich event 3 is proposed to occur at the end of MIS 3 and will be discussed in chapter 5.2.1.1. Figure 39 illustrates the proposed environment during MIS 3 in Yermak Plateau, north of Vestnesa Ridge.
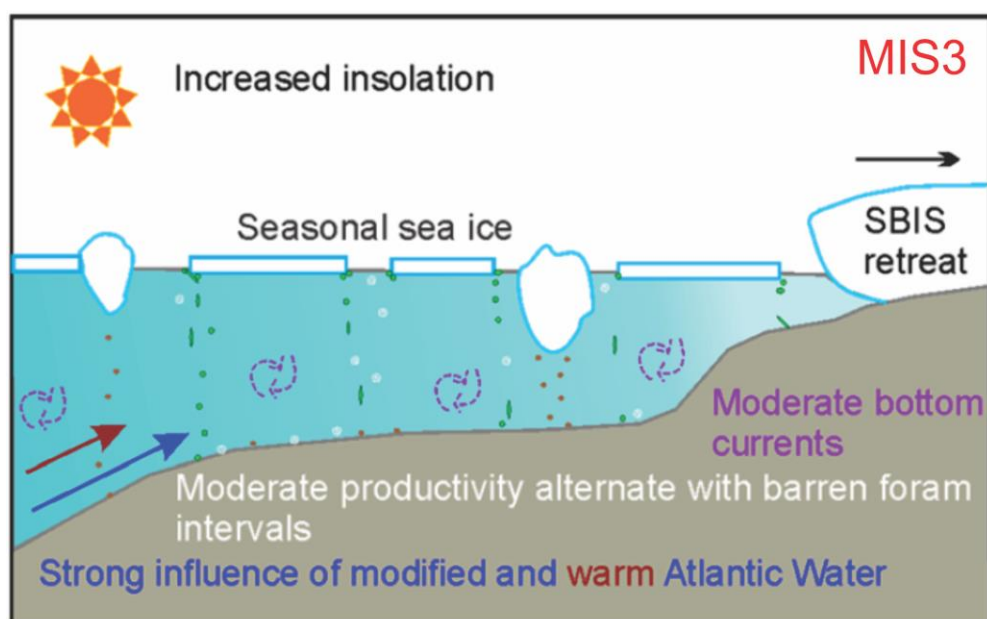
Figure 39: Suggested environment during Marine Isotope Stage 3 (MIS 3) in the Yermak Plateau, North of Vestnesa Ridge. Modified from (Chauhan, et al., 2016).

5.2.1.1 Heinrich event 3 (30,500 cal years BP)

Heinrich event 3 has been identified to occur during MIS 3 in HH16-549GC (Figure 33). Bond et al (1993) suggest that Heinrich event 3 occurred from 32,539 to 30,085 cal years BP, but there are uncertainties of exactly when the event occurred in the North Atlantic. This event is characterized by a distinctive yellow coloring described to be olive brown in HH16-549GC (Figure 20), which is similar to the description in a study from Myrvang (2015) who describes the coloring to be light olive brown. Figure 32 correlates results from HH16-549GC with a study from Rasmussen & Thomsen (2013) documenting characteristic features for Heinrich event 3. It is evident that the assemblage of *N. pachyderma sinistral* (the planktic foraminifera in HH16-549GC mainly consists of *N. pachyderma sinistral*) is low during Heinrich event 3 along with high planktic $\delta^{13}C$ and $\delta^{18}O$ values. The onset of Heinrich event 3 is considered to be gradual and not abrupt (Gwiazda, et al., 1996). Increased concentration of IRD just before Heinrich event 3 is anticipated to occur as a result of lower concentration of foraminifera with a constant and small increase of lithic material (Gwiazda, et al., 1996; Chauhan, et al., 2014), which can be correlated to HH16-549GC (Figure 36). Relatively high values of planktic isotopes occurs straight after this event (Figure 37) which may indicate high ventilation in the water column and a general climate warming (Spielhagen & Erlenkeuser, 1994).

Mutual for all Heinrich events identified in this study is that they contain higher concentration of calcium carbonate (Figure 38), which also is revealed in a study from Hemming (2004). Figure 38 reveals a rapid increase in the concentration of total carbon and total organic carbon during this event, which might be related to enhanced methane seepage (Sztybor & Rasmussen, 2017). Zamelczyk et al (2014) suggest that these findings may indicate Arctic surface water and seasonal sea ice.

5.2.2 Marine Isotope Stage 2 (29,000-14,000 cal years BP)

Lisiecki & Raymo (2005) suggest that Marine Isotope Stage 2 occurred from 29 ka to 14 ka. This event has been interpreted to occur from 85 cm to 275 cm in the HH16-549GC core (Figure 35). The sea surface conditions in Fram Strait during MIS 2 is considered to be very fluctuating due to alterations in advection of Atlantic water masses towards higher latitudes (Hebbeln, et al., 1994). Seasonally ice-free environments occurred as a result of further inflow of saline and warm Atlantic water masses leading to destabilization the ice sheets in the Svalbard-Barents Sea leading to occasional discharge of meltwater (Hebbeln, et al., 1994; Nørgaard-Pedersen, et al., 2003; Rasmussen, et al., 2007). The concentration of IRD and sedimentation rates in western Svalbard were low in the period from 30,000 to 27,000 cal years BP, which might indicate less ice rafting in this period (Andersen, et al., 1996; Mangerud, et al., 1998). The low concentration of IRD may be a result of the presence of cold-based thin ice due to the advance of ice towards the shelf break which is assumed to carry less IRD (Andersen, et al., 1996). Low concentration of IRD accompanied by low sedimentation rates (Figure 36) may signify a steady ice front with low calving rate (Andersen, et al., 1996). A relatively high concentration of IRD appearing at 412 cm (28,500 cal years BP) may indicate that the ice sheets approached the shallow shelf with the sea level remaining relatively low (Peltier & Fairbanks, 2006; Jessen, et al., 2010). The concentration of total carbon and total organic carbon remains relatively low until the start of the Last Glacial Maximum, which might reveal colder temperatures as the insolation from the sun was very low in this period (Figure 44). Figure 40 illustrates the proposed environment during MIS 2 and the Last Glacial Maximum in Yermak Plateau, north of Vestnesa Ridge.
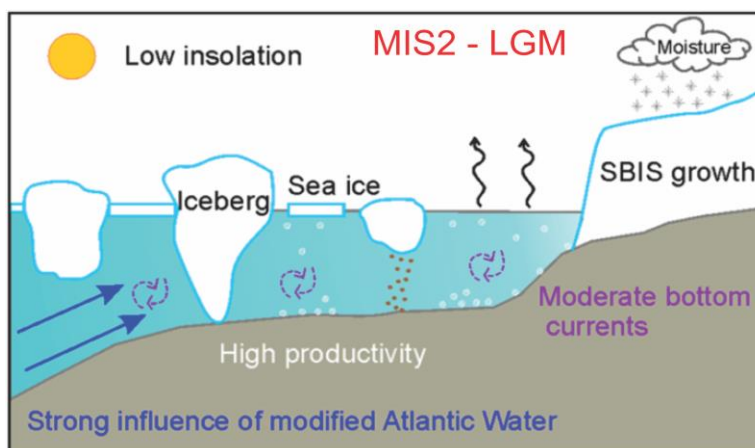

Figure 40: Suggested environment during Marine Isotope Stage 2 (MIS 2) and the Last Glacial Maximum (LGM) in the Yermak Plateau, North of Vestnesa Ridge. Modified from (Chauhan, et al., 2016).

5.2.2.1 Last Glacial Maximum (26,800-20,671 cal years BP)

The Last Glacial Maximum is considered to be one of the most difficult time periods to reconstruct in the Svalbard margin because of inconsistency in the data set. The shelf of western Svalbard is anticipated to be covered by grounded ice during the Last Glacial Maximum (Elverhøi, et al., 1995). Jessen et al (2010) characterize this period with increasing amount of IRD, which correlates well with the high IRD concentration in HH16-549GC (Figure 36). According to Hald et al (2001), the high peaks in IRD concentration are caused by increased moisture and lower insolation leading to the growth of the Svalbard-Barents Sea Ice-Sheets. A relatively thin ice cover developed as a result of the ice progressing towards the shelf break of western Svalbard. (Andersen, et al., 1996). HH16-549GC records low $\delta^{13}C$ values and high concentration of IRD at 370 cm ($\approx$26,700 cal years BP) (Figure 37). This occurrence is suggested to indicate the start of the glaciers progressing towards the shelf (Figure 41) (Elverhøi, et al., 1995; Andersen, et al., 1996; Vogt, et al., 2001) and is supported by the global sea level declining towards a minimum at 25,000 cal years BP (Peltier & Fairbanks, 2006). High values of $\delta^{18}O$ are recorded throughout the LGM (Figure 37), which may imply an incursion of marginally warmer and saline Atlantic water and conditions with open water (Spielhagen & Erlenkeuser, 1994) and a homogenous surface water mass (Nørgaard-Pedersen, et al., 2003). The ocean circulation in this period is likely to be comparable to the present-day ocean circulation with Atlantic water flowing from south towards the north along the Svalbard margin (Hebbeln, et al., 1998; Nørgaard-Pedersen, et al., 2003; Rasmussen, et al., 2007).

Müller & Stein (2014) proposes that Fram Strait was covered with a thick and stationary ice-cover during the later period of the Last Glacial Maximum. HH16-549GC records decreasing concentration of IRD and planktic foraminifera from 300 cm ($\approx$23,200 cal years BP) to the early deglaciation ($\approx$20,000 cal years BP), which may indicate less calving of icebergs (Andersen, et al., 1996). Thinner ice layers are suggested to transport only smaller amounts of debris (Elverhøi, et al., 1998). Figure 41 illustrates a reconstruction of the evolution of the Barents Sea ice sheets from 10,000 cal years BP to 31,400 cal years BP by Hebbeln et al (1994).
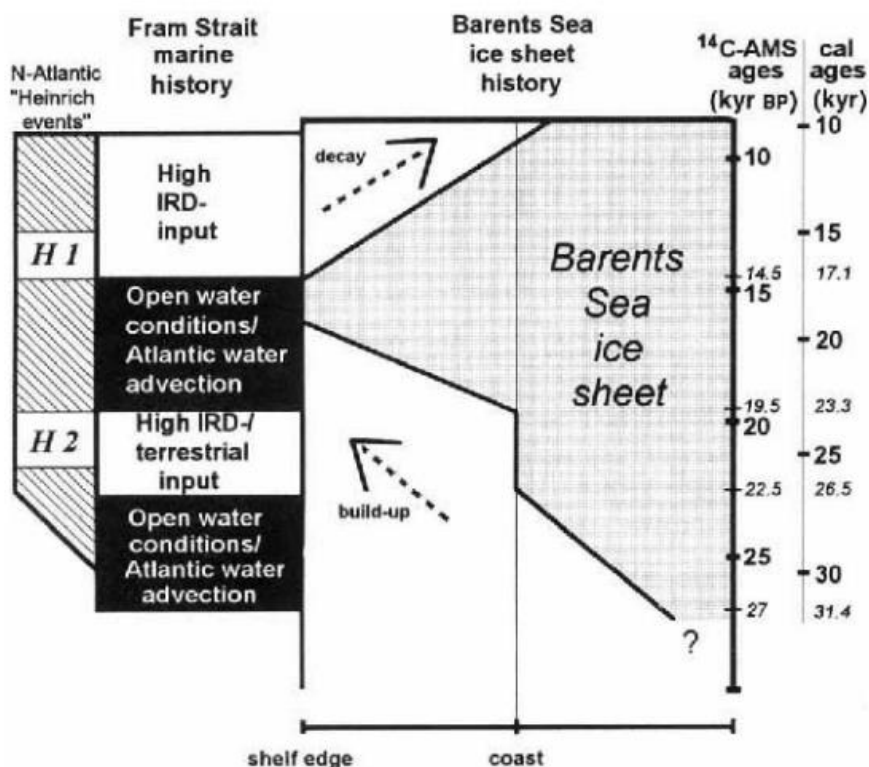
Figure 41: Reconstruction of the evolution of the Barents Sea ice sheets in Fram Strait. Illustration from (Hebbeln, et al., 1994).

Periods with higher abundance of IRD seems to correlate well with increased concentration of planktic foraminifera (Figure 36), which is linked with enhanced primary production in Fram Strait (Nørgaard-Pedersen, et al., 2003; Rasmussen, et al., 2007; Zamelczyk, et al., 2014). In the Last Glacial Maximum the Atlantic inflow is considered to be fluctuating but strong enough to provide an increased abundance of planktic foraminifera (Zamelczyk, et al., 2014). Fram Strait is suggested to have periods with open water and seasonally ice-free conditions during these events (Hebbeln, et al., 1994). Ice-free conditions in this period may be revealed by the high quantity of benthic and planktic foraminifera as the production of phytoplankton needs sufficient supply of insolation and nutrients with open water conditions (Smith, 1995). *N. pachyderma sinistral* is dominating the assemblage of planktic foraminifera in HH16-549GC, which is considered to be an indication of cold environment at the sea surface (Zamelczyk, et al., 2014). Low content of calcium carbonate remains relatively low through the Last Glacial Maximum except for a high peak occurring at Heinrich event 2 (Figure 38).

Zamelczyk et al (2014) suggest that low content of $CaCO_3$ during this event is associated with the presence of Arctic surface water and seasonal sea ice. This statement is supported by a very low concentration of planktic foraminifera in periods with high $CaCO_3$ during the LGM as the planktic foraminifera occupies the upper water column and may be inhibited by the presence of sea ice. The concentration of total carbon and total organic carbon remained relatively low until approximately 26,750 cal years BP, which can be explained by colder temperatures as the insolation from the sun was very low in this period (Figure 43). This is supported by the global sea level declining towards a minimum at around 25,000 cal years BP (Peltier & Fairbanks, 2006).

5.2.2.2 Heinrich event 2 (24,240-23,770 cal years BP)

Heinrich event 2 is described as a mass transport deposition with low magnetic susceptibility occurring in the period from 24,240 cal years BP to 23,770 cal years BP in western Svalbard (Jessen, et al., 2010). A similar debris flow has been examined in a study from Andersen et al (1996) and is proposed to occur at the peak of the glacial period due to instability in the upper slope, suggested to indicate a fully glaciated shelf (Laberg & Vorren, 1995; Vorren & Laberg, 1997; King, et al., 1998; Dowdeswell & Elverhøi, 2002). Jessen et al (2010) suggest that the entire western Svalbard shelf was completely glaciated at 23,820 cal years BP. The pore pressure in the underlying glacigenic sediments increased as a result of considerable amounts of glacigenic material in the upper slope (Laberg & O., 1995; Elverhøi, et al., 1997, 2002). The mass transportation event is characterized by increased quantity of IRD, low magnetic susceptibility and higher sedimentation rates of coarser material (Figure 36). The magnetic susceptibility in HH16-549GC is not a distinctively low as the stacked magnetic susceptibility recorded in the study from Jessen et al (2010). The magnetic susceptibility in HH16-549GC might be disturbed because the core was retrieved from within a pockmark, which has been observed in several other studies in this area (e.g Sztybor & Rasmussen, 2016). The sedimentation rate in HH16-549GC is not particularly high in this event due to lack of tie-points used for dating in this area (Table 5). Increased sedimentation rate as reported by Jessen et al (2010), is likely to lead to higher degree of preservation of organic matter and allowing more total organic carbon to be buried within the sediments avoiding full degradation at the seafloor (Müller & Stein, 2014). Figure 38 reveals that the concentration of total organic carbon was significantly higher during this event in HH16-549GC

Mass transportation close to sediments containing clathrates could result in increased discharge from gas hydrates (Owen, et al., 2007). A study from Sztybor & Rasmussen (2017) from Vestnesa Ridge records high content of total carbon and total organic carbon at around 24,000 cal years BP. Figure 38 reveals that this event contains significantly high values of both total carbon and total organic carbon in HH16-549GC, meaning it might be related to methane seepage as suggested by Owen et al (2007). Similar to Heinrich event 3, the concentration of calcium carbonate is high during Heinrich event 2 (Figure 38).

A similar distinctive dark coloring (dark reddish brown) as recorded in Heinrich event 2 is evident at around 345 cm (≈25,600 cal years BP) in HH16-549GC (Figure 33). This event has similar characteristics as Heinrich event 2 containing significantly higher concentration of both total carbon and total organic carbon with low content of sulfur (Figure 38) and a decreasing abundance of planktic foraminifera (Figure 36). It is therefore likely that this event is a similar mass transportation event with smaller magnitude taking place around 25,600 cal years BP in HH16-549GC. Figure 42 illustrates how the climate can affect different processes for mass movement during glaciation and deglaciation and is relevant to understand the processes that happen during Heinrich events.
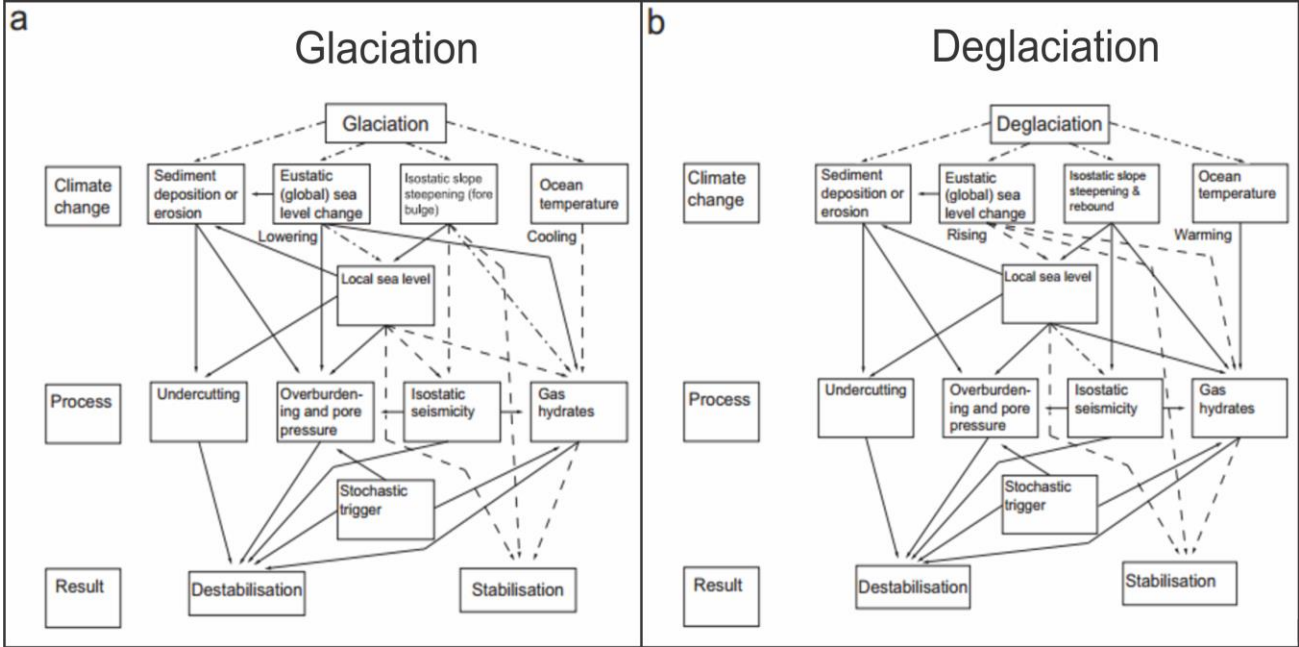

Figure 42: Illustration of how climate changes affect different processes for mass movement. Dashed lines indicate stabilizing factors, solid lines indicate destabilizing factors and dash-dot-dash lines signifies processes that could be both stabilizing and destabilizing. (a) Process during glacial periods (b) Processes during deglacial periods. Modified from (Owen, et al., 2007).

5.2.2.3 Early deglaciation (20,671-19,327 cal years BP)

The study from Jessen et al (2010) proposes that the early deglaciation started between 21,200 and 19,800 cal years BP. This coincides well with increasing summer insolation in this period (Figure 43) (Laskar, et al., 2004). The early deglaciation in HH16-549GC is suggested to start at 20,671 cal years BP, and is in good accordance with a study from Myrvang (2015) who proposes the period to start in 20,101 cal years BP in the HH12-930GC core. Increasing concentration of IRD has been recorded shortly after 20,000 cal years BP in the northeastern part of Svalbard, and is proposed to be an indication of retreating ice sheets leading to enhanced calving of the icebergs (Siegert & Dowdeswell, 1995; Elverhøi, et al., 1995; Knies, et al., 2001). Hebbelen et al (1994) suggest that increasing concentration of IRD and planktic foraminifera (Figure 36) along with decreasing content of total organic carbon (Figure 38) characterizes the early deglaciation, which coincides well with results from HH16-549GC in this period.
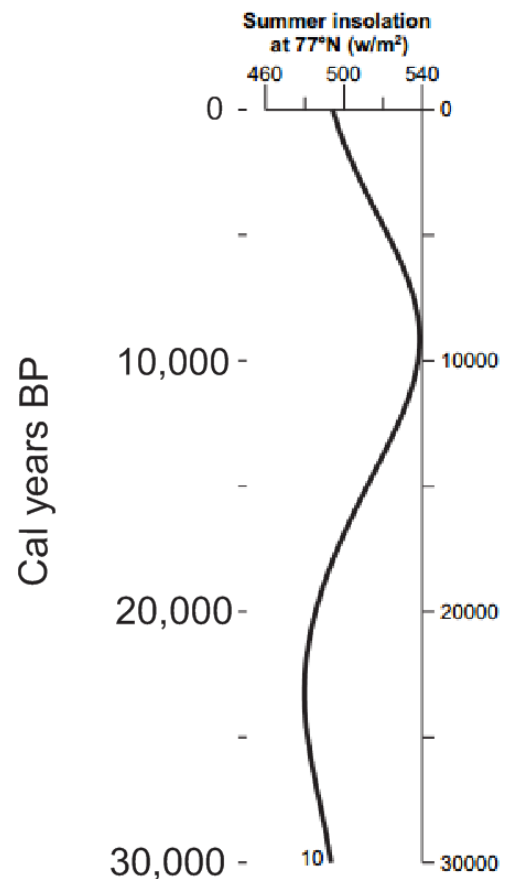
Figure 43: Summer insolation at 77°N. Figure modified from (Laskar, et al., 2004).

The glacial margin could also start to retreat as a consequence of less precipitation and lower atmospheric temperatures in the western Svalbard region (Gildor & Tziperman, 2001). Jessen et al (2010) observe a lower quantity of IRD in the period from 20,000 cal years BP to 15,600 cal years BP and interpret it to be a result of lower accumulation of snow leading to the retreat of the glaciers. In HH16-549GC this trend is observed from 295 cm to 267 cm (22,700-19,800 cal years BP) and from 251 cm to 232 cm (18,200-17,200 cal years BP). Figure 44 illustrates

the proposed environment during the early deglaciation in Yermak Plateau, north of Vestnesa Ridge.
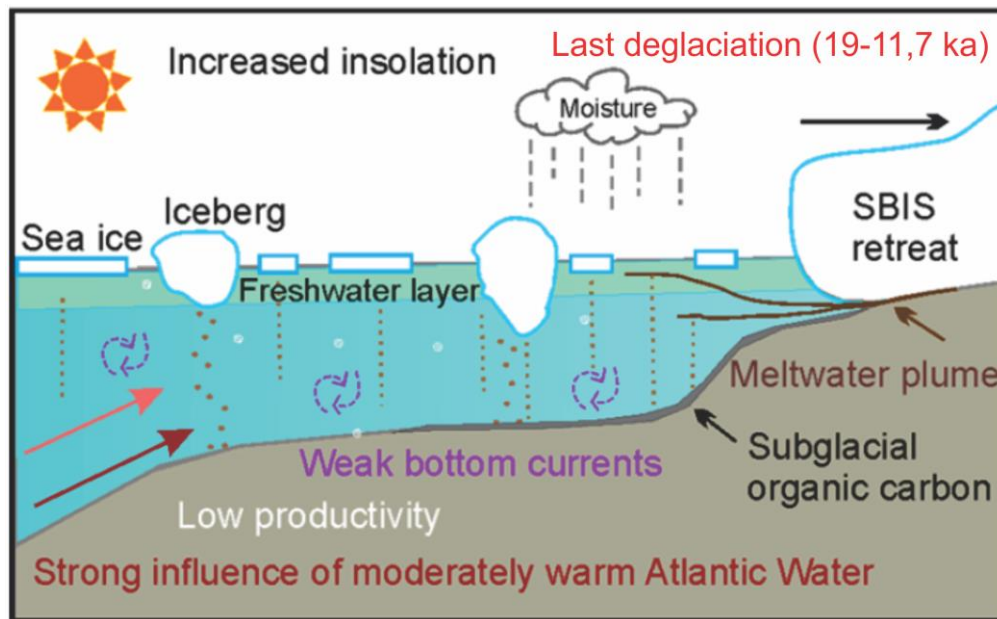
Figure 44: Suggested environment in the last deglaciation in the Yermak Plateau. Modified from (Chauhan, et al., 2016).

The stacked chronology in the study from Jessen et al (2010) reveals lower sedimentation rates in the western Svalbard region in this period, which coincides well with the sedimentation rate in HH16-549GC being at its lowest point throughout this period (Figure 36). Higher insolation from the sun along with warmer flow from the West Spitsbergen Current caused the glaciers to recede, which in turn may lead to altering flow and discharge of meltwater linked with fluctuating values of $\delta^{18}O$ (Figure 37) (Broecker, et al., 1985). Zamelczyk et al (2014) suggest that the Atlantic water inflow was less intense in the early deglaciation as the surface waters sustained a cooling trend. HH16-549GC records a high peak in both benthic and planktic $\delta^{18}O$ towards the end of the early deglaciation which might be linked with cold and polar environments. The abundance of planktic foraminifera increased significantly towards the end of the early deglaciation (Figure 36) and is likely to imply the presence of cold water masses in Fram Strait (Zamelczyk, et al., 2014).

5.2.2.4 Heinrich event H1 (19,327-15,600 cal years BP)

Heinrich event 1 occurred from 17,400 cal years BP to 15,700 cal years BP according to Jessen et al (2010). The start of this event is anticipated to begin as early as 19,637 cal years BP and end at 15,732 cal years BP in HH16-549GC. Heinrich events generally occur at the end of a longer cooling period leading to a warmer period (Patton, et al., 2011) and linked to an increasing supply of freshwater to the ocean emerging from ice sheets. Heinrich was the first to report a larger amount of lithic materials (>180 µm) in sediment cores in 1988 (Heinrich, 1988). After more studies of Heinrich events, these anomalies could be detected over several areas within the North Atlantic Ocean (Grousset, et al., 1993; Hemming, 2004). Figure 36 reveals that the grain sizes ranging from 63-100 µm, 100-500 µm and >1 mm increase rapidly during Heinrich event 1. These events have a global impact on the climate as the freshwater causes stratification of the upper water column and diminish the strength of deep-water formation (Bradley, 2015). Heinrich event 1 is characterized by lower values of stable isotopes, higher concentration of IRD and dominance of the planktic foraminifera *N. pachyderma* (Zamelczyk, et al., 2014). A study from Elverhøi et al (1995) reports of a substantial increase of IRD from 19,400 cal years BP to 14,800 cal years BP, which correlates well with enhanced concentration of IRD from 262 cm (≈19,327 cal years BP) to 217 cm (≈16,200 cal years BP) in HH16-549GC. Increasing concentration of IRD and higher sedimentation rates in Heinrich event 1 is probably a result of a reduction of the Svalbard-Barents Sea Ice-Sheets (Chauhan, et al., 2014). The receding of the glaciers occurring as a result of less precipitation of snow in the period from 20,000 to 15,600 cal years BP corresponds well with lower sedimentation rates and moderate concentrations of IRD (Jessen, et al., 2010). The flux of icebergs to the open ocean is reduced as the ice streams retreated and collapsed following the abrupt warming during the Heinrich event (Bond, et al., 1993). Increasing concentration of *Neogloboquadrina pachyderma sinistral* typically appear just before the event is starting (Bradley, 2015) and diminish after as a result of increased dissolution and lower productivity (Figure 36) (Broecker, et al., 1992; Broecker, 1994).

Variations in the Atlantic meridional overturning circulation is associated with occurrences of Heinrich events (Bradley, 2015). Transport of heat towards the poles was weakened by a continuous decline of the Atlantic meridional overturning circulation as a result of further fresh water supply at the surface of the North Atlantic Ocean starting at 19,000 cal years BP (Stanford, et al., 2011).

Warm saline ocean waters are transported from tropical regions and sinks when it meets the colder North Atlantic ocean, which is likely to lead to an alteration of the formation of North Atlantic Deep Water with ventilation of the deeper parts of the ocean causing a slowdown of the thermohaline circulation (Bradley, 2015). The thermohaline circulation collapsed at approximately 17,500 cal years BP, leading to cold conditions in the North Atlantic (Stanford, et al., 2011).

Heinrich event 1 generally records low values of both benthic and planktic $\delta^{18}O$ and high concentration of IRD (Bond, et al., 1993), which could imply further reduction in ice sheets (Rasmussen, et al., 2007). These observations may imply increased warming of the bottom water which might influence the meltwater at the surface (Rasmussen, et al., 2007; Chauhan, et al., 2014). Sediment cores from the Svalbard region reveals lower value of planktic $\delta^{18}O$ after 17,400 cal years BP which is possibly linked with receding glaciers in Britain and south of Scandinavia (Jessen, et al., 2010). Several studies shows that the value of benthic $\delta^{18}O$ is likely to decrease in Heinrich Event 1, but in less degree than the planktic $\delta^{18}O$ (Figure 37) (Rasmussen, et al., 2007; Myrvang, 2015). Figure 37 reveals a sudden drop in both planktic and benthic $\delta^{18}O$ at 219 cm ($\approx$16,300 cal years BP) and is likely to coincide with the same observation from Jessen et al (2010). Lower values of $\delta^{18}O$ in Fram Strait and in the Nordic Seas is proposed to imply diminishing flow of the Atlantic Water and surface stratification due to the presence of relatively fresh and cold surface water masses (Rasmussen, et al., 1996, 2007; Bauch, et al., 2001) and is related to the deglaciation of Svalbard (Elverhøi, et al., 1995; Andersen, et al., 1996). Declining values of $\delta^{18}O$ in the North Atlantic leads to substantial freshening and warming of the sea surface (Müller & Stein, 2014) and weakened ocean circulation along with decreasing salinity in the water column (Chauhan, et al., 2014). Sztybor & Rasmussen (2017) records very low values of planktic $\delta^{18}O$ at approximately 16,500 cal years BP, which coincides well with results from HH16-549GC (Figure 37). High concentration of foraminifera along with decreasing value of $\delta^{18}O$ occuring between 16,900 to 15,900 cal years BP corresponds to enhanced primary production due to higher nutrient levels and further addition of freswater (Müller & Stein, 2014). High values of $\delta^{13}C$ during Heinrich event 1 (Figure 37) may indicate good ventilation of the surface waters (Spielhagen & Erlenkeuser, 1994). Figure 45 displays the evolution of the sea ice in Fram Strait and the Arctic ocean from the late part of the Last Glacial Maximum to Younger Dryas.
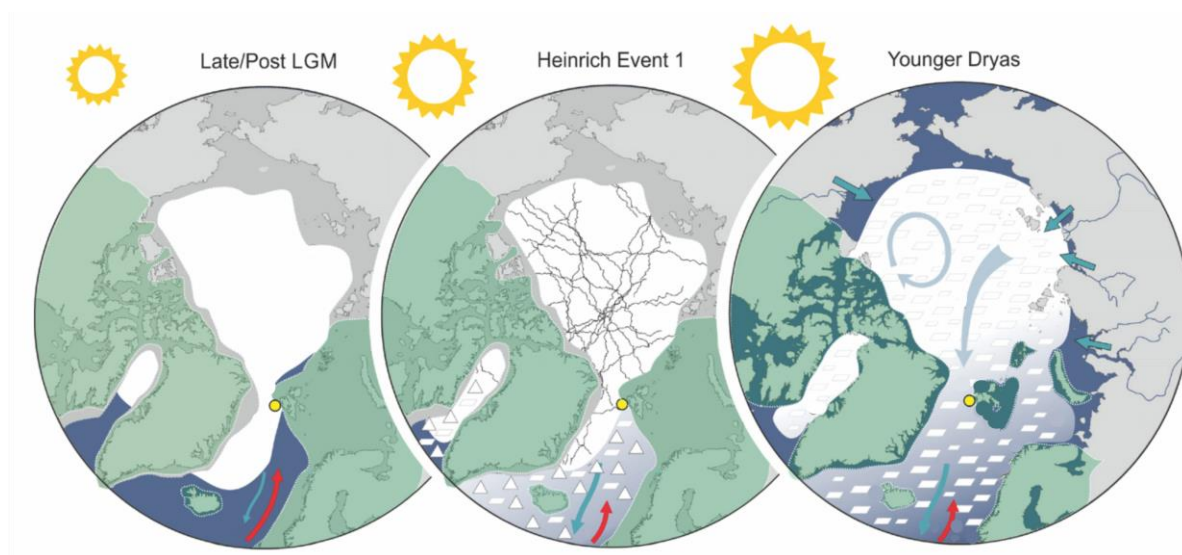
Figure 45: Evolution of the sea ice in Fram Strait and the Arctic Ocean from the late part of Last Glacial Maximum to Younger Dryas. The late Last Glacial Maximum contained permanent stationary sea ice. During Heinrich event 1 the sea ice started breaking up and Younger Dryas had further transportation of sea ice due to a warming climate. Areas in dark gray represent the corresponding sea level through time. The yellow circle represents the location of the HH16-549 core. Modified from (Müller & Stein, 2014).

HH16-549GC records higher concentration of calcium carbonate during Heinrich event 1 (Figure 38), which is typical for all Heinrich events recorded in this core as proposed by Hemming (2004). Higher content of calcium carbonate and increasing concentration of planktic foraminifera may indicate increased planktic productivity (Müller & Stein, 2014; Chauhan, et al., 2016). Figure 38 reveals that the concentration of calcium carbonate more or less follows the same trends as the content of total carbon throughout the core. Zamelczyk et al (2014) suggest that this is linked to increased rain ratio of calcium carbonate may lead to increased respirative release of carbon dioxide which might cause dissolution of calcium carbonate even in surface sediments with high content of carbonate. Low concentration of calcium carbonate and high content of total organic carbon at 232 cm (≈17,200 cal years BP) is suggested to indicate Arctic surface water and seasonal sea ice (Zamelczyk, et al., 2014).

A small assemblage of bivalve shells is found at 235 cm (≈17,400 cal years BP) (Figure 33) in HH16-549GC, which possibly could be correlated to a study from Sztybor & Rasmussen (2016) revealing a large colony of Vesicomyid clams dated to be 16,385 cal years BP. The occurrence of these shells has been interpreted to be an indication of plentiful supply of sulfide-rich fluids in the sediments (Sztybor & Rasmussen, 2016).

5.2.3 Marine Isotope Stage 1 (14,000-7500 cal years BP)

5.2.3.1 Bølling-Allerød interstadial and Younger Dryas (15,600-11,700 cal years BP)

Bølling-Allerød interstadial and Younger Dryas starts at the end of Heinrich event 1 (15,600 cal years BP) and finish at the transition from Marine Isotope Stage 2 to Marine Isotope Stage 1 (11,700 cal years BP). The Younger Dryas is suggested to occur from 12,600 to 11,700 cal years BP (Slubowska-Woldengen, et al., 2007).

The transition from Heinrich event 1 to Bølling-Allerød interstadials in the western Svalbard region is characterized as a period with warmer temperatures, increased sedimentation rates and higher concentration of IRD (Figure 36). Further melting of ice and more calving of icebergs caused the ice to retreat to the mouth of Kongsfjorden and Isfjorden (Elverhøi, et al., 1995; Andersen, et al., 1996; Nørgaard-Pedersen, et al., 2003). Elverhøi et al (1995) suggest that further deglaciation occurred shortly after 15,000 cal years BP. Mangerud et al (1998) propose that the continental shelves in the Svalbard region were completely ice-free from approximately 15,000 cal years BP.

The study from Jessen et al (2010) suggest that laminated layers were deposited around 14,850 cal years BP, and is proposed to occur as a result of rapid sedimentation from turbid meltwater as the Svalbard-Barents Sea Ice Sheets retreated (Elverhøi, et al., 1995; Rasmussen, et al., 2007). This feature is observed is interpreted to occur from 134 cm to 200 cm in HH16-549GC (Figure 34). Fine-grained laminated mud was deposited around 14,650 cal years BP with higher sedimentation rates than during the Last Glacial Maximum (Elverhøi, et al., 1995; Birgel & Hass, 2004; Rasmussen, et al., 2007). Figure 36 shows that all fractions decreased significantly in this section except for the mud (<63 µm) fraction, which might signify the absence of sea ice and icebergs. Elverhøi et al (1995) propose that the deposition may have been constrained due to a strong coastal current containing icebergs adjacent to the shelf edge.

It is also likely that the upper part of the slope endured intensive iceberg rafting in this period (Elverhøi, et al., 1995). The laminated layers recorded in this section may indicate swift glacial retreat in the Barents Sea, which can be correlated to the melting of ice sheets in the Irish Sea and the southern Fennoscandian region (Lekens, et al., 2005). Increased influence of Atlantic subsurface water and higher insolation from the sun (Figure 43) is likely to cause melting and calving of ice in this period. Jessen et al (2010) suggest that the laminated layers were probably deposited as a large outburst of meltwater.

The stacked magnetic susceptibility from the western Svalbard region (figure 27) reveals a generally lower magnetic susceptibility through the Bølling-Allerød period and especially within the laminated sediments, which is suggest that this significant drop in magnetic susceptibility occurred due to increased meltwater deposits in this period (Jessen, et al., 2010). The magnetic susceptibility in HH16-549GC (Figure 36) does however not record a remarkable drop during this event, it is however likely that the magnetic susceptibility has been disturbed due to it being retrieved from within a pockmark as discussed earlier in chapter 4: Correlation and age model establishment.

Both planktic and benthic $\delta^{18}O$ records increasing values in the shift from Heinrich event 1 and the Bølling/Allerød interstadials (Figure 37), which might be another indication of calving icebergs and meltwater influencing the surface water (Jessen, et al., 2010). A study from Elverhøi et al (1995) reveals that the high values of $\delta^{18}O$ occurring at around 15,000 cal years BP may be linked with the development of meltwater occurring simultaneously with the retreat of the Svalbard-Barents Sea Ice Sheets from the western shelf of Isfjorden. Rasmussen et al (2007) suggest that increasing values of $\delta^{18}O$ may imply reduced bottom water temperatures. the $\delta^{18}O$ values is declining from around 178 cm (≈14,900 cal years BP) in HH16-549GC until the end of the Bølling-Allerød interstadial and Younger Dryas period. Slubowska-Woldengen et al (2007) reports of reduced planktic and benthic $\delta^{18}O$ from 13,400 cal years BP and is suggested to occur as a result of reduced salinity in the water masses and freshening of the bottom waters due to a shift in dominant water masses. Lower salinity in the water masses is also indicated by a significant depletion of both planktic and benthic foraminifera (Figure 36) and is suggested to occur as a consequence of extensive melting of icebergs and sea ice (Spielhagen & Erlenkeuser, 1994). Fluctuating values of $\delta^{18}O$ is may imply increased inflow of Atlantic water (Birgel & Hass, 2004; Müller & Stein, 2014).

Although the inflow of Atlantic Water was strong in this period, it is suggested that the flow did not reach the western Svalbard shelf due to the flow being submerged under the cold meltwater (Slubowska, et al., 2005). Slubowska-Woldengen et al (2007) propose that the surface waters was covered by seasonal sea ice during from 14,500 cal years BP to 12,600 cal years BP. The bottom water in the Younger Dryas is likely to be colder and be less saline (Slubowska-Woldengen, et al., 2007). Figure 46 illustrates a reconstruction of the environment in the western Svalbard during the Bølling period.

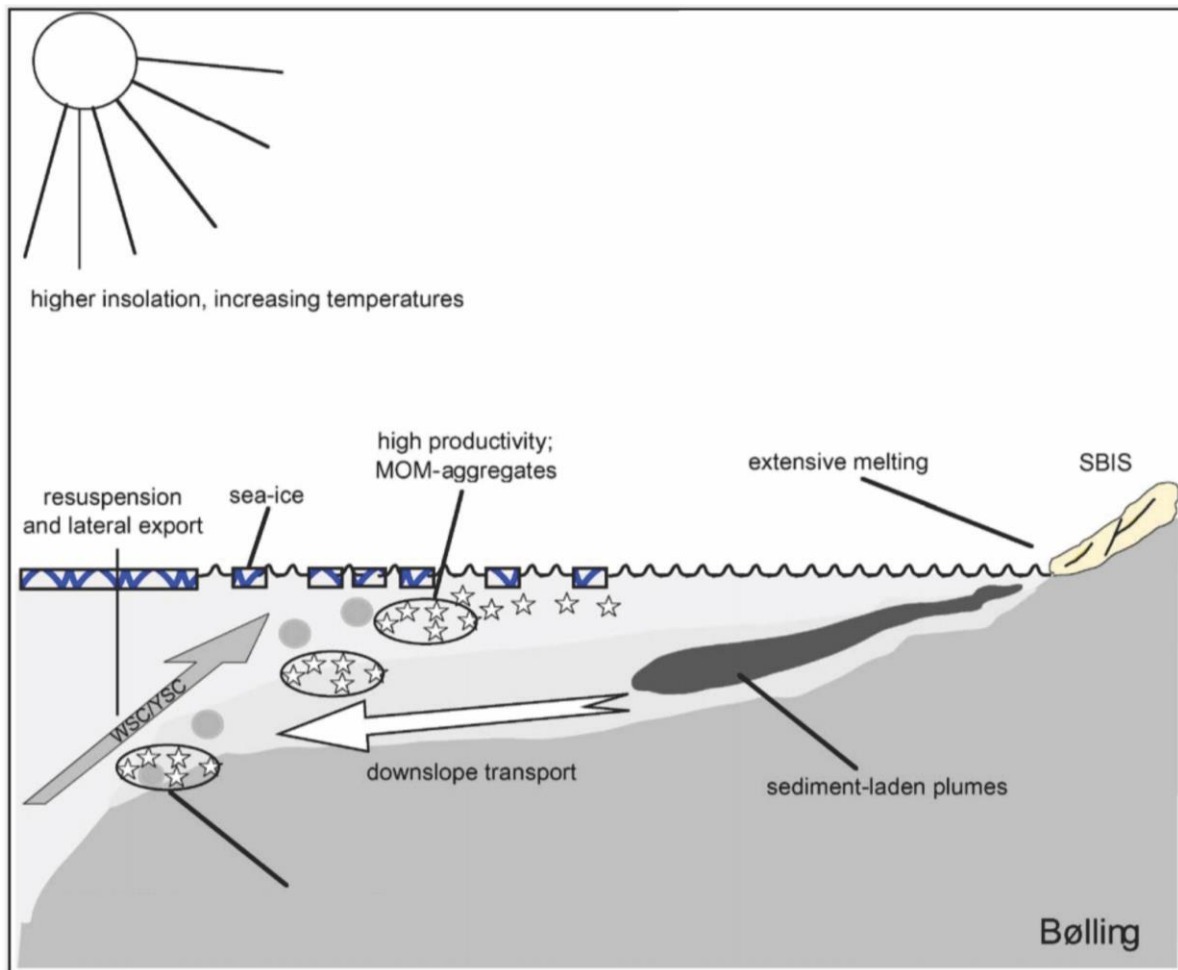*Figure 46: Illustration of environment and processes occurring in the western Svalbard slope and western Yermak slope in the Bølling period. Strong sediment resuspension-loop in the bottom waters discharge substantial amounts of inorganic or organic matter in the West Spitsbergen current (WSC) and Yermak slope current (YSC) from the Svalbard-Barents Sea Ice Sheets (SBIS). Modified from Birgel & Hass (2004).*

There is a significant depletion in both planktic and benthic $\delta^{13}C$ values in the laminated sediments (Figure 37). Aagaard-Sørensen et al (2014) proposes that these values might indicate stratification in the water column due to meltwater and sea ice. Low content of calcium carbonate and high concentration of total organic carbon occurs within the laminated sediments (Figure 38) is suggested to indicate Arctic surface water and seasonal sea ice (Zamelczyk, et al., 2014). Low concentration of $CaCO_3$ may imply polar conditions with low productivity triggered by increased influence of meltwater (Aagaard-Sørensen, et al., 2014) The highest concentration of total organic carbon in HH16-549GC is found in the Bølling-Allerød interstadials (Figure 38) and might be linked with higher concentration of methane in this period (Figure 47) (Bluiner & Brook, 2001; Birgel & Hass, 2004). This theory will be further discussed in chapter 5.3 Gas seepage.

5.2.3.2 Holocene (11,700 cal years BP - Recent)
The start of the Holocene period is suggested to start when the deglaciation of Spitsbergenbanken finished at 11,700 cal years BP (Elverhøi, et al., 1995; Andersen, et al., 1996; Mangerud, et al., 1998). The early Holocene is characterized as a period with ameliorated climatic conditions with sea surface temperatures estimated to be 4° higher than today (Slubowska-Woldengen, et al., 2007). High concentration of IRD is observed from the start of the Holocene period until 37 cm (≈10,500 cal years BP) in HH16-549GC. Melting of ice sheets and further release of meltwater caused further delay of the inflow of Atlantic surface water and Holocene warming in comparison to areas located further south (Jessen, et al., 2010). Slubowska et al (2005) propose that increased abundance of IRD in northern and western Svalbard up to 10,100 cal years BP. From 10,100 cal years BP and onwards the fjords of Svalbard were probably deglaciated (Svendsen & Mangerud, 1997; Jessen, et al., 2010) and is evident as the concentration of IRD in HH16-549GC is significantly low in this period (Figure 36). Jessen et al (2010) propose that the western Svalbard region contained few or any icebergs in the period from 10,100 to 7600 cal years BP. The top of the HH16-549GC core is assumed to be aged 7500 cal years BP due to a rapid increase of IRD towards the very end of the core (Figure 36) which coincides with observations from Jessen et al (2010). Figure 36 reveals a rapid increase of magnetic susceptibility from 30 cm (≈10,500 cal years BP) towards the end of the core. This observation is likely to coincide with the stacked magnetic susceptibility from western Svalbard in the study from Jessen et al (2010) which reveals higher values of magnetic susceptibility from 9920 cal years BP to 8170 cal years BP.

Figure 36 reveals that there is an increasing concentration of planktic foraminifera at the onset to the Holocene period, which might imply strong advection of the Atlantic Water (Slubowska-Woldengen, et al., 2007). From 10,800 cal years BP to 6800 cal years BP the Atlantic water flow in northern and western Svalbard is reported to be strong. The warming trend in the early Holocene is likely to be caused by increased insolation from the sun (Figure 43), increased flux of Atlantic water due to strengthened thermohaline circulation and increased wind force in the western Svalbard shelf (Slubowska-Woldengen, et al., 2007). The value of planktic and benthic $\delta^{18}O$ decreases rapidly in this period (Figure 37), which is characteristic for the early Holocene. High values of $\delta^{13}C$ is observed throughout the Holocene (Figure 37), which is interpreted to indicate good ventilation of the surface waters (Spielhagen & Erlenkeuser, 1994).

A small assemblage of diatoms is found at 27 cm ($\approx$ 9800 cal years BP) in the 63-100 µm fraction in HH16-549GC, which might correlate with the study from Jessen et al (2010) reporting of diatom-rich layers observed in several cores from western Svalbard from around 10,100 to 9840 cal years BP. This event is linked with the Polar Front being pushed further north and increased inflow of Atlantic surface water in this period (Stabell, 1986). The assemblage of diatoms in HH16-549GC is however limited which makes the assumption uncertain.

5.3 Gas seepage

The early Holocene and Bølling-Allerød interstadials are periods identified with higher concentrations of methane in the atmosphere (Figure 47) (Andersen, et al., 2004; Brook, et al., 2000). Figure 38 reveals a significant increase in the concentration of total organic carbon in the middle of Heinrich event 1 to Bølling-Allerød interstadial (≈17,700 to 14,300 cal years BP), Heinrich event 2 (≈24,000 cal years BP), Heinrich event 3 (30,500 cal years BP) and at 360 cm (≈ 26,300 cal years BP) (Figure 38) where a thick bivalve shell layer is found in HH16-449GC. (Figure 33). High content of total organic carbon is linked with high productivity of methane through microbial activity (Kvenvolden, 2002; Sztybor, 2016). The Bølling-Allerød interstadials record high concentration of total organic carbon (Figure 38) and higher sedimentation rates (Figure 36). The sea level is predicted to increase rapidly in this period, which could indicate a connection with climatic changes and occurrence of methane in the North Atlantic (Peltier & Fairbanks, 2006). Sztybor (2016) suggest this event is linked with lower anaerobic oxidation of methane reducing the capacity of the microbial filter in highly organic sediments. Figure 47 illustrates methane levels recorded from ice cores from Greenland and Antarctica.
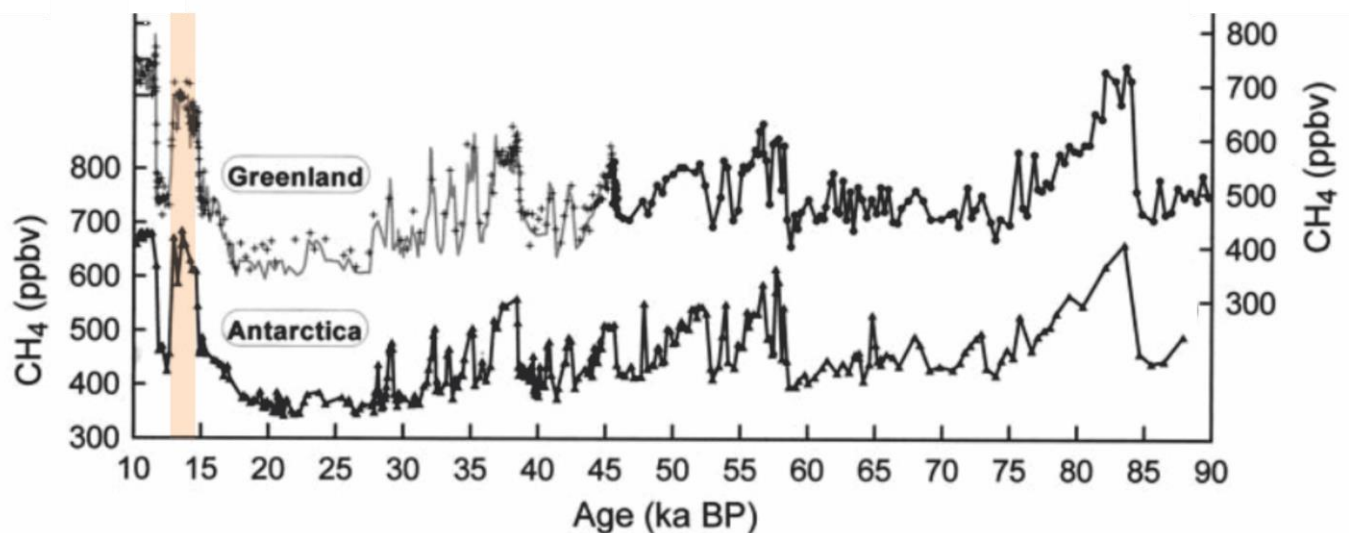

Figure 47: Methane levels from Greenland and Antarctica ice cores. The brown line highlights a significant increase in methane levels occurring around 14,000 cal years BP. Modified from (Bluiner & Brook, 2001).

The exchange of carbon dioxide between the ocean and the atmosphere is significantly inhibited by sea-ice cover, which might have led to accumulation of metabolic carbon dioxide from residual bacterial respiration with low $\delta^{13}C$ values (Spielhagen & Erlenkeuser, 1994). The retreat of ice sheets leads to a reduction in pressure on the seafloor which may result in further dissociation from gas hydrates (Smith, et al., 2001).

Enhanced seep activity can also be revealed by significant depletion in $\delta^{13}C$ values (Hill, et al., 2012; Consolaro, et al., 2015; Sztybor, 2016). HH16-549GC records low values of benthic $\delta^{13}C$ in the start of the laminated deposits ($\approx$15,000 cal years BP) and at 365 cm ($\approx$ 26,500 cal years BP), where a thick layer of bivalve shells are observed in HH16-549GC (Figure 33). The $\delta^{13}C$ value of foraminifera shells are significantly lower if they are exposed to methane (Hill, et al., 2012). Low values of both planktic and benthic $\delta^{13}C$ is likely to be recorded as a consequence of diagenetic overprint caused by authigenic carbonates related to the anaerobic oxidation of methane occurring at the sulfate-methane transition zone (Cook, et al., 2011). A study from Sztybor & Rasmussen (2016) proposes that low values of $\delta^{13}C$ at the end of Heinrich event 1 with peaking intensity during the Bølling-Allerød interstadials is an indication of increased seep activity that started at the end of Heinrich event 1 when the intermediate water started heating up (Consolaro, et al., 2015; Sztybor & Rasmussen, 2016). Enhanced bottom water temperatures through Heinrich event 1 may have caused more intense flux of methane at the start of Bølling-Allerød interstadials (Sztybor & Rasmussen, 2016). Consolaro et al (2015) implies that the increasing methane flux in Vestnesa Ridge in this period could be caused by increased seismic activity due to swift melting of ice sheets in the Svalbard region. The low values of $\delta^{13}C$ within the laminated deposits correlates with the sulfate-methane transition zone which is located at 185 cm in HH16-549GC (Figure 25). Figure 48 reveals that the sulfate-methane interface correlates with significantly low values of $\delta^{13}C$ in a study from Ussler III & Paul (2008).
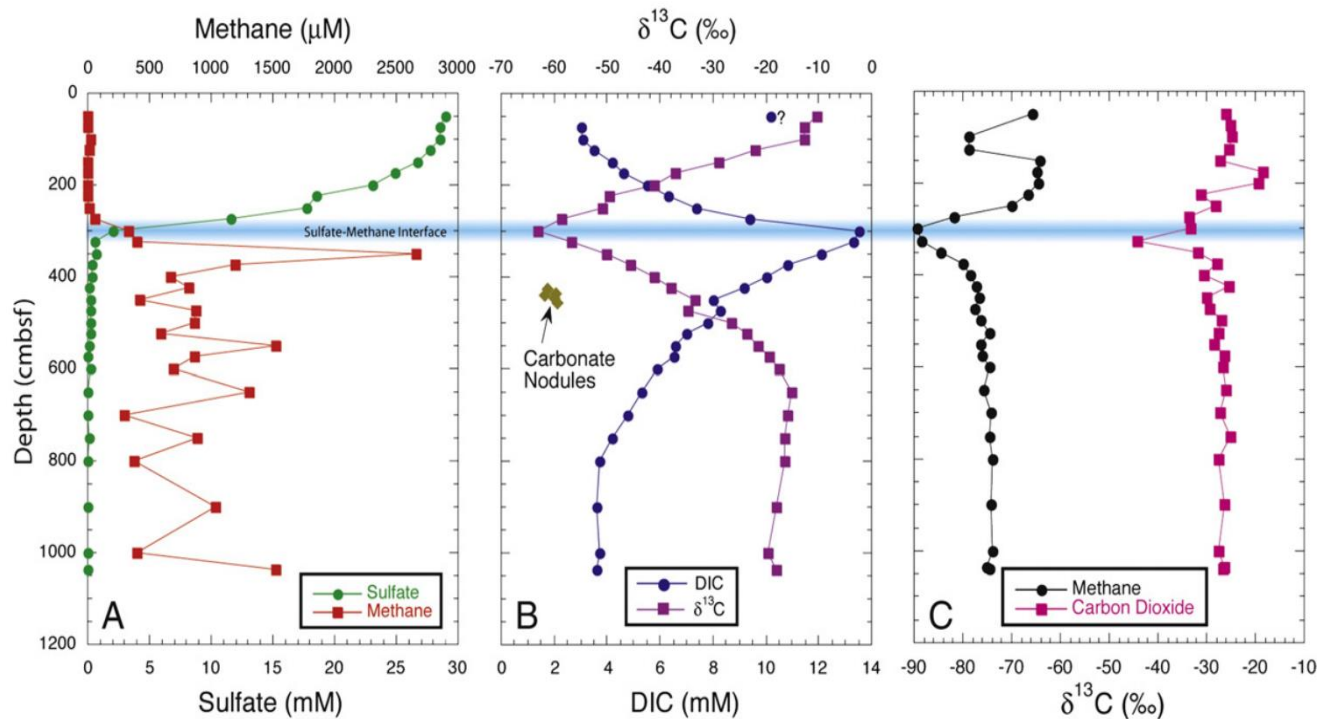
Figure 48: Correlation of $\delta^{13}C$ with the sulfate-methane transition zone in a study from (Ussler III & Paull, 2008).

The sulfate-methane transition zone is normally restricted to a few centimeters and is likely to record a sudden drop in both planktic and benthic $\delta^{13}C$ (Treude, et al., 2005). The depth of the sulfate-methane transition zone is controlled by the strength of upward methane flux (Figure 49) (Consolaro, et al., 2015). Figure 49 illustrates how the sulfate-methane transition zone is controlled by the flux of methane and the predicted environment where the sulfate-methane transition zone is located in HH16-549GC (≈14,900 cal years BP).
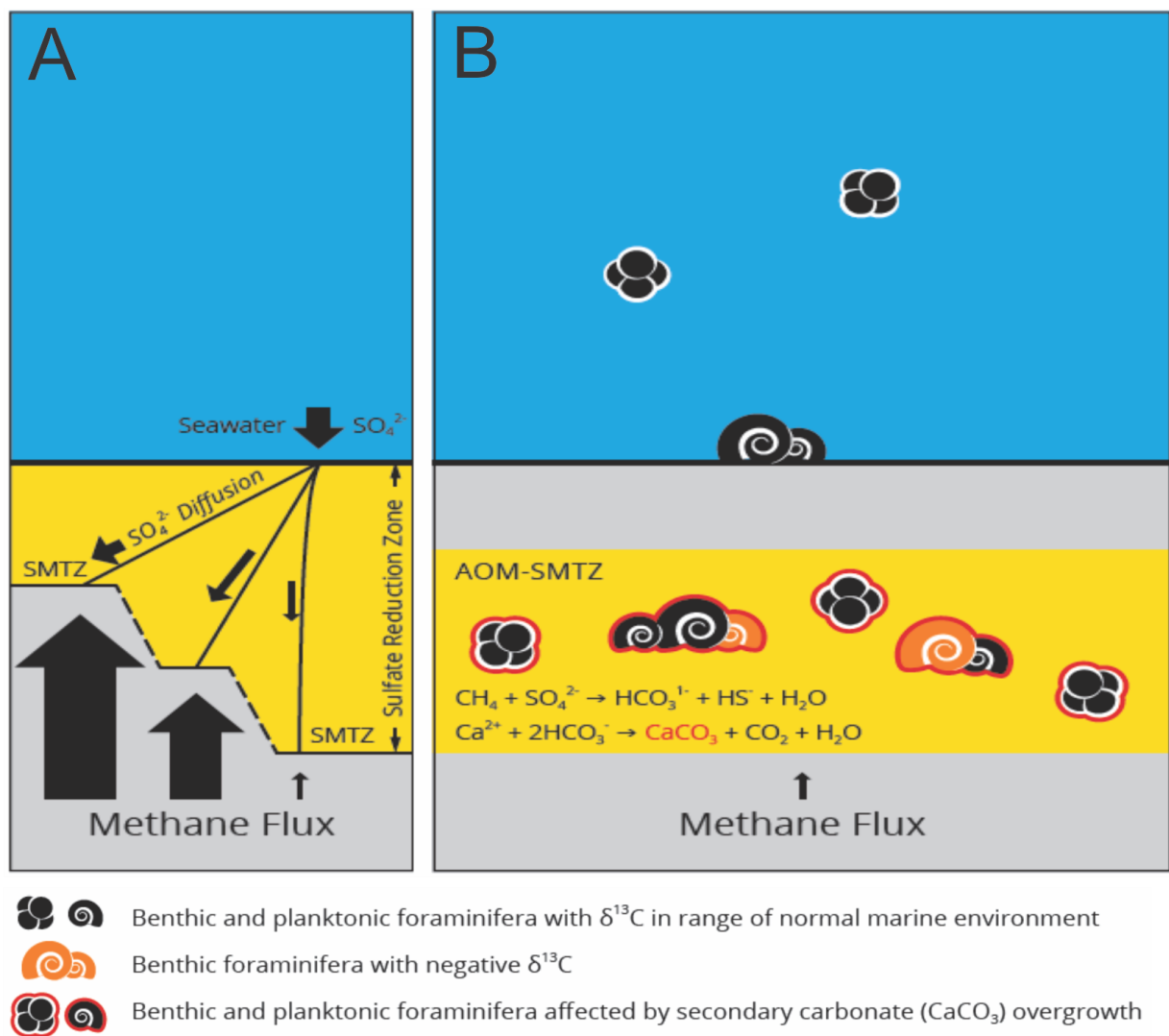
*Figure 49: **A:** Illustration of how the sulfate-methane transition zone is controlled by the flux of methane if sulfate from the seawater is fixed. Modified from (Borowski, et al., 1996). **B:** Illustration of the predicted environment from when both planktic and benthic $\delta^{13}C$ recorded largely negative values (≈14,900 cal years BP in HH16-549GC).*

Low $\delta^{13}C$ values of benthic foraminifera are mainly caused by primary and diagenetic calcite (Cook, et al., 2011; Consolaro, et al., 2015) and occurs as it incorporates the dissolved inorganic carbon in pore waters and register the existence of anaerobically oxidized methane in the sediments as the shells goes through mineralization (Hill, et al., 2012). It is important to determine the position of the sulfate-methane transition zone as authigenic carbonate starts to precipitate in that zone. Planktic $\delta^{13}C$ records a similar negative trend but in a slightly less magnitude (Figure 37). Planktic foraminifera can produce low $\delta^{13}C$ values since their porous and spiny surface has a bigger potential for growth of authigenic carbonate in comparison to benthic foraminifera, which has a smoother test (Cook, et al., 2011).

Planktic $\delta^{13}C$ should normally not be affected by methane in the water column due to the methane being consumed at the seafloor by methanotrophic bacteria (Reeburgh, 2007). It is therefore likely that the negative values are caused by diagenetic adjustment from methane-derived authigenic carbonates occurring in the tests of the foraminifera subsequently to deposition (Panieri, et al., 2009). These deviations may occur due to secondary carbonate precipitation after the foraminifera were buried (Consolaro, et al., 2015). Secondary overgrowths through anaerobic oxidation of methane may be deposited in times of high flux of methane and in areas close to the sulfate-methane transition zone, when the flux of methane are not strong enough to pass through the microbial oxidation filter and enter the sediment-water interface (Panieri, et al., 2016). Borowski et al (1996) suggest that the precipitation of authigenic carbonate develops when the methane is oxidized by the process of anaerobic oxidation of methane in the sulfate-methane transition zone and when there is a low flux of methane.

The highlighted zones in Figure 50 represent periods in HH16-549GC that has been interpreted to indicate enhanced seepage. These zones contains high content of total organic carbon and low $\delta^{13}C$ values, which is likely to reveal events of methane seepage (Kvenvolden, 2002; Hill, et al., 2012; Sztybor, 2016). Methane seepage is likely to be triggered by seismic activity, changing sea level, larger sedimentation rate and higher bottom water temperatures, which may cause landslides as a result of alteration in pore pressure in the sub-seafloor triggering gas venting from the seabed in the study area (Owen, et al., 2007; Hill, et al., 2012). The first seep event is proposed to be centered at 14,900 cal years BP in the early stages of the Bølling-Allerød interstadials which is supported in studies by Consolaro et al (2015) and Sztybor (2016) from the same region. The second zone is centered at 26,200 cal years BP and correlates with a thick layers of bivalve shells in the sediments (Figure 33). This theory is supported by declining sea level in this period (Peltier & Fairbanks, 2006) and warmer bottom water temperatures revealed by a short interval of low $\delta^{18}O$ (Figure 37) (Rasmussen, et al., 2007; Chauhan, et al., 2014). The study from Sztybor & Rasmussen (2017) also reveals negative values of $\delta^{13}C$ in this period, which might occur as a result of diagenetic changes of the empty shells located in sediments.
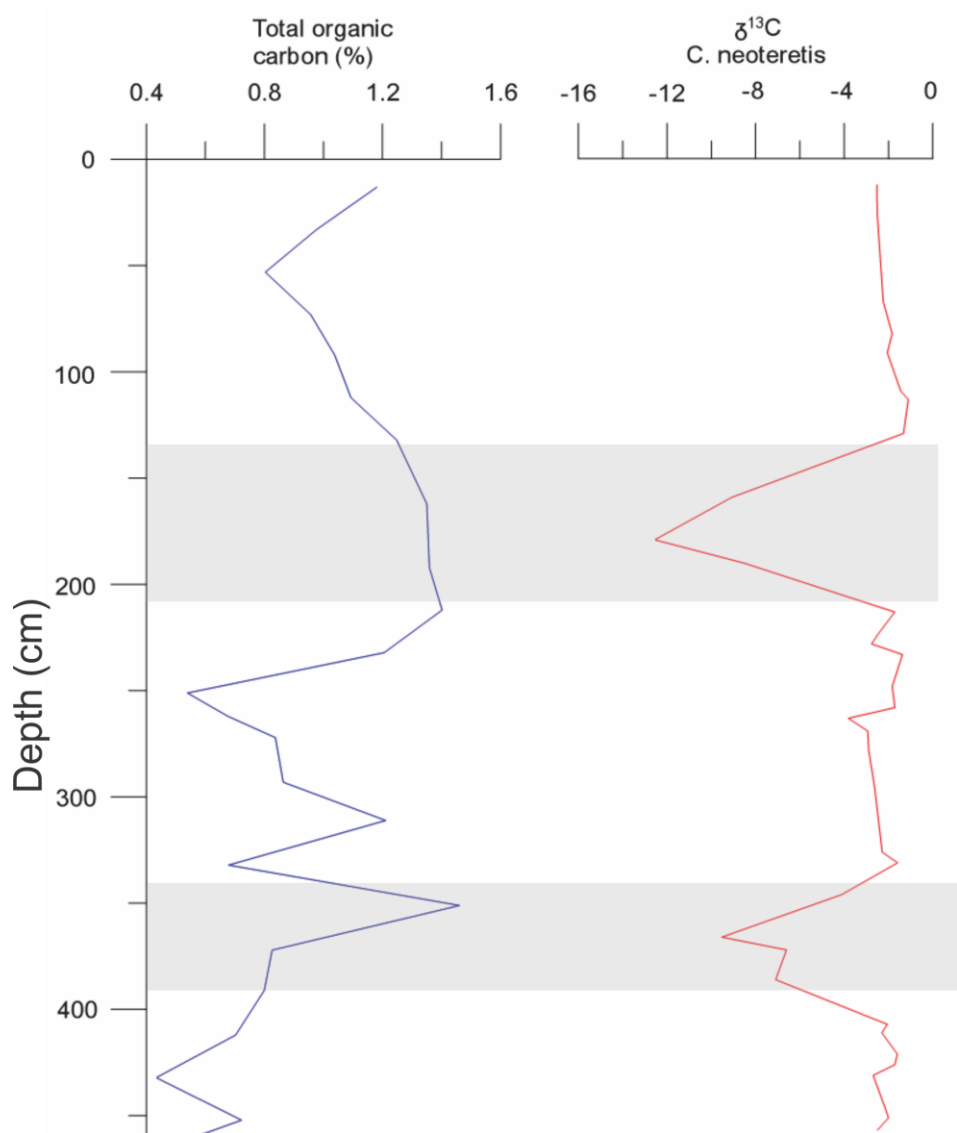
Figure 50: The highlighted areas reveals zone with high content of total organic carbon and low $\delta^{13}C$ values which is interpreted to reveal events of methane seepage in HH16-549GC.

6 Summary and conclusion

The sediment core HH16-549GC retrieved from within a pockmark at Vestnesa Ridge in the Fram Strait, western Svalbard has been investigated to reconstruct changes in paleoceanographic and paleoclimatic conditions from 31,000 to 7500 cal years BP. Vestnesa Ridge is located in an area with extensive methane seepage from the ocean floor and it is therefore particularly interesting to study the interaction between release of methane correlated with climatic changes throughout time.

- Three Marine Isotope Stages has been distinguished in HH16-549GC by investigating variations in $\delta^{18}O$. Marine Isotope Stage 2 is characterized with high $\delta^{18}O$ values and occurs from 29,000 to 14,000 cal years BP. Marine Isotope Stage 3 and 1 is revealed by decreasing values of $\delta^{18}O$ from 31,000 to 29,000 cal years BP and from 14,000 to 7500 cal years BP in the core, respectively.

- A laminated layer and a mass transfer deposit are two distinctive events recorded in HH16-549GC that has been correlated with the study from Jessen et al (2010). The laminated sediments consist of fine-grained sediments deposited by meltwater plumes from 15,070 to 14,600 cal years BP causing rapid sedimentation as the Svalbard-Barents Sea Ice Sheets retreated. The mass transport deposit is interpreted to occur as the ice approached the shelf edge in western Svalbard. The stacked magnetic susceptibility by Jessen et al (2010) reveals a significant drop during these events. This is however not recorded in HH16-549GC and may be caused by the dissolution of magnetic minerals as the core is retrieved from methane seep sediments.

- Two major events of possible methane seepages characterized by high content of total organic carbon and significantly low $\delta^{13}C$ values are centered at 14,900 and 26,200 cal years BP (-12,53‰ and -9,50‰) in HH16-549GC. The seep event at 14,900 cal years BP occurs in the early stages of the Bølling-Allerød interstadials. A thick layer of bivalve shells date approximately 26,300 cal years BP and might possibly indicate enhanced seepage of methane. Methane seepage is likely to be triggered by seismic activity, changing sea level and higher bottom water temperatures. Common for both seep events indicated in this study is that sea level changed drastically during the events and increased bottom water temperature is revealed by low $\delta^{18}O$ values in both periods.

7 References

Aagaard, K., Foldvik, A. & Hillman, S. R., 1987. The West Spitsbergen Current: disposition and water mass transformation. *J. Geophys. Res. 92,* pp. 3778-3784.

Aagaard, K., Swift, J. H. & Carmack, E. C., 1985. Thermohaline circulation in the Arctic Mediterranean Seas. *J. Geophys. Res. 90,* pp. 4833-4846.

Aagaard-Sørensen, S. et al., 2014. A Late Glacial–Early Holocene multiproxy record from the eastern Fram Strait, Polar North Atlantic. *Marine Geology,* Volum 355, pp. 15-26.

Andersen, E. et al., 1996. Late Quaternary sedimentation and glacial history of the Western Svalbard continental margin. *Marine Geology 133.*

Andersen, K. K. et al., 2004. High-resolution record of Northern Hemisphere climate extending into the last interglacial period. *Nature 431,* pp. 147-151.

Archer, D., 2007. Methane hydrate stability and anthropogenic climate change. *Biogeosciences, 4,* pp. 521-544.

Armstrong, H. & Braiser, M., 2005. Microfossils. I: *Microfossils, second edition.* s.l.:s.n.

Arntsen, B., Wensaas, L., Loseth, H. & Hermanrud, C., 2007. Seismic modeling of gas chimneys. *Geophysics 72,* pp. 251-259.

Barnes, R. O. & Goldberg, E. D., 1976. Methane production and consumption in anoxic marine sediments. *Geology 4,* pp. 297-300.

Bauch, H. A. et al., 2001. A multiproxy reconstruction of the evolution of deep and surface waters in the subarctic Nordic seas over the last 30,000 yr. *Quaternary Science Reviews,* Volum 20, pp. 659-678.

Berndt, C. et al., 2014. Temporal Constraints on Hydrate-Controlled Methane Seepage off Svalbard. *Sciencemag Vol 343.*

Bhatnagar, G. et al., 2011. Analytical theory relating the depth of the sulfate-methane transition to gas hydrate distribution and saturation. *Geochemistry, Geophysics, Geosystems 12.*

Biastoch, A. et al., 2011. Rising Arctic Ocean temperatures cause gas hydrate destabilization and ocean acidification. *Geophys. Res. Lett 38.*

Birgel, D. & Hass, H., 2004. Ocean and Atmospheric variations during the last deglaciation in the Fram Strait (Arctic Ocean): a coupled high-resolution organic-geochemical and sedimentological study. *Quaternary Science Reviews 23,* pp. 29-47.

Bluiner, T. & Brook, E. D., 2001. Timing of Millennial-Scale Climate Change in Antarctica and Greenland During the Last Glacial Period. *Sciencemag,* Volum 291, pp. 109-112.

Boetius, A. et al., 2000. A marine microbial consortium apparently mediating anaerobic oxidation of methane. *Nature 407,* pp. 623-626.

Boetius, A. & Wenzhofer, F., 2013. Seafloor oxygen consumption fuelled by methane from cold seeps. *Nat Geosci 6,* pp. 725-734.

Bond, G. et al., 1993. Correlations between climate records from North Atlantic sediments and Greenland ice. *Nature,* Volum 365, pp. 143-147.

Borowski, W. S., Paull, C. K. & Ussler, W., 1996. Marine pore-water sulfate profiles indicate in situ methane flux from underlying gashydrate. *Geology 24,* pp. 655-658.

Bourke, R. H., Wiegel, A. M. & G., P. R., 1988. The westward turning branch of the West Spitsbergen Current. *Jorunal of Geophysical Research,* Volum 93, pp. 14065-14077.

Bradley, R., 2015. *Paleoclimatology: Reconstructing Climates of the Quaternary.* Third edition red. Amherst, Massachusetts, : Elsevier.

Broecker, W. S., Peteet, D. M. & Rind, D., 1985. Does the ocean-atmosphere system have more than one stable mode of operation?. *Nature,* Volum 315, pp. 21-26.

Brook, E. J. et al., 2000. On the origin and timing of rapid changes in atmospheric methane during the last glacial period. *Global Biogeochem. Cy. 14,* pp. 559-572.

Bunz, S. et al., 2012. Active gas venting trough hydrate-bearing sediments on the Vestnesa Ridge, offshore W-Svalbard. *Marine Geology 332–334,* pp. 189-197.

Bylinskaya, M. E. et al., 2016. Paleoenvironments in the Fram Strait during Marine Isotope Stages 2-6 based on planktonic paleobiological and stable-isotope proxies and ice-rafted debris. *Quaternary International,* Volum 420, pp. 272-279.

Caralp, M. H., 1989. Size and morphology of the benthic foraminifer Melonis barleeanum: Relationships with marine organic matter. *Journal of Foraminiferal Research,* 19(3), pp. 235-245.

Castellini, D. G., Dickens, G. R., Snyder, G. T. & Rupple, C. D., 2006. Barium cycling in shallow sediment above active mud volcanoes in the Gulf of Mexico. *Chem. Geol., 226,* pp. 1-30.

Chand, S. & Minshull, T. A., 2003. Seismic constraints on the effects of gas hydrate on sediment physical properties and fluid flow: a review.

Chauhan, T., Noormets, R. & Rasmussen, T. L., 2016. Glaciomarine sedimentation and bottom current activity on the north-western and northern continental margins of Svalbard during the late Quaternary. *Geo-Mar Lett,* Volum 36, pp. 81-99.

Chauhan, T. et al., 2014. Glacial history and paleoceanography of the southern Yermak Plateau. *Quaternary Science Reviews,* Volum 92, pp. 155-169.

Consolaro, C. et al., 2015. Carbon isotope(δ13C) excursions suggest times of major methane release during the last 14 kyr in Fram Strait, the deep-water gateway to the Arctic. *Climate of the Past.*

Cook, M. S., Keigwin, L. D., Birgel, D. & Hinrichs, K. U., 2011. Repeated pulses of vertical methane flux recorded in glacial sediments from the southeast Bering Sea. *Paleoceanography,* Volum 26, p. PA2210.

Darling, K. F., Kucera, M., Kroon, D. & Wade, C. M., 2006. A resolution for the coiling direction paradox in Neogloboquadrina pachyderma. *Paleoceanography,* Volum 21.

Darling, K. F., Kucera, M., Pudsey, C. J. & Wade, C. M., 2004. Molecular evidence links cryptic diversifiaction in polar plankton to Quaternary climate dynamics. *Proc. Natl. Acad. Sci. U.S.A.,* Volum 101, pp. 7657-7662.

Demirbas, A., 2010. *Methane Gas Hydrate.* London: Springer London Dordrecht Heidelberg New York.

Desa, E., 2001. Submarine Methane Hydrates - Potential Fuel Resource of the 21st Century. *Proc, of AP Akademi of Sciences,* 5(2), pp. 101-114.

Dickens, G. R., 2003. Rethinking the global carbon cycle with large, dynamic and microbially mediated gas hydrate capacitor. *Earth and Planetary Science Letters,* Volum 213, pp. 169-183.

Dickson, R. R. et al., 2000. The Arctic Ocean response to the North Atlantic oscillation. *Journal of Climate 13,* pp. 2671-2696.

Dowdeswell, J. A. & Elverhøi, A., 2002. The timing of initiation of fast-flowing ice streams during a glacial cycle inferred from glacimarine sedimentation. *Marine Geology,* Volum 188, pp. 3-14.

Elverhøi, A. et al., 1995. The growth and decay of the Late Weichselian Ice Sheet in western Svalbard and adjacent areas based on provenance studies of marine sediments. *Quaternary Research 44.*

Elverhøi, A. et al., 2002. Submarine mass-wasting on glacially-influenced continental slopes: processes and dynamics. *Geological Society of London,* Volum 203, pp. 73-83.

Elverhøi, A., Hooke, R. & Solheim, A., 1998. Late Cenozoic erosion and sediment yield from the Svalbard-Barents Sea region: implications for understanding erosion of glacierized basins. *Quaternary Science Reviews,* Volum 17, pp. 209-241.

Elverhøi, A. et al., 1997. On the origin and flow behaviour of submarine slides on deep-sea fans along the Norwegian-Barents Sea continental margin. *Geo-Marine Letters,* Volum 17, pp. 119-125.

Faleide, J. A. et al., 1996. Late Cenozioc evolution of the western Barents Sea-Svalbard continental margin. *Global and Planetary Change 12,* pp. 53-74.

Ferré, B., Mienert, J. & Faseker, T., 2012. Ocean temperature variability for the past 60 years on the Norwegian-Svalbard margin influences gashydrate stability on human time scales. *Journal of Geophysical Research Vol 117.*

Gentz, T. et al., 2013. A water column study of methane around gas flares located at the West Spitsbergen continental margin. *Continental Shelf Research 72,* pp. 107-118.

Gildor, H. & Tziperman, E., 2001. A sea ice climate switch mechanism for the 100-kyr glacial cycles. *Journal of Geophysical Research 106 (C5),* pp. 9117-9136.

Goswani, B. K. et al., 2015. A joint electromagnetic and seismic study of an active pockmark within the hydrate stability field at the Vestnesa Ridge, West Svalbard. *J. Geophys. Res. Solid Earth 120,* pp. 6797-6822.

Graves, C. A. et al., 2017. Methane in shallow subsurface sediments at the landward limit of the gas hydrate stability zone offshore western Svalbard. *Geochemica et Cosmochimica Acta,* Volum 198, pp. 419-438.

Grousset, F. et al., 1993. Patterns of ice-rafted detritus in the glacial North Atlantic (40-55 N). *Paleocenography.*

Gwiazda, R. H., Hemming, S. R. & Broecker, W. S., 1996. Provenance of icebergs during Heinrich event 3 and the contrast to their sources during other Heinrich episodes. *Paleoceanography,* 11(4), pp. 371-378.

Hald, M. & Aspeli, R., 1997. Rapid climatic shifts of the northern Norwegian Sea during the last deglaciation and the Holocene. *Boreas,* Volum 26, pp. 15-28.

Hald, M., Dokken, T. & Mikalsen, G., 2001. Abrupt climatic change during the last interglacia-glacial cycle in the polar North Atlantic. *Marine Geology,* Volum 176, pp. 121-137.

Hebbeln, D. et al., 1994. Moisture supply for northern ice-sheet growth during the Last Glacial Maximum. *Nature,* Volum 370, pp. 409-411.

Hebbeln, D., Heinrich, R. & Baumann, K., 1998. Paleoceanography of the Last interglacial/glacial cycle in the polar North Atlantic. *Quaternary Science Reviews 17.*

Heinrich, H., 1988. Origin and Consequences of Cyclic Ice Rafting in the Northeast Atlantic Ocean during the Past 130,000 Years. *Quaternary Research,* Volum 29, pp. 142-152.

Hemming, S., 2004. Heinrich events: Massive late Pleistocene detritus layers of the North Atlantic and their global climate imprint. *Reviews of Geophysics.*

Hill, T. M., Kennett, J. P. & Valentine, D. L., 2004. Isotopic evidence for the incorporation of methane-derived carbon into foraminifera from modern methane seeps, Hydrate Ridge, Northeast Pacific. *Geochim. Cosmochim. Ac 68,* pp. 4619-4627.

Hill, T. M., Paull, C. K. & Crister, R. B., 2012. Glacial and deglacial seafloor methane emissions from pockmarks on the northern flank of the Storegga Slide complex. *Geo-Marine Letters ,* Volum 32, pp. 73-84.

Hinrichs, K.-U. & Boetius, A., 2002. The anaerobic oxidation of methane: New insights in microbial ecology and biogeochemistry. *Ocean Margin Systems,* pp. 457-477.

Hinrichs, K.-U.et al., 1999. Methane-consuming archaebacterial in marine sediments. *Nature 398,* pp. 802-805.

Hinrichs, K.-U., Hmelo, L. R. & Sylva, S. P., 2003. Molecular fossil record of elevated methane levels in Late Pleistocene coastal waters. *Science 299,* pp. 1214-1217.

Hopkins, T. S., 1991. The GIN Sea A synthesis of its physical oceanography and literature review 1972-1985. *Earth-Science Reviews 30,* pp. 175-318.

Hustoft, S., Bunz, S., Mienert, J. & Chand, S., 2009a. Gas hydrate reservoir and active methane-venting province in sediments on <20Ma young oceanic crust in the Fram Strait, offshore NW-Svalbard. *Earth and Planetary Science Letters 284,* pp. 12-24.

Hustoft, S., Dugan, B. & Mienert, J., 2009b. Effects of rapid sedimentation on developing the Nyegga pockmark field: Constraints from hydrological modeling and 3-D seismic data, offshore mid-Norway. *Geochem. Geophy. Geosy., 10.*

Husum, K. & Hald, M., 2012. Arctic planktic foraminiferal assemblages: Implications for subsurface temperature reconstructions. *Elsevier.*

Intergovernmental Panel on Climate Change, .., 2001. Climate Change 2001 - The Scientific Basis. *Cambridge University Press,* p. 881.

Intergovernmental Panel on Climate Change, .., 2007. The Physical Science Basis. Contribution of Working Group I to the Fourth Assessment Report of the Intergovernmental Panel on Climate Change. *Cambridge Univ. Press, Cambridge, U. K.*

Intergovernmental Panel on Climate Change, .., 2013. The Physical Science Basis. Contribution of Working Group I to the Fifth Assessment. Report of the Intergovernmental Panel on Climate Change. *Cambridge Univ. Press, Cambridge, U. K.*

Isaksen, I. S. A. et al., 2011. Strong atmospheric chemistry feedback to climate warming from Arctic methane emissions. *Global Biochemical Cycles,* Volum 25.

James, R. H. et al., 2016. Effects of climate change on methane emissions from seafloor sediments in the Arctic Ocean: A review. *Limnolg. Oceanogr.,* Volum 00, pp. 00-00.

Jansen, E. et al., 1983. Late Weichselian paleoceanography of the southeastern Norwegian Sea. *Norsk Geologisk Tidsskrift,* Volum 63, pp. 117-146.

Jennings, A. E., Weiner, N. J., Helgadottir, G. & Andrews, J. T., 2004. Modern foraminiferal faunas of the southwestern to northern Iceland shelf: oceanographic and environmental controls. *Journals of Foraminiferal Research,* 34(3), pp. 180-207.

Jessen, S. P., 2015. Ice rafting, Ocean circulation and Glacial activity on the western Svalbard margin 0-74000 years BP. *A dissertation for the degreee of Philosophiae Doctor.*

Jessen, S. P., Rasmussen, T. L., Nielsen, T. & Solheim, A., 2010. A new Late Weichselian and Holocene marine chronology for the western Svalbard slope 30,000-0 cal years BP. *Elsevier.*

Judd, A. G. & Hovland, M., 2007. Seabed Fluid Flow: The Impact on Geology. *Biology, and the Marine Environment,* p. 475.

Judd, A. G. et al., 2002. The geological methane budget at continental margins and. *Geofluids 2,* Volum 2, pp. 109-126.

Karcher, M. J., Gerdes, R., Kauker, F. & Koberle, C., 2003. Arctic warming: evolution and spreading of the 1990s warm event in the Nordic seas and the Arctic Ocean. *Journal of Geophysical Research ,* Volum 108.

Katz, M. E. et al., 2010. Tranditional and emerging geochemical proxies in foraminifera. *Journal of Foraminifera Research,* 40(2), pp. 165-192.

Kennett, J., Cannariato, K., Hendy, I. & Behl, R., 2000. Carbon isotopic evidence for methane hydrate instability during quaternary interstadials. *Science, volume 288.*

Kimantas, J., 2014. *www.alternativesjournal.ca.* [Online]
Available at: http://www.alternativesjournal.ca/energy-and-resources/more-methane-surprises
[Accessed 8 March 2017].

Kim, G. Y. et al., 2011. Evidence of gas hydrate from downhole logging data in the Ulleung Basin, East Sea. *Mar. Petrol. Geol. 28,* pp. 1979-1985.

King, E. L., Haflidason, H., Sejrup, H. P. & Løvlie, R., 1998. Glacigenic debris flows on the North Sea Trough Mouth Fan during ice stream maxima. *Marine Geology,* Volum 152, pp. 217-246.

Knies, J. et al., 2001. Marine ice rafted debris records constrain maximum extent of Saalian and Weichselian ice-sheets along the northern Eurasian margin. *Global and Planetary Changes,* Volum 31, pp. 45-64.

Kohfeld, K. E. & Fairbanks, R. G., 1996. Neogloquadrina pachyderma (sinistral coiling) as paleoceanographic tracers in polar oceans: Evidence from Northeast Water Polynya plankton tows, sediment traps, and surface sediment samples. *Paleoceanography ,* 11(6), pp. 679-699.

Kretschmer, K., Biastoch, A., Rüpke, L. & Burwicz, E., 2015. Modeling the fate of methane hydrates under global warming. *Global Biogeochem. Cycles,* Volum 29, pp. 610-625.

Krey, V. et al., 2009. Gas hydrates: entrance to a methane age or climate threat?. *Environmental Research Letters,* Volum 4, p. 6.

Kristensen, D. K., Rasmussen, T. L. & Koc, N., 2013. Palaeoceanographic changes in the northern Barents Sea during the last 16 000 years – new constraints on the last deglaciation of the Svalbard–Barents Sea Ice Sheet. *Boreas,* pp. 798-813.

Kucera, M. & Kennett, J. P., 2002. Causes and consequences of a middle Pleistocene origin of the modern planktonic foraminifer Neogloboquadrina pachyderma sinistral. *Geological Society of America ,* 30(6), pp. 539-542.

Kvenvolden, K. A., 1988. Methane hydrate – a major reservoir of carbon in the shallow geosphere?. *Chemical Geology 71,* pp. 41-51.

Kvenvolden, K. A., 2002. Methane hydrate in the global organic carbon. *Terra Nova ,* Volum 14, pp. 302-306.

Kvenvolden, K. A., Ginsburg, G. D. & Soloviev, V. A., 1993. World-wide distribution of subaquatic gas hydrates. *Geo-Marine Letters 13,* pp. 32-40.

Laberg, J. S. & Vorren, T. O., 1995. Late Weichselian submarine debris flow deposits on the Bear Island Trough Mouth Fan. *Marine Geology,* Volum 127, pp. 45-72.

Laskar, J. et al., 2004. A long-term numerical solution for the insolation quantities of the Earth. *Astronomy & Astrophysics,* Volum 428, pp. 261-285.

Lazar, K. B., Polyak, L. & Dipre, G. R., 2016. Re-examination of the use of Cassidulina Neoteretis as a Pleistocene biostratigraphic marker in the Arctic Ocean. *Journal of Foraminiferal Research,* 46(2), pp. 115-123.

Lekens, W. A. H. et al., 2005. Laminated sediments preceding Heinrich event 1 in the Northern North Sea and Southern Norwegian Sea: Origin, processes and regional linkage. *Marine Geology,* Volum 216, pp. 27-50.

Lelieveld, J., Crutzen, P. J. & Dentener, F. J., 1998. Changing concentration, lifetime and climate forcing of atmospheric methane. *Tellus 50B,* pp. 128-150.

Levin, L. A., 2005. Ecology of cold seeps sediments: interactions of fauna with flow, chemistry and microbes. *Oceanography and Marine Biology: An Annual Review,* Volum 43, pp. 1-46.

Linke, P. & Lutze, G. F., 1993. Microhabitat preferences of benthic foraminifera a static concept or a dynamic adaptation to optimize food acquisition?. *MMarine Micropaleontology,* Volum 20, pp. 215-234.

Liro, C. R., Adams, E. E. & Herzog, H. K., 1992. Modelling the release of carbon dioxide in the deep ocean. *Energy Conversion and Management 33,* pp. 667-674.

Lisiecki, L. E. & Raymo, M. E., 2005. A Pliocene-Pleistocene stack of 57 globally distributed benthic d18O records. *Paleoceanography,* Volum 20, p. PA1003.

Mackensen, A. & Hald, M., 1988. Cassidulina teretis Tappan and C. laevigata D'Orbigny: their modern and late quaternary distribution in Northern Seas. *Journal of Foraminiferal Research,* 18(1), pp. 16-24.

Magalhães, V. H. et al., 2012. Formation processes of methane-derived authigenic carbonates from the Gulf of Cadiz. *Sedimentary Geology,* pp. 155-168.

Mangerud, J. et al., 1998. Fluctuations of the Svalbard-Barents Sea Ice Sheet during the last 150 000 years. *Quaternary Science Reviews 17,* pp. 11-42.

Maslin, M. et al., 2010. Gas hydrates: past and future geohazard?. *Phil. Trans. R. Soc. A.,* Volum 368, pp. 2369-2393.

Mattingsdal, R. et al., 2014. A new 6 Myr stratigraphic framework for the Atlantic-Arctic Gateway. *Quaternary Sci. Rev 92,* pp. 170-178.

McGinnis, D. F. et al., 2006. Fate of rising methane bubbles in stratified waters: How much methane reaches the atmosphere?. *Journal of Geophysical Research,* Volum 111, p. C09007.

Metz, B. et al., 2007. Climate change 2007: Mitigation. *IPCC.*

Migeon, S., Weber, O., Faugeres, J. & Saint-Paul, J., 1998. SCOPIX: A new X-ray imaging system for core analysis. *Geo-Marine Letters.*

Milkov, A. V., 2004. Global estimates of hydrate-bound gas in marinesediments: how much is really out there?. *Earth-Science reviews 66,* pp. 183-197.

Möller, L. et al., 2013. Independent variations of CH4 emissions and isotopic composition over the past 160,000 years. *Nature Geoscience,* Volum 6, pp. 885-890.

Moller, T., Schulz, H. & Kucera, M., 2013. The effect of sea surface properties on shell morphology and size of the planktonic foraminifer Neogloboquadrina pachyderma in the North Atlantic. *Palaeogeography, Palaeclimatology, Palaeoecology,* Volum 391, pp. 34-48.

Müller, B. & Stein, R., 2014. High-resolution record of late glacial and deglacial sea ice changes in Fram Strait corroborates ice-ocean interactions during abrupt climate shifts. *Earth and Planetary Science Letters,* Volum 403, pp. 446-455.

Myrvang, K., 2015. *Correlation between changes in paleoceanography, pakeoclimate and methane seepage on Vestnesa Ridge, eastern Fram Strait,* Tromsø: Master's thesis in Geology.

Niemann, H. et al., 2006. Novel microbial communities of the Haakon Mosby mud volcano and their role as a methane sink. *Nature 443,* pp. 854-858.

Nørgaard-Pedersen, N. et al., 2003. Arctic Ocean during the Last Glacial Maximum: Atlantic and polar domains of surface water mass distribution and ice cover. *Paleoceanography 18.*

Orcutt, B. N. et al., 2004. Life at the edge of methane ice: microbial cycling of carbon and sulfur in Gulf of Mexico gas hydrates. *Chemical Geology 205,* pp. 239-251.

Orphan, V. J. et al., 2004. Geological, geochemical, and microbiological heterogeneity of the seafloor around methane vents in the Eel River Basin, offshore California. *Chemical Geology 205,* pp. 265-289.

Ottesen, D., Dowdeswell, J. A. & Rise, L., 2005. Submarine landforms and the reconstruction of fast-flowing ice streams within a large Quaternary ice sheet: the 2500-km-long Norwegian-Svalbard margin (57-80N). *Geol. Soc. Am. Bull. 18,* pp. 1033-1050.

Owen, M., Day, S. & Maslin, M., 2007. Late Pleistocene submarine mass movements: occurrence and causes. *Quaternary Science Reviews,* Volum 26, pp. 958-978.

Panieri, G. et al., 2009. Methane seepages recorded in benthonic foraminifera from Miocene seep carbonates, Northern Apennines (Italy). *Palaeogeogr. Palaeocl. Palaeoecol 284,* pp. 271-282.

Panieri, G., Graves, C. A. & James, R. H., 2016. Paleo-methane emissions recorded in foraminifera near the landward limit of the gas hydrate stability zone offshore western Svalbard. *Geochemistry, Geophysics, Geosystems,* Volum 17, pp. 521-537.

Patton, G. M., Martin, P. A., Voelker, A. & Salgueiro, E., 2011. Multiproxy comparison of oceanographic temperature during Heinrich Events in the eastern subtropical Atlantic. *Earth and Planetary Science Letters,* Volum 310, pp. 45-58.

Paull, C. K. et al., 2005. Geochemical constraints on the distribution of gas hydrates in the Gulf of Mexico. *Geo-Mar Lett 25,* pp. 273-280.

Paull, C. K., Ussler, W. I., Borowski, W. S. & Spiess, F. N., 1995. Methane-rich plumes on the Carolina continental rise: associations with gas hydrates. *Geology 32,* pp. 89-92.

Peltier, W. & Fairbanks, R., 2006. Global glacial ice volume and Last Glacial Maximum duration from an extended Barbados sea level record. *Quaternary Science Reviews 25,* pp. 3322-3337.

Perkin, R. G. & Lewis, E. L., 1984. Mixing in the West Spitsbergen Current. *Journal of Physical Oceanography,* Volum 14, pp. 1315-1325.

Petersen, C., Bünz, S., Hustoft, S. & and Mienert, J., 2008. 3D seismic imaging of marine gas hydrates in arctic sediments of the Vestnesa Ridge off the W-Svalbard margin: Proceedings of the 6th International Conference on Gas Hydrates, Vancouver, British Colombia, Canada.

Pflaumann, U., Duprat, J., Pujol, C. & Labeyrie, L. D., 1996. SIMMAX: A modern analog technique to deduce Atlantic sea surface temperatures from planktonic foraminifera in deep-sea sediments. *Paleoceanography,* 11(1), pp. 15-36.

Plaza-Faverola, A. et al., 2015. Role of tectonic stress in seepage evolution along the gas hydrate-charged Vestnesa Ridge, Fram Strait. *Geophysical Research Letters,* Volum 42, pp. 733-742.

Plaza-Faverola, A., Bünz, S. & Mienert, J., 2011. Repeated fluid expulsion through sub-seabed chimneys offshore Norway in response to glacial cycles. *Earth Planet. Sc. Lett. 305,* pp. 297-308.

Pohlman, J. W. et al., 2009. Methane sources in gas hydrate-bearing cold seeps: evidence from radiocarbon and stable isotopes. *Marine Chemistry 115,* pp. 102-109.

Quadfasel, D., Gascard, J. C. & Koltermann, K. P., 1987. Large-scale oceanography in Fram Strait during the 1984 Marginal Ice Zone experiment. *Journal of Geophysical Research,* Volum 92, pp. 6719-6728.

Rasmussen, T. L., Thomsen, E., van Weering, T. C. E. & Labeyrie, L., 1996. Rapid changes in surface and deep water conditions at the Faeroe Margin during the last 58,000 years. *Paleoceanography,* 11(6), pp. 757-771.

Rasmussen, T. L. & Thomson, E., 2013. Pink marine sediments reveal rapid ice melt and Arctic meltwater discharge during Dansgaard–Oeschger warmings. *Nature communications,* Volum 4.

Rasmussen, T. & Thomsen, E., 2014. Palaeoceanographic development in Storfjorden, Svalbard, during the deglaciation and Holocene: evidence from benthic foraminiferal records. *An international journey of Quaternary research.*

Rasmussen, T. et al., 2007. Paleoceanographic evolution of the SW Svalbard margin (76N) since 20,000 14C yr BP. *Quaternary Research 67.*

Rathburn, A. E. et al., 2003. Relationships between the distribution and stable isotopic composition of living benthonic foraminifera and cold methane seep biogeochemistry in Monterey Bay: California. *Geochem. Geophy. Geosy. 4,* p. 1106.

Reeburgh, W. S., 1976. Methane consumption in Cariaco Trench waters and sediments. *Earth and Planetary Science Letters 28,* pp. 337-344.

Reeburgh, W. S., 2007. Oceanic methane biogeochemistry. *Chem. Rev. 107,* pp. 486-513.

Roberts, H. H., 2001. Fluid and gas expulsion on the northern Gulf of Mexico continental slope: mud-prone to mineral -prone responses. *Natural Gas Hydrates: Occurrence, Distribution, and Detection,* pp. 145-161.

Rowan, C. J., Roberts, A. P. & Broadbent, T., 2009. Reductive diagenesis, magnetite dissolution, greigite growth and paleomagnetic smoothing in marine sediments: A new view. *Earth and Planetary Science Letters,* Volum 277, pp. 223-235.

Rudels, B. et al., 2000. Water mass distribution in Fram Strait and over the Yermak Plateau in summer 1997. *Ann. Geophysicae 18,* pp. 687-705.

Ruppel, C. D., 2011. Methane Hydrates and Contemporary Climate Change. *Nature Education Knowledge.*

Schaefer, K., Lantuit, H., Romanovsky, V. & Schuur, E., 2012. Policy Implications of Warming Permafrost. *United Nations Environment Programme.*

Schiebel, R. & Hemleben, C., 2005. Modern planktic foraminifera. *Paläontologische Zeitschrift.*

Screen, J. A. & Simmonds, I., 2010. The central role of diminishing sea ice in recent Arctic temperature amplification. *Nature 464,* pp. 1334-1337.

Seidenkrantz, M. S., 1995. Cassidulina teretis Tappan and Cassidulina neoteretis new species (Foraminifera): stratigraphic markers for deep sea and outer shelf areas. *Journal of Micropalaeontology,* 14(2), pp. 145-157.

Shackleton, N. J., 1987. The carbon isotope record of the Cenozoic: history of organic carbon burial and of oxygen in the ocean and atmosphere. *Marine Petroleum Source Rocks,* Volum 26, pp. 423-434.

Shakhova, N. et al., 2013. Ebullition and storm-induced methane release from the East Siberian Arctic Shelf. *Nature Geoscience.*

Shakhova, N. et al., 2010. Extensive Methane Venting to the Atmosphere from Sediments of the East Siberian Arctic Shelf. *Sciencemag.*

Shakhova, N. et al., 2015. The East Siberian Arctic Shelf: towards further assessment of permafrost-related methane fluxes and role of sea ice. *Philosophical Transactions A.*

Shipley, T. H. et al., 1979. Seismic reflection evidence for the widespread occurrence of possible gas hydrate horizons on continental slopes and rises. *Am. Ass. Petrol. Geol. Bull 63,* pp. 2201-2213.

Sibuet, M. & Olu, K., 1998. Biogeography, biodiversity and fluid dependence of deep-sea cold-seep communities at active and passive margins. *Deep-Sea Research II,* Volum 45, pp. 517-567.

Siegert, M. & Dowdeswell, J., 1995. Numerical modeling of the Late Weichselian Svalbard-Barents Sea Ice Sheet. *Quaternary Research 43,* pp. 1-13.

Sloan, E. D., 1998. Gas hydrates: Review of physical/chemical properties. *Energy Fuels 12,* pp. 191-196.

Slubowska, M. A., Kocß, N., Rasmussen, T. L. & Klitgaard-Kristensen, D., 2005. Changes in the flow of Atlantic water into the Arctic Ocean since the last deglaciation: evidence from the northern Svalbard continental margin, 80N. *Paleoceanography 20,* p. 4014.

Slubowska-Woldengen, M. et al., 2007. Advection of Atlantic Water to the western and northern Svalbard shelf. *Quaternary Science Reviews,* Volum 26, pp. 463-478.

Smith, A. J., Mienert, J., Bünz, S. & Greinert, J., 2014. Thermogenic methane injection via bubble transport into the upper Arctic Ocean from the hydrate-charged Vestnesa Ridge, Svalbard. *Geochem. Geophy. Geosy 15,* pp. 1945-1959.

Smith, L. M. et al., 2001. Light d13C events during deglaciation of the East Greenland continental shelf attributed to methane release from gas hydrates. *Geophysical Research Letters,* 28(11), pp. 2217-2220.

Smith, V. O., 1995. Primary productivity and new production in the Northeast Water (Greenland) Polynya during summer 1992. *Journal of Geophysical Research,* Volum 100, pp. 4341-4356.

Snyder, G. T. et al., 2007. Pore water profiles and authigenic mineralization in shallow marine sediments above the methane-charged system on Umitaka Spur, Japan Se. *Deep-Sea Res. PartII 54,* pp. 1216-1239.

Solheim, A. et al., 1998. Late Cenozoic seismic stratigraphy and glacial geological development of the East Greenland and Svalbard-Barents Sea continental margins. *Quaternary Science Reviews, Vol 17,* pp. 155-184.

Spielhagen, R. & Erlenkeuser, H., 1994. Stable oxygen and carbon isotopes in planktic foraminifers from Arctic Ocean surface sediments: Reflection of the low salinity surface water layer. *Marine geology volume 119.*

Spielhagen, R. F. et al., 2011. Enhanced modern heat transfer to the Arctic by warm Atlantic water. *Science 331,* pp. 450-453.

Stabell, B., 1986. A diatom maximum horizon in upper quaternary deposits. *Geologische Rundschau,* Volum 75/1, pp. 175-184.

Stanford, J. D. et al., 2011. A new concept for the paleoceanographic evolution of Heinrich event 1 in the North Atlantic. *Quaternary Science Reviews,* Volum 30, pp. 1047-1066.

Stuiver, M., Reimer, P. J. & Reimer, R. W., 2016. *CALIB Radiocarbon Calibration.* [Online]
Available at: http://calib.org/calib
[Accessed 6 March 2017].

Suess, E. et al., 1999. Gas hydrate destabilization: enhanced dewatering, benthic material turnover and large methane plumes at the Cascadia convergent margin. *Earth and Planetary Science Letters 170,* pp. 1-15.

Svendsen, J. I. et al., 2004. Late Quaternary ice sheet history of northern Eurasia. *Quaternary Science Reviews,* Volum 23, pp. 1229-1271.

Svendsen, J. I. & Mangerud, J., 1992. Paleoclimatic inferences from glacial fluctuations on Svalbard during the last 20 000 years. *Climate Dynamics,* Volum 6, pp. 213-220.

Svendsen, J. I. & Mangerud, J., 1997. Holocene glacial and climatic variations on Spitsbergen, Svalbard. *The Holocene,* 7(1), pp. 45-47.

Sztybor, K. A., 2017. Late glacial and deglaicial paleoceanographic and environmental changes at Vestnesa Ridge, Fram Strait. *A dissertation for the degree of Philosophiae Doctor.*

Sztybor, K. & Rasmussen, T. L., 2016. Diagenetic disturbances of marine sedimentary records from methane-influenced environments in the Fram Strait as indications of variation in seep intensity during the last 35.000 years.

Sztybor, K. & Rasmussen, T. L., 2017. Late glacial and deglacial palaeoceanographic changes at Vestnesa Ridge, Fram Strait: Methane seep versus non-seep environments. *Palaeogeography, Palaeoclimatology, Palaeoecology,* Volum 476, pp. 77-89.

Treude, T. et al., 2003. Anaerobic oxidation of methane above gas hydrates at Hydrate Ridge. *NE Pacific Ocean, Mar. Ecol.-Prog. Ser., 264,* pp. 1-14.

Treude, T. et al., 2005. Anaerobic oxidation of methane and sulfate reduction along the Chilean continental margin. *Geochimica et Cosmochimica Acta 69,* pp. 2767-2779.

Ussler III, W. & Paull, C. K., 2008. Rates of anaerobic oxidation of methane and authigenic carbonate mineralization in methane-rich deep-sea sediments inferred from models and geochemical profiles. *Earth and Planetary Science Letters,* Volum 266, pp. 271-287.

Vogt, C., Knies, J., Spielhagen, R. & Stein, R., 2001. Detailed mineralogical evidence for two nearly identical glacial/deglacial cycles and Atlantic water advection to the Arctic Ocean during the last 90,000 years. *Global and Planetary Change 31,* pp. 23-44.

Vorren, T. O. & Laberg, J. S., 1997. Through mouth fans - paleoclimate and ice-sheet monitors. *Quaternary Science Reviews,* Volum 16, pp. 865-881.

Walczowski, W., Piechura, J., Osinski, R. & Wieczorek, P., 2005. The West Spitsbergen Current volume and heat transport from synoptic observations in summer. *Deep Sea Research Part I Oceanographic Research Papers,* Volum 52, pp. 1371-1391.

Wefer, G., Heinze, P.-M. & Berger, W. H., 1994. Clues to ancient methane release. *Nature 369,* p. 282.

Westbrook, G. K. et al., 2009. Escape of methane gas from the seabed along the West Spitsbergen continental margin. *Geophysical Research Letters,* Volum 36, p. L15608.

Whiticar, M. J., 1999. Carbon and hydrogen isotope systematics of bacterial formation and oxidation of methane. *Chemical Geology 161,* pp. 291-314.

Zamelczyk, K. et al., 2014. Surface water conditions and calcium carbonate preservation in the Fram Strait during marine isotope stage 2, 28.8–15.4 kyr. *Paleoceanography,* Volum 29, pp. 1-12.

Zhang, J., Rothrock, D. A. & Steele, M., 1998. Warming of the ARctic Ocean by a strengthened Atlantic inflow: model results. *Geophysical Research Letters 25,* pp. 1745-1748.